ELECTRON WORK FUNCTIONS

by

THOMAS A. JENNINGS

Thesis
543.272
JEN

11 OCT 71 142934

A thesis submitted for the
Degree of Doctor of Philosophy
in the
Department of Chemistry
of the
University of Aston
in Birmingham

September, 1971.

ACKNOWLEDGEMENTS

It is a joy to acknowledge the following debts of gratitude:

The first is to Professor F. M. Page for the many long hours of consultation and the sincere interest he has shown in this study.

I am especially indebted to the Hull Corporation for their most generous financial support.

The third is to my wife, Marianne, for her endless encouragement and patience during these last few years.

I am grateful for the assistance and co-operation of Mr. W. E. Sabin and Mr. L. Parker during the construction of the ultra high vacuum system.

Last I am indebted to Miss S. E. Grice for her excellent typing skill and the suffering she experienced because of my American longhand writing.

CONTENTS

		Page
1.	INTRODUCTION	1
1.1.	Introduction	1
1.2.	General Considerations for the Adsorption of Gases on a Metal Surface	1
1.3.	General Considerations of the Desorption Reaction	2
1.4.	Surface Ionisation	3
2.	THE THERMAL DESORPTION OF GASES FROM A METAL SURFACE	6
2.1.	Introduction	6
2.2.	The Theory of the Absolute Reaction Rate	7
2.3.	Application of the Theory of Absolute Reaction Rates to Thermal Desorption Reactions	14
2.4.	Interpretation of the Thermal Desorption Data	16
2.5.	The Experimental Techniques and Apparatus used in Thermal Desorption Studies	19
2.5.1.	Required information	19
2.5.2.	Detection of the desorbed gases	23
2.5.3.	Vacuum pumps	26
2.5.3.1.	Diffusion pumps	26
2.5.3.2.	Turbo-molecular pump	27
2.5.3.3.	Sorption pumps	27
2.5.3.4.	Sublimation pumps	28
2.5.3.5.	Getter ion pump	28
2.5.4.	Construction of the vacuum system	29

Page

3. THE ELECTRON WORK FUNCTION 31

3.1. Introduction 31

3.2. The Electron Work Function 31

3.3. Basic Techniques for the Determination of the Electron Work Function of a Surface 34

3.3.1. Thermionic emission 34

3.3.2. Photoelectric emission 36

3.3.3. Field emission 38

3.3.4. Contact potential difference 40

3.3.4.1. Capacitor method 40

3.3.4.2. Electron beam method 41

3.3.4.3. Use of the contact potential difference method in the study of gas-metal surface interactions 46

3.4. Work Function Measurements on Patchy Surface 47

4. EXPERIMENTAL APPARATUS 50

4.1. Introduction 50

4.2. Vacuum System 50

4.2.1. General description 50

4.2.2. Sorption pumps 51

4.2.3. Sublimation pump 54

4.2.4. Trigger discharge gauge 55

4.2.5. Vacuum pump-down procedure 56

4.3. The Reaction Cell 57

4.4. Gas Supply System 59

Page

5. RESULTS AND DISCUSSION OF THE THERMAL DESORPTION REACTIONS 61

5.1. Introduction 61

5.2. The Oscilloscope Display of a Thermal Desorption Reaction 61

5.2.1. Determination of the total pumping speed 63

5.2.2. Collector temperatures as a function of time 66

5.3 Experimental Procedure 70

5.4. The Analysis of a β_1 Desorption Peak 70

5.4.1. Determination of the rate of desorption as a function of time 71

5.4.2. Calculation of the coverage of the surface 74

5.4.3. Determination of the order of the reaction 77

5.4.4. Determination of the heat of activation energies, the change in entropy and the standard free energy for the reaction 77

5.5. The Analysis of a β_2 Desorption Peak 80

5.5.1. Determination of the rate of desorption as a function of time 80

5.5.2. Calculation of the coverage of the surface 80

5.5.3. Determination of the order of the reaction 83

5.5.4. Determination of the heat of activation energies, the change in entropy and the standard free energy for the desorption reaction 83

Page

5.6. The Effect of the Residual Gases on the Thermal Desorption Spectrum 84

5.6.1. The effects of the residual gases on the thermal desorption spectrum 84

5.6.2. The effects of the desorption of gases from the sublimation pump on the thermal desorption spectrum 86

5.6.3. The effects of the thermal desorption of gases from the walls of the experimental cell on the thermal desorption spectrum 87

5.6.4. Summary 89

5.7. The Thermal Desorption of Oxygen from a Tantalum Surface 89

6. RESULTS AND DISCUSSION OF THE EFFECTS OF ADSORBED GASES ON THE WORK FUNCTION OF A TANTALUM SURFACE 93

6.1. Introduction 93

6.2. Collector Current-Voltage Characteristic Plot 93

6.3. Emitter Temperature 94

6.3.1. Energy distribution method 95

6.3.2. Optical method 96

6.4. The Effect of the Grid Voltage on the Current-Voltage Characteristic Plot 98

6.4.1. The effect of the grid voltage on the saturated collector current 98

6.4.2. The effect of the grid voltage on the collector current in the retarding portion of the characteristic plot 99

Page

6.4.3. The effect of the grid voltage on the calculated emitter temperature 99

6.5. Determination of the Electron Work Function of the Emitter and Collector Surfaces from the Current-Voltage Characteristic Plot 104

6.5.1. Emitter "effective" work function 104

6.5.2. The collector "effective" work function 105

6.5.3. The "apparent" work function of the emitter 107

6.5.4. The "apparent" work function of the collector 107

6.5.5. The "effective" and "apparent" work function for a thermally cleaned collector surface 108

6.5.6. The interaction of oxygen with a tantalum surface 110

7. SUMMARY AND CONCLUSION 113

7.1. Experimental Apparatus 113

7.2. Thermal Desorption of Oxygen from a Polycrystalline Tantalum Surface 114

7.3. The Effect of Adsorbed Gases on the Electron Work Function of a Polycrystalline Tantalum Surface 116

7.4. Use of the Planar Triode by Other Investigators 118

FIGURES

		Between Pages
Fig. 1.	Desorption of gases from a metal surface.	17-18
Fig. 2.	A typical plot of the desorption rate as a function of time.	18-19
Fig. 3.	Thermal desorption spectrum for a closed system.	20-21
Fig. 4.	Thermal desorption spectrum for an open system.	21-22
Fig. 5.	Contact potential difference between two metal surfaces[2].	40-41
Fig. 6.	Current J_2 as a function of applied voltage V_1.	42-43
Fig. 7.	Potential difference in saturated region of the characteristic plot.	44-45
Fig. 8.	Potential difference in the retarding region of the characteristic plot.	45-46
Fig. 9.	Family of current-voltage characteristic plots.	46-47
Fig. 10.	Experimental equipment.	50-51
Fig. 11.	Sorption pump pressure as a function of time.	53-54
Fig. 12.	Cutaway of sublimation pump.	54-55
Fig. 13.	Planar triode[45].	58-59
Fig. 14.	Cutaway of experimental cell.	58-59
Fig. 15.	Electrical circuit for work function determination	58-59
Fig. 16.	Electrical circuit for thermal desorption studies.	58-59
Fig. 17.	Apparatus used to prepare oxygen gas sample.	60-61

Between Pages

Fig. 18. An oscilloscope display of a thermal desorption reaction. 61-62

Fig. 19. Resistance R_T as a function of time. 66-67

Fig. 20. Collector temperature as a function of time. 69-70

Fig. 21. Thermal desorption spectrum of experiment No. 224-3. 70-71

Fig. 22. Pressure P^* as a function of time. 71-72

Fig. 23. The rate of desorption as a function of time. 74-75

Fig. 24. $\ln \dfrac{(dn/dt)_t}{(\sigma_o - \sigma_t)^{n'} T}$ as a function of (1/T); ($n'=1$) × , ($n'=2$) ● . 77-78

Fig. 25. Pressure P^* as a function of time. 80-81

Fig. 26. The rate of desorption as a function of time. 80-81

Fig. 27. $\ln \dfrac{(dn/dt)_t}{(\sigma_o - \sigma_t)^{n'} T}$ as a function of (1/T); ($n'=1$) × , ($n'=2$) ● . 83-84

Fig. 28. Thermal desorption spectrum of residual gases after an adsorption time of three minutes. 84-85

Fig. 29. Thermal desorption spectrum of residual gases after an adsorption time of three hours. 86-87

Fig. 30. Thermal desorption spectrum of oxygen after two hours at a pressure of 5×10^{-8} torr. 89-90

Fig. 31. The rate of desorption as a function of time; calculated × , experimental ● . 91-92

Fig. 32. The rate of desorption as a function of time; calculated × , experimental ● . 92-93

Between Pages

Fig. 33. A typical collector current-voltage characteristic plot. 93-94

Fig. 34. Filament current as a function of T^2. 97-98

Fig. 35. Collector current as a function of the grid voltage; plot I $\circ$; plot II $\times$. 98-99

Fig. 36. The effect of an applied grid voltage of 100 volts on the current-voltage characteristic plot. 101-102

Fig. 37. Family of current-voltage characteristic plots. 104-105

Fig. 38. The $\ln(J_2/T_1^2)$ as a function of $(1/T)$. 107-108

Fig. 39. $(\ln(J_2/T_1^2) - \bar{V}_{12}(T))$ as a function of $(1/T_1)$. 107-108

Fig. 40. Thermal desorption spectrum showing the contamination of the collector surface due to desorption from the walls of the experimental cell. 111-112

Fig. 41. Thermal desorption of oxygen after one hour at a pressure of 6×10^{-8} torr. 111-112

TABLES

Table		Page
I	Observed experimental values of the pressure, collector current, and collector voltage and the calculated values of the total collector resistance and temperature at various times during the thermal desorption reaction	64
II	Observed experimental values of the pressure and calculated values of the collector temperature at various times during the thermal desorption reaction	72
III	Calculated values of P_t^*, $\left(\frac{dP^*}{dt}\right)_t$, $\frac{P_t^*}{P_{t_m}^*}$, and $\frac{dn}{dt}$ at various times during the β_1 thermal desorption reaction	73
IV	A list of experimentally determined values used to examine the kinetics of β_1 reaction	75
V	The results of the analysis of a β_1 desorption reaction	79
VI	Calculated values of P_t^*, $(dP^*/dt)_t$, (P_t^*/P_{t_m}), and $(dn/dt)_t$ at various times during the thermal desorption	81
VII	A list of experimentally determined values used to examine the kinetics of the β_2 reaction	82
VIII	The results of the analysis of the β_2 thermal desorption reaction	85

Table		Page
IX	Results of the analysis of the β_1 peak of experiment No. 231-1	88
X	Results of the analysis of the thermal desorption spectrum of oxygen from a tantalum surface	90
XI	The observed brightness temperature S and the calculated "true" temperature T_1 for a given filament current I_F	97
XII	Calculated emitter temperatures, measured collector current and optically measured emitter temperatures at various applied grid voltages	100
XIII	The effective emitter work function for various emitter temperatures obtained from the characteristic plots of experiment No. 207	105
XIV	The "effective" collector work function and contact potentials obtained from the characteristic plots of experiment No. 207	106
XV	Results of the "effective" work function determined with a thermally cleaned collector surface	109

This work was carried out between January, 1969 and July, 1971 at the University of Aston in Birmingham. The work was done independently, and has not been submitted for any other degree.

T. A. Jennings

SUMMARY

The interaction of oxygen with a tantalum surface has been studied in an ultra high vacuum system. This study consisted of observing the thermal desorption of neutral species from the surface and the effects of gas adsorption on the electron work function.

The study of the thermal desorption spectrum revealed the presence of two adsorbed gas species. From this study, the initial coverage of each adsorbed species and the order, heat of activation, change in entropy and free energy change for each of the desorption reactions were ascertained.

The effect of the adsorption of oxygen on the tantalum surface was observed from the change in the electron work function. The electron work function in these studies was determined by a contact potential difference method.

CHAPTER 1

INTRODUCTION

1.1. Introduction

The interaction of gases with a metal surface represents one of the earliest studied chemical reactions. For example, in 1796 van Marum studied the dehydrogenation of alcohols by metal surfaces[1]. Since that time, a vast number of studies of gas-metal surface reactions have been undertaken. As a result of these studies, the gas-metal surface reaction can be broken down into two main categories:

1. The adsorption of gases on the metal surface.
2. The desorption of products from the surface.

1.2. General Considerations for the Adsorption of Gases on a Metal Surface

When atoms or molecules of a gas collide with a metal surface there exist a finite probability that they will be adsorbed on the surface. If the adsorption is an activated reaction then the rate of adsorption has been defined as[2]

$$r_a = \frac{\sigma P\, f(\theta)}{(2\pi mkT)^{\frac{1}{2}}} \exp(-E/RT) \qquad 1.1$$

where σ is the condensation coefficient, P is the gas pressure above the metal surface, $f(\theta)$ represents the probability that the gas will make a collision with an active site, and E is the activated energy of adsorption reaction. For atoms or molecules that are physically adsorbed on the surface, i.e., the forces between the molecule and the metal surface are weak Van der Waals forces, the molecule must

surmount an energy barrier of a magnitude E in order to become chemisorbed. If the energy barrier is greater than the physical desorption energy, then when the molecule acquires sufficient energy to pass over the barrier, it will be preferentially desorbed rather than chemisorbed. Chemisorption for the activation adsorption reaction can only occur directly from the gas phase.

In the non-activated adsorption reaction, the activation energy E_a will approach zero. In this reaction the desorption energy of the physically adsorbed precursor will be greater than that of the activation energy E_a and hence a physically adsorbed molecule can become chemisorbed. The chance that a physically adsorbed molecule will become chemisorbed will depend on the availability of active sites on the surface and thus the surface coverage will be an important factor for the chemisorption of molecules when a precursor is involved.

1.3. General Considerations of the Desorption Reaction

The rate of desorption of gases from a metal surface can be expressed as

$$n = k_{n'} \sigma^{n'} \exp(-Q_j/RT) \qquad 1.2$$

where σ is the surface coverage, n' is the order of the reaction, $k_{n'}$ is a constant, and Q_j is the desorption activation energy for a molecule adsorbed in the jth state.

While an adsorbed gas molecule usually exists in a single physically adsorbed state, the molecules in the chemisorbed state have been known to exist in a number of adsorbed states[3, 4]. Each

of these adsorbed states can be characterized by its own individual desorption rate equation.

1.4. Surface Ionisation

Surface ionisation is a process by which atom or molecules are desorbed from a surface in a charged state. These charged species may be positive or negative ions. The formation of negative ions is of considerable academic and commercial interest. Its commercial interest stems from the use of negative ions in the formation of dielectric material by means of a gas phase anodisation reaction[5, 6].

The degree of surface ionisation for the ith species desorbing from a surface can be defined as

$$\alpha = \frac{N_{I,i}}{N_i} \qquad 1.3$$

Where $N_{I,i}$ represents the number of positive or negative ions of the ith species that are desorbed from the surface per unit time per unit area, and N_i is the number of neutral species that are desorbed from the surface per unit time per unit area. α has been shown to be a function of the temperature of the surface T, the electron work function $e\chi$, the ionisation potential I or the electron affinity A, and the electric field that accelerates the ions from the surface F.

From the Saha equation, α_+ can be expressed as[8]

$$\alpha_+ = \left(\frac{g_+}{g_o}\right)\left(\frac{A}{A^*}\right)\left[\frac{(1-\bar{r}_+)(1-\bar{r}_e)}{(1-\bar{r}_o)}\right]\exp((e\chi - eI_i)/kT) \qquad 1.4$$

where $\frac{g_+}{g_o}$ is the ratio of the statistical weights of the positive ions and atomic states of the adsorbed atom, $\bar{r}_+$, $\bar{r}_e$ and $\bar{r}_o$ are the average reflection coefficients of the positive ions, the electrons and the neutral atoms, respectively, and A/A^* is the ratio of the thermionic emission constant (120.4 amperes cm^{-2} deg^{-2}) and the "apparent" emission constant. Equation 1.4 is generally referred to as the Saha-Langmuir equation.

An analogous expression for α_- is given as[8]

$$\alpha_- = \left(\frac{Q_-}{Q_o}\right)\left(\frac{A}{A^*}\right)\left[\frac{(1-\bar{r}_-)(1-\bar{r}_e)}{(1-\bar{r}_o)}\right] \exp\left((A' - e\chi)/kT\right) \qquad 1.5$$

where Q_-/Q_o is the statistical sum ratio of the adsorbed negative ion and that of the neutral atom, respectively. The electron affinity A', for a given surface temperature T, cannot be obtained by directly solving equation 1.5 for a given value of α_-. This results from the fact that σ_-, σ_o, $\bar{r}_-$, $\bar{r}_e$ and $\bar{r}_o$ cannot be experimentally ascertained and a value of A^* could be in serious error.

An approximate value of A can be obtained by solving

$$A' = -k\frac{d(\ln\alpha_-)}{d(1/T)} + e\chi \qquad 1.6$$

provided $e\chi$ and the pre-exponential terms in equation 1.5 are not significantly temperature dependent.

Consider the following alternate method for the determination of the electron affinity. F. M. Page[9] has shown by a thermodynamic calculation that the rate of desorption of negative ions per unit

area can be expressed as

$$n_- = \frac{\sigma c}{\sigma_s} \exp(A' - Q_j - e\chi)/RT) \qquad 1.7$$

where c is a function of the electronic charge, σ/σ_s represents the fraction of the surface covered by the adsorbed gas species and Q_j is the heat of desorption of the electron acceptor. By dividing equation 1.2 into equation 1.7 one obtains

$$\frac{n_-}{n} = \alpha_- = \frac{c\,\sigma}{\sigma_s\, k_{n'}\, \sigma^{n'}} \exp((A' - e\chi)/RT). \qquad 1.8$$

In equation 1.8, all the quantities in the pre-exponential term are known or can be experimentally ascertained. Hence, the electron affinity can be ascertained by directly solving equation 1.8. In order to solve equation 1.8 one must know the following:

1. The rate equation for the desorption of neutral gas species from the metal surface.
2. The electron work function of the surface as a function of coverage.
3. The temperature of the surface.
4. The rate equation for the desorption of a given ion species from a metal surface.

This thesis represents a study of the thermal desorption reaction of neutral gas species from a metal surface and the determination of the electron work function in the presence of adsorbed gas species.

CHAPTER 2

THE THERMAL DESORPTION OF GASES FROM A METAL SURFACE

2.1. Introduction

A great number of studies concerning the interaction of various gas species with metal surfaces have been reported in the literature[10, 11]. Most of these studies have been concerned with the adsorption reaction. The adsorption reaction has increased our knowledge concerning the gas-metal surface interaction by providing the following information:

1. The adsorption isotherm for various gas-metal surface systems.
2. The heat of adsorption as a function of surface coverage.
3. A rate equation for adsorption under certain well defined conditions.
4. The determination of the adsorption activation energy for systems such as hydrogen and nickel.

While the above information certainly adds to our understanding of the gas-metal surface reaction, the study of the adsorption reaction has not provided information regarding the following:

1. The existence of a number of adsorbed gas phases for a given gas-metal system.
2. The binding energy for each of the individual adsorbed gas phases.

From thermal desorption studies it is not only possible to ascertain the individual adsorption phases and their associated binding

energies, but also to provide the following additional information concerning the desorption reaction:

1. The rate equation for the desorption reaction.
2. The order of the desorption reaction for each of the individual adsorbed phases.
3. The number of adsorbed gas species per unit area for each of the phases.

In view of the importance of a thermal desorption study, the remaining portions of this section will be concerned with (a) the theory of the absolute rate reaction, (b) the application of the latter theory to the desorption reaction, (c) the interpretation of the thermal desorption data, and (d) the experimented apparatus and techniques used in thermal desorption studies.

2.2. The Theory of the Absolute Reaction Rate

The quantitative formulation of reaction rates in terms of activated complexes was first used by H. Eyring in 1935[12]. Since that time the theory has been applied to a wide range of rate processes, such as diffusion, dielectric loss, and internal friction in high polymers[1].

This theory is based substantially on two main postulates[13]. The first postulate states that for any atomic or molecular process that requires an activation energy, the atoms or molecules involved must first form an activated complex. The rate of the reaction will be dependent on a factor of the form exp $(-\alpha/T)$. The activated complex will form at the top of an energy barrier which separates the initial and final states. The rate of the reaction is then the velocity at which the activated complex passes over the barrier.

The second postulate states that the initial reactants are always in equilibrium with the activated complex, and that the latter decomposes to the final state at a definite rate.

Consider an activated atom or molecule having a velocity between $\dot{x}$ and $\dot{x} + d\dot{x}$ in one degree of freedom. The probability of such an event occurring is given as

$$P(\dot{x}) = \text{constant} \cdot \exp\left(m^*(\dot{x})^2/(2kT)\right) d\dot{x} \qquad 2.1$$

where m^* is the mass of the activated complex and k is the Boltzmann constant.

The average velocity of the complex with a motion in one direction can be expressed by

$$\bar{\dot{x}} = \frac{\int_0^\infty \exp\left(-(m^*(\dot{x})^2)/(2kT)\right) \dot{x}\, d\dot{x}}{\int_{-\infty}^\infty \exp\left(-(m^*(\dot{x})^2)/(2kT)\right) \dot{x}\, d\dot{x}} \qquad 2.2$$

or

$$\bar{\dot{x}} = \left(\frac{kT}{2\pi m^*}\right)^{\frac{1}{2}} . \qquad 2.3$$

If d is considered as the width of the top of the barrier, then the average time required for an activated complex to cross this distance has the form

$$\tau = \frac{d}{\bar{\dot{x}}} = \left(\frac{2\pi m^*}{kT}\right)^{\frac{1}{2}} \times d . \qquad 2.4$$

The fraction of the activated complexes that will cross the barrier per unit time will be $1/\tau$. The concentration of the activated complexes is given as $C^{\ddagger}$ and the rate at which they cross the barrier is

$$r = k^* C_A C_B \cdots C_N = C^{\ddagger} \left(\frac{kT}{2\pi m^*} \right)^{\frac{1}{2}} \times \frac{1}{d} \qquad 2.5$$

where the term $C_A C_B \cdots C_N$ represents the product of the concentrations of the reactants and the k^* is known generally as the rate constant for the reaction. The rate constant k^* can be expressed as

$$k^* = \frac{C^{\ddagger}}{C_A C_B \cdots C_N} \left(\frac{kT}{2\pi m^*} \right)^{\frac{1}{2}} \times \frac{1}{d} \cdot \qquad 2.6$$

Since it was postulated earlier that the reactants will always be in equilibrium with the activated complex, it then becomes possible to express the equilibrium constant for the system of ideal substances as

$$K = \frac{C^{\ddagger}}{C_A C_B \cdots C_N} \cdot \qquad 2.7$$

If statistical mechanics are used then the equilibrium constant is expressed by

$$K = \frac{F_{\ddagger}'}{F_A F_B \cdots F_N} \exp(-E_o/(RT)) \qquad 2.8$$

where E_o represents the difference in the zero level energy per mole of the activated complex and that of the reactants. In other words E_o in equation 2.8 represents the amount of energy that the reactants must

acquire before they can form the activated complex. $F_{\ddagger}^{'}$ represents the complete partition function for the activated complex, while the product of the total partition functions of the reactants is given as $F_A F_B \cdots F_N$.

By assuming that equilibrium constants defined by equations 2.7 and 2.8 are equivalent, equation 2.6 becomes

$$k^* = \frac{1}{d} \left(\frac{kT}{2\pi m^*} \right)^{\frac{1}{2}} \frac{F_{\ddagger}^{'}}{F_A F_B \cdots F_N} \exp(-E_o/(RT)) \quad . \qquad 2.9$$

$F_{\ddagger}^{'}$ is the complete partition function for the activated complex. The complex will, because of translational motion along the reaction co-ordinate, decompose to either products or to the initial reactants. The complete partition function for the activated complex can be expressed as

$$F_{\ddagger}^{'} = F_{\ddagger} f(tr) \qquad 2.10$$

where f (tr) is the translational partition function and is given by

$$f(tr) = \left(\frac{2\pi m^* kT}{h} \right)^{\frac{1}{2}} \times d \qquad 2.11$$

and h is Plank's constant.

By substitution of equations 2.10 and 2.11 into equation 2.9, the expression for the rate constant becomes

$$k^* = \frac{F_{\ddagger}}{F_A F_B \cdots F_N} \left(\frac{kT}{h^{\frac{1}{2}}} \right) \exp(-E_o/(RT)) \quad . \qquad 2.12$$

In order to allow for the possibility that not every activated complex that reaches the top of the barrier will decompose into products, a transmission coefficient $\bar{K}$ is introduced and equation 2.12 can now take the form of

$$k^* = \frac{\bar{K}\ F_{\ddagger}}{F_A\ F_B \cdots F_N} \left(\frac{kT}{h^{\frac{1}{2}}} \right) \exp\left(-E_o/(RT)\right) . \qquad 2.13$$

The rate of the reaction is now expressed as

$$r = k^*\ C_A\ C_B \cdots C_N = \bar{K}\ C_A\ C_B \cdots C_N \frac{F_{\ddagger}}{F_A\ F_B \cdots F_N} \left(\frac{kT}{h^{\frac{1}{2}}} \right) \exp\left(-E_o/(RT)\right) . \qquad 2.14$$

If it is assumed that the experimental energy difference between the activated complex and the reactants ΔE_p approximates the value of E_o, then equation 2.14 in a logarithmic form becomes

$$\ln(r) = \ln \frac{K\ (C_A\ C_B \cdots C_N)\ k\ F_{\ddagger}}{F_A\ F_B \cdots F_N\ h^{\frac{1}{2}}} + \ln T - \frac{\Delta E_p}{RT} . \qquad 2.15$$

An expression for the experimental activation energy ΔE_p can be obtained by the differentiation of equation 2.15 with respect to temperature and is given as

$$\frac{d \ln(r)}{dT} = -\frac{\Delta E_p}{RT^2} + \frac{1}{T} . \qquad 2.16$$

The equilibrium constant can also be expressed in terms of the standard free energy of the reaction, i.e.,

$$K = \exp\left(\frac{-\Delta G^{o}}{RT}\right) \qquad 2.17$$

where

$$\Delta G^{o} = \Delta G_1^{\ddagger} - \Delta G_2^{\ddagger} \qquad 2.18$$

and $\Delta G_1^{\ddagger}$ and $\Delta G_2^{\ddagger}$ represent the free energies for the reaction in the forward and reverse direction[10]. The standard free energy can also be expressed in the form

$$\Delta G^{o} = \Delta H^{o} - T\Delta S^{o} \qquad 2.19$$

and ΔH^{o} and ΔS^{o} represent the standard heat of the reaction and the change on entropy, respectively.

From equation 2.17 and 2.18 the equilibrium constant can now be expressed by

$$K = \frac{k_1}{k_2} = \frac{\exp\left(-\Delta G_1^{\ddagger}/(RT)\right)}{\exp\left(-\Delta G_2^{\ddagger}/(RT)\right)} \qquad 2.20$$

where k_1 and k_2 represent the rate constants for the forward and reverse reaction respectively. Hence, the rate for the forward reaction can be expressed as

$$\ln(r_1) = \ln\left(k_1 C_A C_B \cdots C_N\right) = \ln\left(C_A C_B \cdots C_N\right) + \frac{\Delta S_1^{\ddagger}}{R} - \frac{\Delta H_1^{\ddagger}}{RT} . \qquad 2.21$$

$\Delta S_1^{\ddagger}$ and $\Delta H_1^{\ddagger}$ in equation 2.21 represent the change in entropy and the heat of activation for the formation of the activated complex.

Upon differentiation of equation 2.21 with respect to temperature, one obtains the following expression for the heat of activation, namely

$$\frac{d \ln(r_1)}{dT} = \frac{-\Delta H^{\ddagger}}{RT^2} \quad . \qquad 2.22$$

If the reaction rate (r), expressed by equation 2.15, can be represented by the forward reaction rate (r_1), then by combining equations 2.16 and 2.22, the heat of activation for the formation of the complex can be expressed by

$$\Delta H_1^{\ddagger} = \Delta E_p - RT \quad . \qquad 2.23$$

By assuming also that a constant k_{1n}^{1}, can now be introduced into equation 2.21, the expression for the change in entropy of the activation reaction can now be expressed as

$$\Delta S_1^{\ddagger} = \left[R \ln(r_1) - \ln(k_{1n}^{1} C_A C_B \cdots C_N) - 1 \right] + \frac{\Delta E_p}{T} \qquad 2.24$$

and the free energy of the reaction for a given temperature becomes

$$\Delta G_1^{\ddagger} = \Delta H_1^{\ddagger} - T\Delta S_1^{\ddagger} \quad . \qquad 2.25$$

While the rate of the chemical reaction is determined by the free energy of the reaction, the change in entropy can provide an insight to the mechanism of the reaction.

2.3. Application of the Theory of Absolute Reaction Rates to Thermal Desorption Reactions

Consider a surface in a system where the adsorption and desorption reactions are occurring simultaneously. If the gas on the surface does not change in composition and concentration with time, then the gas-surface reactions have reached a steady state. The gas reaction at the surface can be far removed from the steady state by rapidly increasing the temperature of the surface. The gas desorption reaction rate will then determine the gas composition and concentration on the surface. Thus for a desorption process

$$nA_{(ad)} \rightarrow nA^{\ddagger}_{ad} \rightarrow nA_{(g)} \qquad 2.26$$

the reaction rate expression can be given as

$$\ln\left(\frac{dA}{dt}\right) = \ln\left[\frac{k_1^{\,1}\,(A)^{n'}\,F_{\ddagger}}{F_a^{\,2}}\left(\frac{k}{h^{\frac{1}{2}}}\right)\right] + \ln T - \frac{\Delta E_p}{RT} \qquad 2.27$$

and then by rearrangement and differentiation with respect to (1/T), the experimental activation energy can be expressed as

$$\Delta E_p = \frac{R\, d\left[\ln\left(\frac{(-dA/dt)}{(A)^{n'}\,T}\right)\right]}{d\,(1/T)} . \qquad 2.28$$

The standard heat of activation ($\Delta H_1^{\ddagger}$) in terms of the experimental activation energy ΔE_p was expressed by equation 2.23. Before the standard heat of activation can be determined, however, a convenient standard state must be chosen.

It is customary[10] to express the heat of adsorption on a metal surface in terms of the initial heats of adsorption; i.e., at low surface coverages where the heat of adsorption is independent of the coverage. A convenient standard state for the desorption reaction would also be at a low surface coverage and where the free energy of the reaction is independent of surface concentration.

Equation 2.23 becomes

$$\Delta H_1^{\ddagger} = \Delta E_p - RT_o \qquad 2.29$$

where T_o is the surface temperature at which the free energy of the reaction is independent of the surface concentration.

The change in the entropy for the desorption reaction can be determined from

$$\Delta S^{\ddagger} = R \left[\ln \left(\frac{-dA}{dt} \right)_{T=T_o} - \ln \left(k_{1n'}^{1} A^{n'} \right) - 1 \right] + \frac{\Delta E_p}{T_o} \qquad 2.30$$

when n′ is 1, the constant k_{11}^{1} will have the units of sec^{-1} and an numerical value of between 0 and 1. The constant k_{12}^{1} for the second order reaction, i.e., when n′ is two, will have the units of $sec^{-1}\ cm^{-2}$ $molecules^{-1}$ and an assumed numerical value of 10^{-15}.

The desorption free energy for the reaction $\Delta G_1^{\ddagger}$ can now be determined from

$$\Delta G_1^{\ddagger} = \Delta H_1^{\ddagger} - T_o \Delta S_1^{\ddagger} \quad . \qquad 2.31$$

2.4. Interpretation of the Thermal Desorption Data

When the temperature of a metal surface is rapidly increased or "flashed", the pressure increase in the system is dictated by a competition between the rate at which the gas enters the system and the rate at which it is removed. Such a reaction is illustrated by Fig. 1. The mass balance for the system during the flash is given as

$$V\left(\frac{dN}{dt}\right) = R_F - NS_F + F_L - NS_E \qquad 2.32$$

where V denotes the volume of the system, R_F is the rate of the gas evolution from the metal surface, F_L represents the leak rate into the system, S_F is the rate at which gas is readsorbed on the metal surface, S_E is taken as the rate at which gas is removed from the system or the total pumping speed, and N is the gas density. As stated in the previous section, when the temperature of the surface is increased rapidly enough, the desorption rate R_F will determine the concentration and composition of the adsorbed gas species on the surface[14]. If the numerical values NS_F and F_L are small compared to R_F and NS_E then equation 2.32 reduces to

$$V\left(\frac{dN}{dt}\right) = R_F - NS_E \; . \qquad 2.33$$

Equation 2.33 can also be expressed as

$$KV\left(\frac{dP^*}{dt}\right) = -\left(\frac{dn}{dt}\right) - KS_E P^* \qquad 2.34$$

where n is the number of adsorbed gas species on the surface, K is a

constant, and P^{*15}_t is defined by[15]

$$P^*_t = P - P_{eq} \quad . \qquad 2.35$$

P_{eq} is the equilibrium pressure of the system at a moment just before the "flash", and P is the pressure of the system at some time during the "flash".

Upon examination of Fig. 1 it can be seen that a maximum occurs in the pressure-time plot at a time (t_m), and at this instant, equation 2.34 simplifies to

$$\left(\frac{-dn}{dt}\right)_{t_m} = KS_E P^*_{t_m} \quad . \qquad 2.36$$

Equation 2.34 can be rearranged to give

$$\left(\frac{-dn}{dt}\right) = K V \left(\frac{dP^*}{dt}\right) + K S_E P^* \quad . \qquad 2.37$$

By multiplying equation 2.37 through by the term $\left(\frac{dn}{dt}\right)_{t_m} \Big/ (K S_E P_{t_m})$, the rate of desorption, at any time t, can be expressed as

$$\left(\frac{dn}{dt}\right)_t = \left(\frac{dn}{dt}\right)_{t_m} \left[\frac{V}{S_E P^*_{t_m}} \left(\frac{dP^*}{dt}\right)_t + \frac{P^*_t}{P^*_{t_m}} \right] \qquad 2.38$$

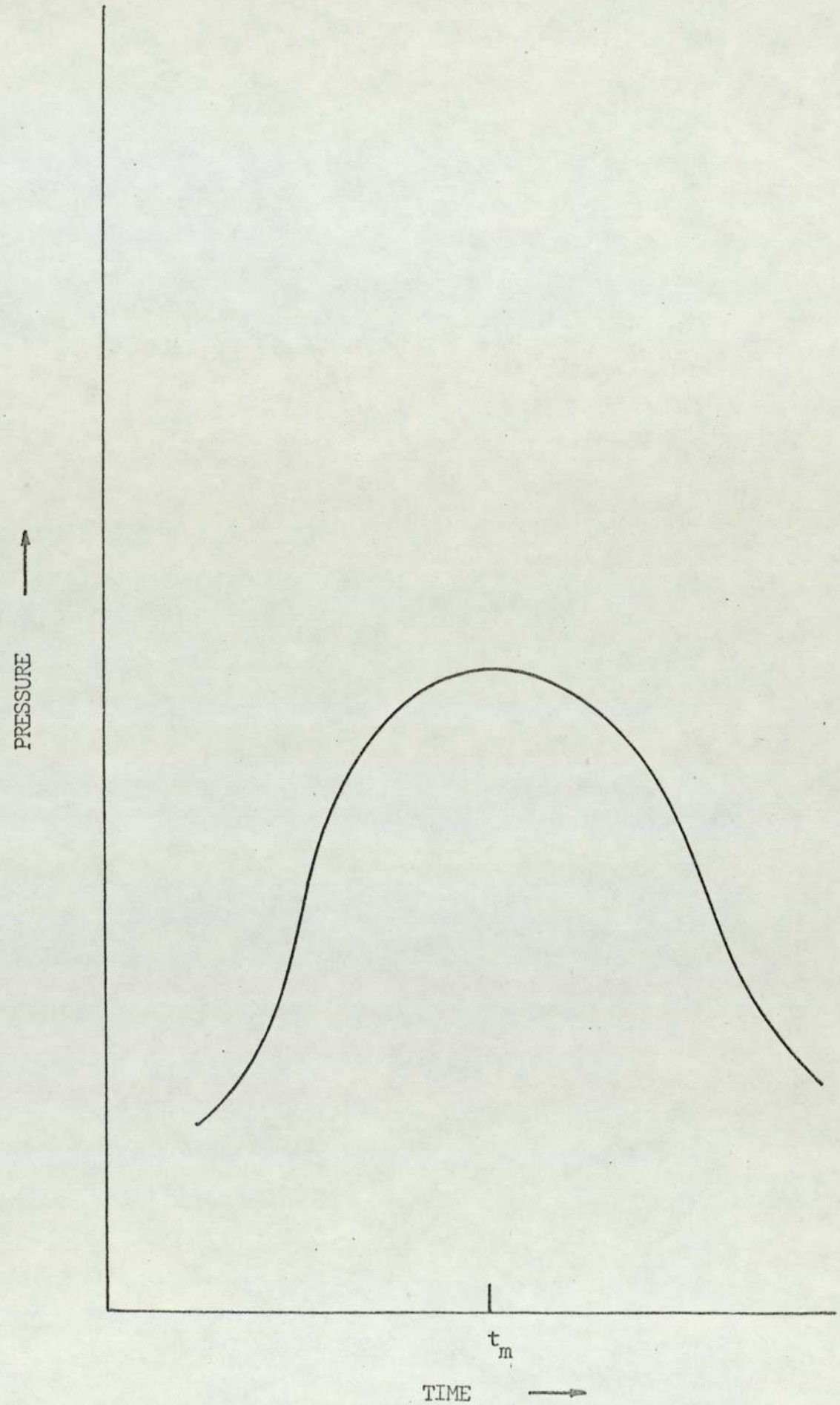

Fig. 1. Desorption of gases from a metal surface.

If equation 2.37 is integrated, then the initial coverage of the surface is given by

$$\sigma_o = \int_o^{t_K} \left(\frac{dn}{dt}\right)_t dt \qquad 2.39$$

where t_K represents the time at which $\left(\frac{dn}{dt}\right)$ approaches zero. The number of adsorbed gas species on the surface at any time between the time interval 0 and t_K can be found by solving

$$(\sigma_o - \sigma_t) = \int_o^{t_K} \left(\frac{dn}{dt}\right)_t dt - \int_o^{t} \left(\frac{dn}{dt}\right)_t dt \,. \qquad 2.40$$

The experimental activation energy for the desorption reaction of the nth order is given as

$$\Delta E_p = \frac{R\, d\left[\ln \dfrac{(dn/dt)_t}{(\sigma_o - \sigma)^n T}\right]}{d\,(1/T)} \,. \qquad 2.41$$

The standard state for the desorption reaction has been defined in section 2.3. This state will occur on the surface as some time t_o. Fig. 2 is a typical plot of the desorption rate from the metal surface as a function of time. The time t_o, illustrated in Fig. 2, is defined as that time when the desorption rate is one half the maximum desorption rate and the sign of $\frac{d\bar{P}^*}{dt}$ is negative. T_o can be determined from a

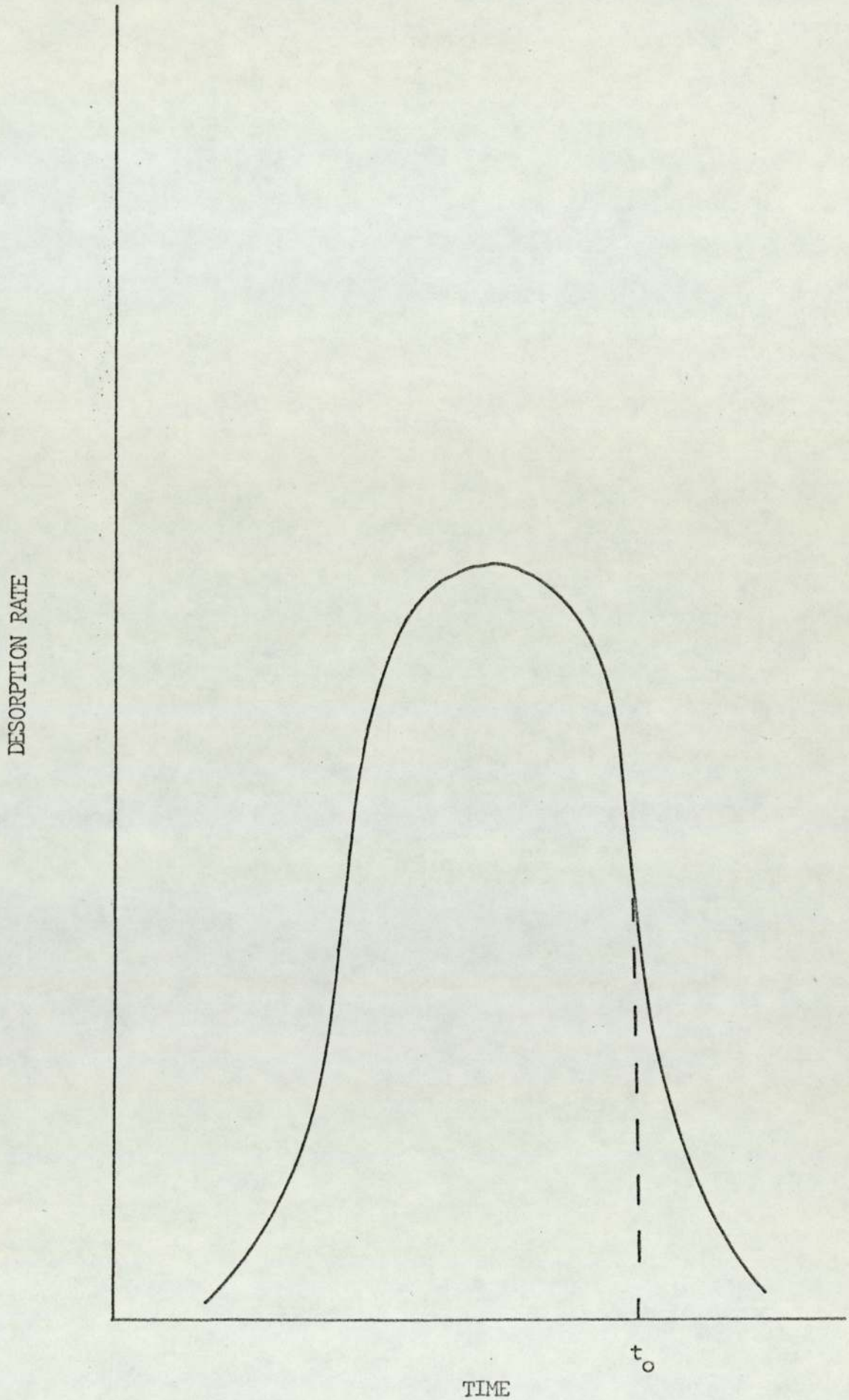

Fig. 2. A typical plot of the desorption rate as a function of time.

knowledge of the surface temperature as a function of time. The standard heat of activation, the change in entropy, and the standard free energy of the desorption reaction can now be determined by substitution of T_o into equations 2.29, 2.30, and 2.31 respectively.

2.5. The Experimental Techniques and Apparatus used in Thermal Desorption Studies

The amount of knowledge about the chemistry of the gas-metal surface interaction by rapidly heating the surface and desorbing the gas is indeed impressive. Yet, unless strict attention is given to the experimental techniques and the equipment used, the results from such experiments can be misleading. This section will be concerned with what is thought to be the most important aspects of the experimental techniques and equipment.

2.5.1. Required information

The thermal desorption reaction experiment consists of permitting gas to adsorb on to a metal surface and then drive the gas off by rapidly heating the filament. However, before any quantitative kinetic information can be obtained about the reaction, the experimental results must provide the following information:

1. The pumping speed of the system for the gases involved in the desorption reaction.
2. The gas density of the system as a function of time.
3. The temperature of the metal surface as a function of time.

The total pumping speed of a vacuum system is the sum of all the various modes of pumping. These modes include not only the vacuum pump itself, but pumping due to pressure measuring devices and the adsorption of the desorbed gas species on various surfaces contained within the vacuum system. The pumping speed is defined by the equation[16]

$$\frac{-dP}{dt} = \frac{S}{V} (P - P_s) \qquad 2.42$$

where S is the pumping speed in litres/sec., and P_s is the ultimate lowest pressure. For a range of pressures where S is independent of the pressure, equation 2.42 can be integrated to give

$$S = \frac{V}{\Delta t} \Delta \left[\ln (P - P_s) \right]. \qquad 2.43$$

Should $P >> P_s$, then from equation 2.43 the pumping speed can be expressed as

$$S = \frac{V}{t_2 - t_1} \ln \left(\frac{P_1}{P_2} \right) \qquad 2.44$$

where P_1 and P_2 represent the pressures at the beginning and the end of a time interval defined by $(t_2 - t_1)$.

The observed form of the desorption spectra or gas density as a function of time will be dependent upon the pumping speed of the system and the rate at which the temperature of the filament is increased.

For a closed system, i.e., where the pumping speed approaches zero, the desorption spectra will have a form similar to that shown in Fig. 3. Since Fig. 3 represents the desorption spectra for a

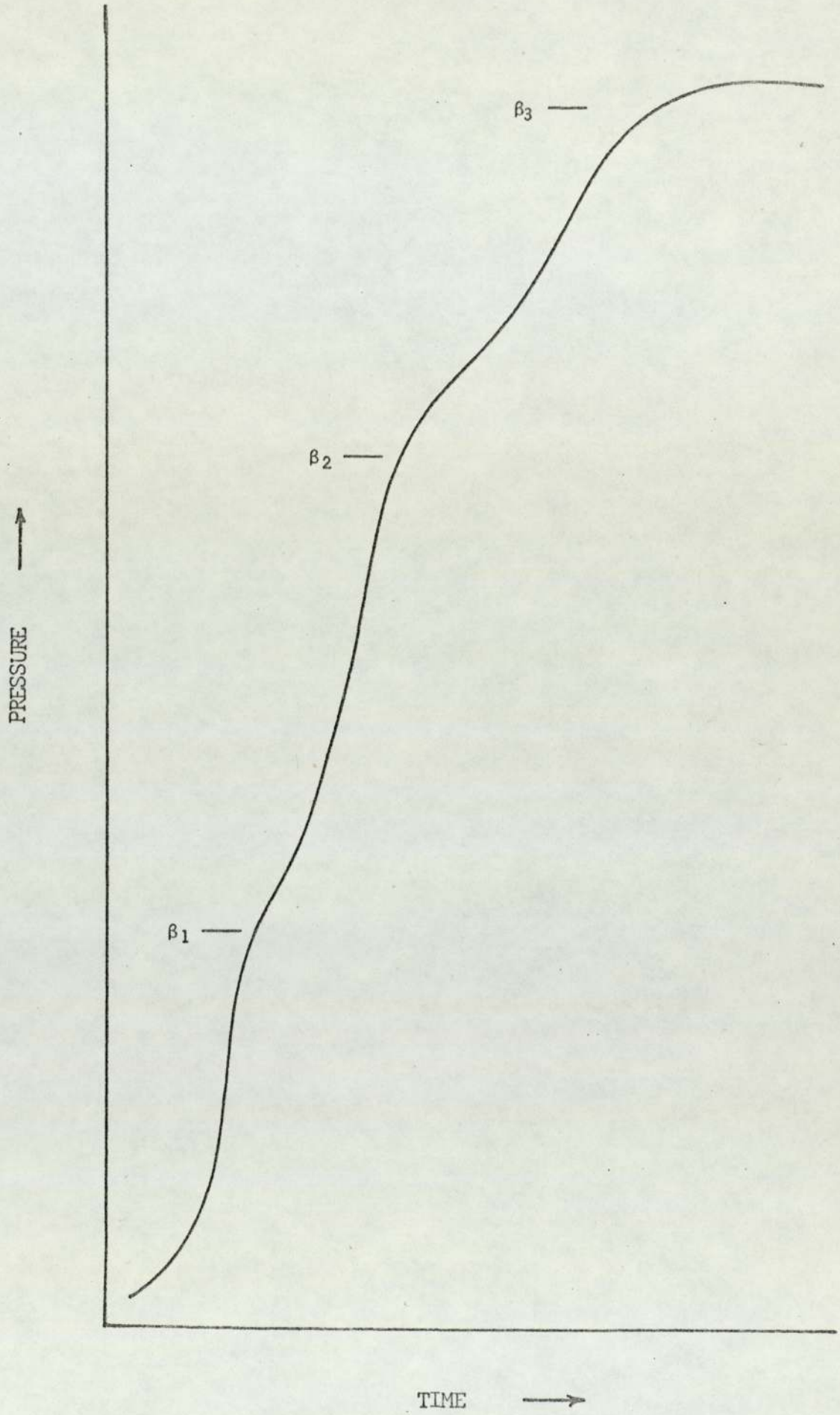

Fig. 3. Thermal desorption spectrum for a closed system.

single gas species adsorbed on the surface, the structure in the desorption spectra indicates that the gas was adsorbed in several states and each state required a different desorption energy. With the pumping speed of the system approaching zero, equation 2.37 becomes

$$\frac{-dn}{dt} = K V \left(\frac{dP^*}{dt}\right) \qquad 2.45$$

and the initial surface coverage is

$$\sigma_o = K V P^*_{max} \qquad 2.46$$

where P^*_{max} is the maximum pressure.

A flow system exists when the pumping speed $S > 0$. The effect of pumping speed on the desorption spectra for a constant heating rate is illustrated by Fig. 4. Comparison of Figs. 4 and 3 reveals that a better resolution of the individual peaks can be obtained from the flow system than from the closed system. In order to obtain quantitative information from the desorption spectra, the pumping speed of the system must be known [17].

The rate at which the temperature is increased will effect the resolution of the desorption spectra from both the closed and the flow system. An increase in the heating rate will cause the individual desorption peaks to coalesce and make quantitative analysis of the individual peaks more difficult. The resolution of the peaks, for a given heating rate, can be increased to some extent by increasing the sweep rate of the recording instrument. This is limited, however, by the response time of the pressure measuring circuit.

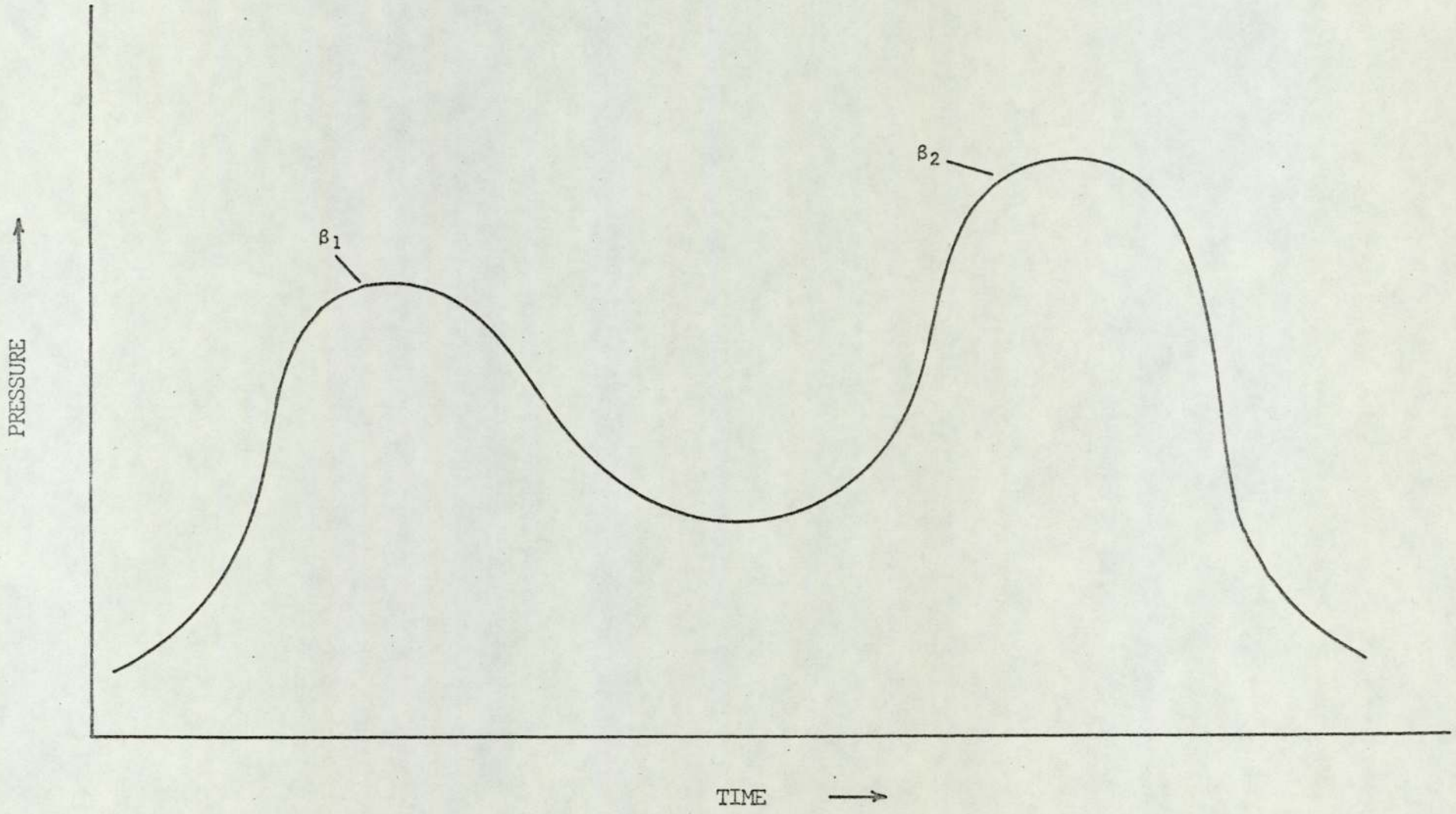

Fig. 4. Thermal desorption spectrum for an open system.

The last and most important parameter is the temperature of the metal surface as a function of time. Since the temperature as a function of time does not appear in any of the rate expressions in sections 2.2, 2.3, or 2.4, its exact form is not important other than that the instantaneous first derivation of the function should be at all times equal to or greater than zero.

The most common method of increasing the temperature of the surface is by resistance heating[17-20], i.e., the power stems from the I^2R product generated across a metal filament. There are two important consideration that should be borne in mind when using this form of heating technique. First, the filament should be of sufficient length so that the portion of the filament where the temperature variation is the greatest, because of heat losses to the contact supports, will represent only a small fraction of the total filament. G. Ehrlich[17] has studied the temperature variation along a filament under conditions where the temperature in the middle portion of the filament was increased rapidly with time or was held constant over a period of time. The result of this investigation showed, that as the temperature was increased, the temperature variation along the filament whose temperature was changing rapidly with time was significantly more uniform over a larger portion of the filament than that for the filament held momentarily at a steady state.

The temperature of the filament at any instant during a "flash" can be determined from the measurement of the instantaneous filament resistance. The instantaneous resistance is obtained from the ratio of the voltage across the filament and the filament current at a time (t) during the "flash". From a knowledge of the composition of the filament and its physical dimensions, the temperature of the filament at a time (t) can be determined from the temperature dependence of

resistivity of the filament material. G. Ehrlich[17] has warned, and rightly so, that because there is a temperature variation across the filament during the flash, there will also be a resistance variation. However, for a filament of sufficient length the end corrections can be considered well within the experimental error.

2.5.2. Detection of the desorbed gases

There are basically two types of pressure gauges commonly used to detect the gases being desorbed during a thermal desorption experiment. The first type is known as a total pressure gauge and determines the pressure by ionizing a fraction of the gases in the system. There are two forms of this type of gauge, and each form determines the pressure by measuring the positive ion current resulting from the impact of energetic electrons with the gaseous species in the system. The intensity of the positive ion current for a given density of a gas species will be dependent on the total ionization cross-section. The total ionization cross-section is a function of the electron energy. For most gases a maximum in the value of the ionization cross-section occurs for electron energies of about 100 ev[21]. Since the magnitude of the ionization cross-section will vary from gas to gas, with helium having one of the lowest values, the true total pressure of the system can only then be determined if the composition of the gas is known and the appropriate corrections are made.

The Bayard-Alpert gauge is perhaps the most commonly used gauge in flash desorption studies. The electrons from this form of gauge are generated by means of thermionic emission from a hot metal filament. Upon being accelerated to a grid, the electrons ionize a portion of the gas within the gauge. Although this form of a total pressure

gauge responds well to small changes in gas density within the system, it does suffer from two inherent burdensome features.

1. When electrons strike the grid, there is a possibility that a soft x-ray will be emitted. These soft x-rays in turn interact with the negatively biased ion collector surface so as to produce a photoemission current. The effect of this photoemission current on the pressure measurement becomes most pronounced at pressures less than 10^{-8} torr. The photoemission current at low pressure can often equal or exceed the positive ion current of the collector and thus prevent any accurate pressure measurement.

2. The hot incandescent filament used in the Bayard-Alpert gauge can itself interfere with the results of a "flash" desorption experiment. The gauge filament surface can be responsible for the decomposition of the gas under investigation. For example, the surface of the gauge filament often contains carbon as a result of the decomposition of hydrocarbons. This carbon can then react with oxygen to form carbon monoxide. Thus, the introduction of pure oxygen into a flash desorption system will result in the adsorption and desorption of oxygen and carbon monoxide from the metal surface under investigation.

The second form of a total pressure gauge that is often used in thermal desorption studies is generally known as a Penning gauge. This form of a gauge operates on the principle that the electron path between the anode and cathode is greatly increased by the presence of

crossed magnetic and electrostatic fields. The electrostatic field is generated by the formation of an electron space charge on an axis parallel to the anode surface and at right angles to the applied magnetic field. The potential of the electron space charge is near that of the applied cathode voltage. As a result of these crossed fields, the electrons will move in a radial path. This path will increase in radius after each inelastic collision with a molecule until the path of the electron intercepts the anode surface. Some of the latter inelastic collisions between the electrons and the gas will result in the ionization of the gas molecules. The detached electrons, as a result of the ionization reaction, will become part of the electron space charge, while the positive ions will be collected at the cathode surface. The pressure of the system is determined from the ion current.

This form of a total pressure gauge is useful in flash desorption studies because its operation does not depend on the continuous operation of a hot incandescent metal filament and the pressure measurement is not x-ray limited. The chief disadvantages of this form of gauge is that the pumping speed is usually much greater than that of the Bayard-Alpert gauge[21] and the ion current can vary non-linearly with pressure.

The second type of pressure measuring instrument is called a partial pressure gauge. Partial pressure gauges used in flash desorption studies are commonly known as mass spectrometers. This type of gauge is similar to that of the Bayard-Alpert gauge in that it detects the pressure of the gas from the ion currents. These ion currents are a result of inelastic collisions between energetic electrons emitted from a hot filament and the molecules in the system. Thus, this type of device will suffer with the same inherent dis-

advantage as does the Bayard-Alpert gauge. The primary advantage of this type of gauge is that the partial pressures can be determined by passing the gaseous ions through an electric or magnetic analyser. The analyser separates the ions according to their charge to mass ratios. It is, therefore, possible to obtain a mass spectrum of the desorption peak.

In general, the mass range must be scanned by changing the potential of an electrostatic plate or the intensity of a magnetic field. The magnetic field deflection instruments can perhaps make only two or three scans/sec. In view of the fact that the flash times are about one second in duration, the usefulness of the magnetic scan instrument is rather doubtful. Scan rates as high as 100 KHz for a time of flight mass spectrometer with a 60 cm long drift tube have been reported[21], and an instrument of this type would be capable of determining the entire mass spectrum throughout the entire flash.

2.5.3. Vacuum pumps

2.5.3.1. Diffusion pumps. Mercury and oil diffusion pumps are commonly used for the production of ultra-high vacuum pressures. These pumps operate on the principle of the bombardment of the gas molecules with energetic oil or mercury vapours which provides the gas with a preferred velocity. By the use of these pumps, pressures below 10^{-9} torr can be obtained. Their chief disadvantage, as far as their use in a flash desorption system is concerned, is that in spite of the use of traps and baffels between the pump and the system, oil or mercury can find its way back into the reaction chamber. The decomposition of oil on the surface of the flashing filament will not only alter the surface characteristics of the filament, but also the

composition of the gas species desorbing from the surface. Thus the desorption spectra could be severely altered by the contamination from the diffusion pump.

2.5.3.2. Turbo-molecular pump. This pump consists of a horizontal housing that contains a series of annular rings comprised of fixed slotted blades that are uniformly spaced from one another. A rotatable cylinder is contained within the housing, and its annular rings occupy the space between the rings of the housing. The clearance between the two sets of rings is very close, and when the cylinder is rotated at about 16,000 revolutions/minute, the molecules within the rings are given a preferred momentum by repeated collisions with the rapidly moving rings[21]. These pumps are capable of producing pressures as low as 1×10^{-11} torr. Their chief disadvantages, besides their high cost, are that they are not very effective in removing water vapour and hydrocarbon oil from the cylinder bearing can find its way back into the main vacuum system.

2.5.3.3. Sorption pumps. These pumps can produce system pressures as low as 1×10^{-8} torr by the physical adsorption of the gases on a cooled surface. The materials used in these pumps are commonly referred to as molecular sieves, or zeolites which are generally dehydrated crystalline alumino-silicates[21]. The original structure of these silicates is such that upon dehydration a system of internal cavities, interconnected by pores, permeates the entire material[22] and provides a large surface area. The dimensions of the pore is dependent on the chemical composition of the zeolite. Potassium alumino-silicates have pore diameters of 3 $\mathring{A}$, while sodium alumino-silicates have pore diameters of 10 $\mathring{A}$. The pumping performance of a pump will depend on the composition of the gas and the zeolite,

i.e., a zeolite can not effectively reduce the partial pressure of a gas whose molecular diameter exceeds that of the pore diameter. In general most commercial zeolites are effective in removing most gases except for inert gases like helium and neon. The chief advantage of using this form of pump in a flash desorption system is that it does not constitute a source of hydrocarbon contamination.

2.5.3.4. Sublimation pumps. A sublimation pump operates by the adsorption of gases on to a cooled metal surface. The surface used in this pump is a deposited metal film of titanium, molybdenium, tantalum, or tunsten. When the gas surface coverage approaches a monalayer, another metal layer is deposited. This will not only bury the adsorbed gases on the previous surface, but also provide a clean metal surface for further gas adsorption.

The pumping speed of the pump will depend on the sticking coefficient of the particular gas species, the effective surface area of the metal deposit, and the temperature of the surface. The pumping speed per unit area of a metal deposite of titanium at liquid nitrogen temperature is quite high for gases such as oxygen, nitrogen, hydrogen, carbon monoxide, and water vapour. Gases such as helium, neon, and methane are much more difficult to remove with this type of pump. This pump, like the sorption pump, will not constitute a source of hydrocarbon contamination.

2.5.3.5. Getter ion pump. The getter ion pump is modelled after the Penning type pressure gauge, except that the pump cathode is constructed of titanium. In the operation of the Penning gauge, the ions that strike the surface of the cathode are desorbed as neutral atoms or molecules. With the getter ion pump, however, the energy at which the ions impact the cathode surface is sufficient not only to bury the ion

in the interior of the cathode, but also cause cathode atoms to leave the surface as a result a transfer of momentum between the impinging ion and the surface atoms. The latter process is known as sputtering. The sputtered cathode material will deposite on other surfaces of the pump and thus constitute a form of sublimation pump. The getter ion pump is generally not a source of hydrocarbon contamination and can be operated at ambient room temperature or at elevated bake out temperatures.

2.5.4. Construction of the vacuum system

While it is not necessary to go into all the details of the construction of an ultra-high vacuum system suitable for thermal desorption studies, there are a few major considerations which should be borne in mind.

1. The desorbed gases from the filament will make a number of collisions with the walls and surfaces contained within the system before reaching the pressure gauge. Reaction of the gases with these surfaces could lead to errors in the determination of the rate and composition of the gases. For example, atomic hydrogen adsorbs strongly on glass walls[19] and thus glass surfaces should be avoided in a system studying the desorption reaction of hydrogen from a metal surface.

2. The placement of the pressure measuring gauge too near the flashing filament could lead to erroneous measurements. By placing the gauge some distance from the desorption chamber, the conductance of the connecting tube must be taken into consideration. As a result of the rapid increase in the surface temperature of the metal there will be a

sudden increase in the pressure at one end of the connecting tube. Now by assuming a Maxwellian distribution of gas velocities, it is important that the average time for the gas to reach the gauge must be much shorter than that of the flash duration. Let C^{ll} represent the conductance of the connecting tube of a length l and a radius a, then the average time required for a gas molecule to reach the gauge would be

$$\bar{t} \approx \frac{\pi a^2 l}{4\left[1 + \frac{3l}{8a}\right] C} \quad . \qquad 2.47$$

Consider that a and l have values of 1 cm and 100 cm respectively and the conductance ^{ll} C of the tube is given as 100 cm^3/sec., then upon substitution of these values into equation 2.47 the average transit time for the molecule will be about 20 milliseconds. For a flash duration of one second, the above transit time is well within the experimental error. While the above example represents a rather extreme case for an all metal system, it does point out that for some glass systems using narrow bore tubing, the transit time could be increased and thus introduce a considerable error in the correlation between the filament temperature and the desorption spectrum.

3. The last point of consideration in the construction of the vacuum system is that during the design and construction of the system provision should be made for heating the system to an elevated temperature for some period of time. This heating of the system or baking will help to desorbe gases from various internal surfaces of the system and thus reduce the internal leak rate.

CHAPTER 3

THE ELECTRON WORK FUNCTION

3.1. Introduction

It has been established for a number of years that the electron work function of a metal surface is effected by the presence of adsorbed gas species[23-26]. Hence, the measurement of the work function of a conductor surface is an essential part of the study of a gas-surface interaction.

The following sections will consider the nature of the electron work function of a conductor surface; the applicability of the method of determining the work function with regard to a gas-surface interaction; and the effect that a patchy surface has on the work function measurement. The vacuum requirements will not be considered for they will be the same as for the desorption studies of the previous chapter.

3.2. The Electron Work Function

The "true" work function $e\chi$ for a homogeneous surface of a conductor is defined as[23]

$$e\chi = - e\phi_a - \bar{u} \qquad 3.1$$

where $e\phi_a$ is the electrostatic potential energy in the vacuum just outside the conductor surface and $\bar{u}$ is the electrochemical potential. The electrochemical potential can be expressed as

$$\bar{u} = \left(\frac{\partial F}{\partial n} \right)_{T,V} \qquad 3.2$$

where n is the number of electrons, V is the volume and F is the

Helmholtz free energy of the electron. In terms of the total energy of the system the electrochemical potential becomes

$$\bar{u} = \left(\frac{\partial E}{\partial n}\right)_{S,V} \quad . \qquad 3.3$$

where S is the entropy.

From the method of Wigner and Bardeen[23], the energy of the system may be evaluated for some metals by using the self-consistent field solution to the wave equation. At absolute zero the total energy[23] of a volume of metal, i.e., relative to the state of separated ion cores and electrons, is expressed as

$$E = \Sigma(\varepsilon_i) - \text{coulomb energy} - \text{exchange energy} - \text{correlation energy} + E_1 \qquad 3.4$$

where E_1 is the interaction energy between ion cores of the volume and ε_i represents the energy parameters for a single electron that is moving in a field of ion cores and the coulomb field as a result of the rest of the electrons. The mathematical expressions for the exchange and correlation energies per electron can be assumed. After multiplying the latter two energy terms by n, the number of electrons per unit volume, the total exchange and correlation energies are substituted into equation 3.4. By taking the partial derivative of equation 3.4 with respect to n we obtain,

$$-\left(\frac{\partial E}{\partial n}\right)_V = -\bar{u} = -\varepsilon_{max} + \frac{Ae^2}{r_e} + \frac{Be^2}{(r_e + CR_B)} + \frac{De^2 r_e}{(r_e + CR_B)^2} \qquad 3.5$$

where r_e represents the radius of a volume that is defined as the metal

volume per free electron, C is a constant, and R_B is the Bohr radius. The first energy term in equation 3.5 represents the energy of the electron at the top of the Fermi distribution, the second energy term gives the exchange energy correction, while the last two terms are the correlation corrections.

Now on substitution of equation 3.5 into equation 3.1, the true work function of the metal surface at absolute zero can be expressed as

$$e\chi = -e\phi_a - \varepsilon_{max} + \frac{Ae^2}{r_e} + \frac{Be^2}{(r_e + CR_B)} + \frac{De^2 r_e}{(r_e + CR_B)} \quad . \qquad 3.6$$

The difference between the first two terms of equation 3.6 will be dependent on the double layer[27] of the surface. The double layer results from the spreading out the electron distribution and has the effect of producing a dipole moment per unit area. This spreading out of the electrons will have the effect of lowering the kinetic energy of the electron and increasing its potential energy. The potential energy increase is mainly a result of the last three terms in equation 3.5, i.e., the exchange and correlation energy corrections. Therefore, the average interaction energy of an electron will increase as the electron density decreases. The exchange and correlation energies are related to the total energy of the electron that is necessary to overcome the image force $(e^2/(4x^2))$ which acts on the electrons at large distances from the surface.

3.3. Basic Techniques for the Determination of the Electron Work Function of a Surface

This section will be a discussion of the four basic techniques for the determination of the electron work function of a conductor surface, i.e., thermionic emission, photoelectric emission, field emission, and the contact potential difference. A major consideration in the discussion of each of these various techniques will be its applicability to the study of a gas-metal surface interaction.

3.3.1. Thermionic emission

The saturated thermionic emission current density from a conductor surface is generally expressed by the Richardson-Dushman equation as

$$J = A(1 - r_e)\ T^2 \exp(-e\chi/kT) \qquad 3.7$$

where J is the current density in amperes/cm^2, A is a constant that is equal to $4\pi mk^2e/h^3$ or 120 amperes/cm^2/deg^2, and r_e is the zero field reflection coefficient. The Richardson-Dushman equation can be derived either from a thermodynamic[23] or a kinetic[28] argument. J.C. Riviere[29] has pointed out that the two most important criteria that must be met before equation 3.7 is valid are (a), the surface of the conductor must be uniform and (b), the electric field necessary for current saturation must be so weak it can be set to zero.

By now taking the total differential of the rearranged logrithmic form of equation 3.7 and then dividing through by the term (dT) we obtain

$$\frac{d\ \ln(J/T^2)}{dT} = \frac{dr_e}{(1 - r_e)\,dT} - \frac{d(e\chi)}{kT\,dT} + \frac{e\chi}{kT^2} \qquad 3.8$$

and since

$$\frac{-dT}{d\,(1/T)} = T^2 \qquad 3.9$$

equation 3.8 becomes

$$\frac{-k\,d\,\ln(J/T^2)}{d\,(1/T)} = \frac{kT^2}{(1-r_e)} \times \frac{dr_e}{dT} - \frac{T\,d\,(e\chi)}{dT} + e\chi \,. \qquad 3.10$$

The term $\dfrac{-k\,d\,\ln(J/T^2)}{d\,(1/T)}$ can be determined experimentally and is generally known as the "apparent" work function $e\chi^*$. Therefore, equation 3.8 can be expressed as

$$e\chi^* = e\chi + \frac{kT}{(1-r_e)} \times \frac{dr_e}{dT} - \frac{T\,d\,(e\chi)}{dT} \qquad 3.11$$

where $e\chi$ now represents the work function of the surface at absolute zero, and the last two terms are corrections for the temperature dependence of the reflection coefficient and work function, respectively.

The value of A in equation 3.7 can be determined from the experimental plot of the $\ln(J/T^2)$ as a function (1/T) as (1/T) approaches zero.

The most essential point about the above discussion of determination of the work function by the thermionic emission technique is that the temperature of the metal surface must be varied. In section 2.3 it was pointed out that by increasing the temperature of the surface, the composition and concentration of the adsorbed gas species could become solely dependent on the desorption reaction rate.

In section 3.2., it was shown that the work function of a surface is strongly influenced by the first few atomic layers on the surface. Hence, an attempt to study the effect of the electron work function on a gas-metallic surface interaction by the thermionic emission technique is not feasible.

3.2.2. Photoelectric emission

The process of electron emission as a result of light striking a metal surface is generally known as photoemission. Experimentally the photoemission current from the metal is a function of the surface temperature and the light frequency[30]. It is also observed that electron emission occurs only when the light frequency exceeds a lower limit known as the threshold frequency $h\nu_o$.

Consider now the photoemission from a metallic single crystal surface held at T=0. At this temperature, all of the electron energy levels in the Fermie distribution are filled. The minimum energy ($h\nu_o$) to remove an electron from the surface would then be that required to remove an electron from the top of the Fermie distribution. The work function of the surface is thus given as

$$e\chi = h\nu_o \qquad 3.12$$

where ν_o is the threshold frequency. Under these temperature conditions the onset of a photoemission current would be sharp as the light frequency was varied through the threshold value.

The rate of photoemission from a surface will not only be dependent on the light intensity, but also on the number of electrons of suitable energy (N_e) that strike the surface per unit area per unit time. There is a finite probability that these electrons will interact with the radition and acquire a proper momentum normal to

the surface[30]. R. H. Fowler[30] has shown that for N_e electrons having a momentum range between p and p + dp normal to the surface, the ratio of the photoemission current density to the temperature can be expressed as

$$\ln\left(\frac{J}{T^2}\right) = \ln (B k^2) + f (h\nu - e\chi)/kT \qquad 3.13$$

where f is a known function and B is a constant for a narrow range of frequencies near the threshold frequency.

From equation 3.13, R. H. Fowler[30] determined the work function of the surface by first plotting the $\ln(J/T^2)$ as a function of $h\nu/kT$, when T was held constant. A plot of ln (f) as a function of $\frac{h\nu - h\nu_o}{kT}$ was then made and the two plots were then superimposed by shifts along both axis. The magnitude of the shift along the $\ln(J/T^2)$ axis represented $\ln (Bk^2)$, while a shift along the $h\nu/kT$ axis will give $h\nu_o/kT$. Since T was constant, $e\chi$ can be determined by the use of equation 3.12.

A second method for obtaining the work function of a conductor surface from equation 3.13 was proposed by L. A. Du Bridge[31]. In this method the light frequency was held constant and it was the temperature of the surface that was varied. This method is experimentally superior to that suggested by R. H. Fowler[30], because this method is not subject to current density variations as a result of changes in light intensity with changes in light frequency.

The L. A. Du Bridge method[31], like that of the R. H. Fowler method, requires an experimental and theoretical plot to determine the work function. The experimental plot if the $\ln(J/T^2)$ as a function of (1/T) and the theoretical plot is the ln (f) as a function of

$\ln \frac{(h\nu - h\nu_o)}{kT}$. The plots are again superimposed by shifts along both axis and once again Bk^2 and $e\chi$ are obtained. Should B or $e\chi$ be significantly temperature dependent then the superimposing of the two plots would be difficult.

The photoelectric emission method for the determination of the work function of a surface is useful for temperatures not exceeding 1100 K. At higher temperatures, the photoelectric current becomes obscure by the substantial increase in the thermionic emission current. The photoelectric method can be used in the study of gas-metal surface reaction[32-35]; however, the R. H. Fowler method is preferred since the temperature of the surface is held constant and the concentration and composition of the adsorbed gas species are not altered as a result of the method of measuring the work function.

3.3.3. Field Emission

As the strength of the electric field at the surface of a metal conductor is increased to about 10^{+4} volts/cm, the probability of an electron being emitted from the surface is also increased. The current density for high field emission is given by[23]

$$J = \frac{1.55 \times 10^{-6} E^2}{\theta^2 e\chi} \exp\left[\frac{-6.838 \times 10^{+7} \theta (e\chi)^{3/2}}{E}\right] \text{ amperes cm}^{-2} \qquad 3.14$$

where E is the electric field strength in volts per cm, J is the emission current density in amperes cm^{-2}, and θ is a very slowly varying function of the field E and the work function $e\chi$. If

equation 3.14 is differentiated with respect to 1/E we obtain

$$\frac{d \ln(J/E^2)}{d (1/E)} = S = -6.838 \times 10^{+7} \theta (e\chi)^{3/2} \quad . \qquad 3.15$$

The value of S in equation 3.15 will be mainly dependent on the value of the work function $e\chi$.

In order to solve equation 3.15, the emission current density J and the electric field strength E must be determined experimentally. It is usually found that the exact emitting area A and the distance d between the emitter and collector are difficult to measure experimetally. For this reason equation 3.15 is generally expressed as[29]

$$\frac{d \ln(i/v^2)}{d (1/v)} = S = \frac{-6.838 \times 10^{+7} (e\chi)^{3/2}}{d} \qquad 3.16$$

where v is the applied voltage, and i is the measured electron current. Before any accurate measurement of the work function values can be determined, the values of θ and d must be known. The slowly varying function θ has been tabulated from the image potential[36]. The value of d can be determined by determining S from a surface of a known work function value[36].

The field emission method for the determination of the work function of a surface is quite applicable for studies of gas-metal surface interactions[37-41]. Since the temperature of the surface remains constant throughout the measurement, the composition and concentration of the adsorbed gas species on the surface will remain in a steady state. The upper temperature limit at which the work function can be determined will be dependent on the temperature dependence of the vapour presence of the metal surface. Work function measurements have been made on tungsten surfaces held at 2000 K[29].

3.3.4. Contact Potential Difference

Consider now that two metallic surfaces at T=0 are connected electrically, as shown in Fig. 5, through an external circuit. Let the surfaces be brought close enough so that there will be electronic interactions. In order that two such surfaces be in a state of equilibrium, their respective electrochemical potentials must be equal and hence

$$\bar{u}_1 = \bar{u}_2 \qquad 3.17$$

where the subscripts signify metal surface (1) and metal surface (2). By use of the definition of the work function given by equation 3.1, equation 3.17 can now be expressed as

$$e\chi_1 + e\phi_{a_1} = e\chi_2 + e\phi_{a_2} \qquad 3.18$$

By rearrangement, equation 3.18 becomes

$$e\chi_1 - e\chi_2 = e\phi_{a_2} - e\phi_{a_1} = V_{12} \qquad 3.19$$

where V_{12} is referred to as the contact potential difference and can have values of $0 \leq V_{12} \leq 0$. The work function of either of the metal surfaces can be obtained from equation 3.19 provided the contact potential difference is measured and the work function of the other surface is known.

3.3.4.1. Capacitor Method

The contact potential can be experimentally determined by two basic methods. The first method arranges the two metal surfaces such that they form a parallel plate capacitor. The capacitance of the capacitor is defined as[42]

$$C = \frac{K A}{4\pi d_1} \qquad 3.20$$

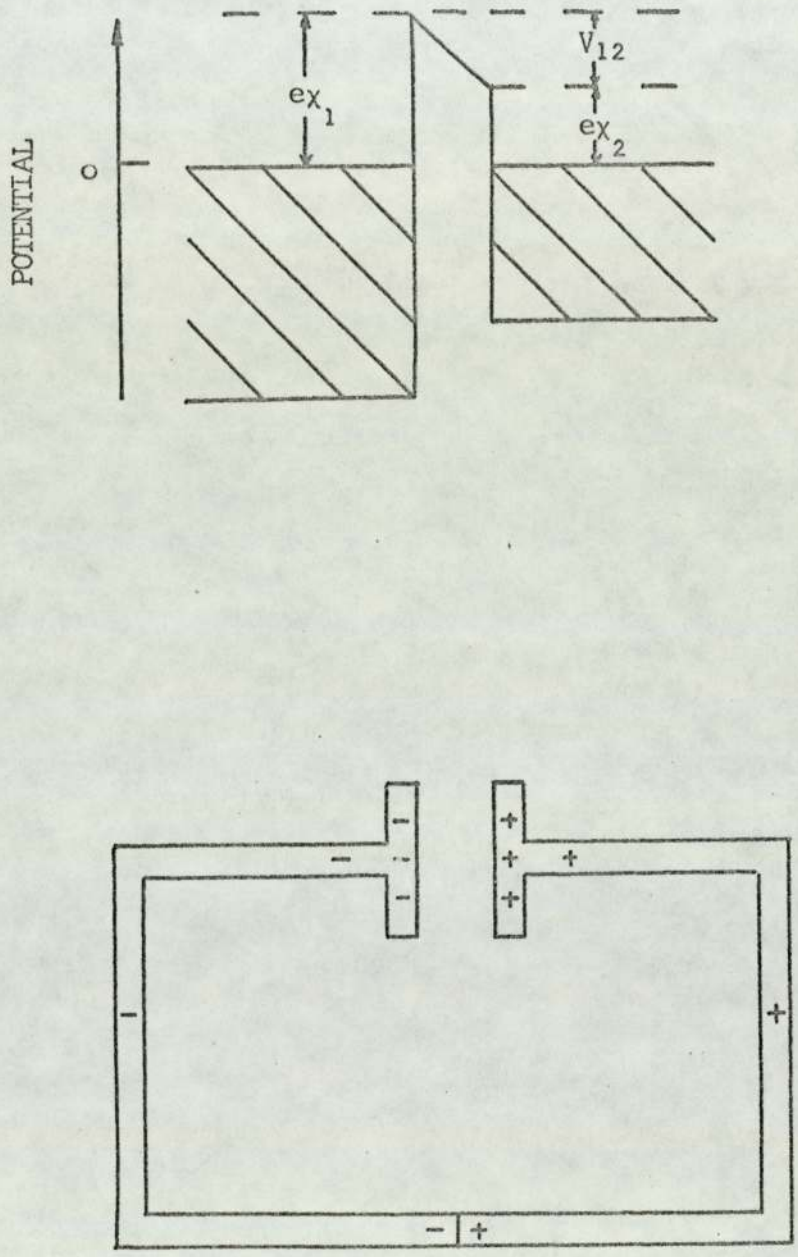

Fig. 5. Contact potential difference between two metal surfaces[2].

where A is the surface area of each of the metal surfaces, K is the dielectric constant of the medium between the plate, and d_1 is the distance separating the plate.

The charge on the capacitor, when no external voltage is applied, is given as

$$Q = C\ V_{12} \qquad 3.21$$

and

$$Q = C\ (V_{12} + V_a) \qquad 3.22$$

when a voltage of V_a is applied to the capacitor. If d_1 is a function of time then equation 3.22 becomes

$$\frac{dQ}{dt} = \frac{dC}{dt}\ (V_{12} + V_a) \qquad 3.23$$

where dQ/dt represents the current in the capacitor circuit. Thus when dQ/dt approaches zero, V_a will be equal to $-V_{12}$. The method described above is generally known as the Kelvin Method[43-44].

3.3.4.2. Electron Beam Method

The second general method for determining the contact potential difference can be classified as the electron beam method. This method determines the contact potential difference by observing the current voltage characteristic of a beam of electrons that strike a conductor surface at a normal incident[23, 29, 45].

Once again let metal (1) and metal (2) be electrically connected by an external circuit like that shown in Fig. 5. Let the temperature of metal (1), however, be increased to T_1 so that the thermionic emission current density is significant. If the electrons from a

small area of metal (1) are allowed to incident the surface of metal (2) and if this impinging electron beam represents the only electronic interaction between the two metal surfaces, then equation 3.19 becomes

$$e\chi_1 - e\chi_2 + eE_T = V_{12} \qquad 3.24$$

where eE_T represents the thermoelectric e.m.f. The thermoelectric e.m.f. can be expressed as[23]

$$eE_T = \int_T^{T_1} \frac{d\,\bar{u}_1}{dT} + \int_{T_1}^{T_2} \frac{d\,\bar{u}_2}{dT} + \int_{T_2}^{T} \frac{d\,\bar{u}_2}{dT} \qquad 3.25$$

and T represents the temperature of the voltage supply. Since metal (2) is not actually in direct contact with metal (1) and assuming that the energy dissipated at surface of metal (2) by the electron beam is trivial, then the second term in equation 3.25 will be effectively zero. It was also assumed that the temperature of metal (2) was constant and thus the third term can also be neglected. Equation 3.25 is then reduced to

$$eE_T = \int_T^{T_1} \frac{d\,\bar{u}_1}{dT} \qquad 3.26$$

An ideal current-voltage characteristic for the electron beam striking the metal surface (2) is illustrated by Fig. 6. In Fig. 6,

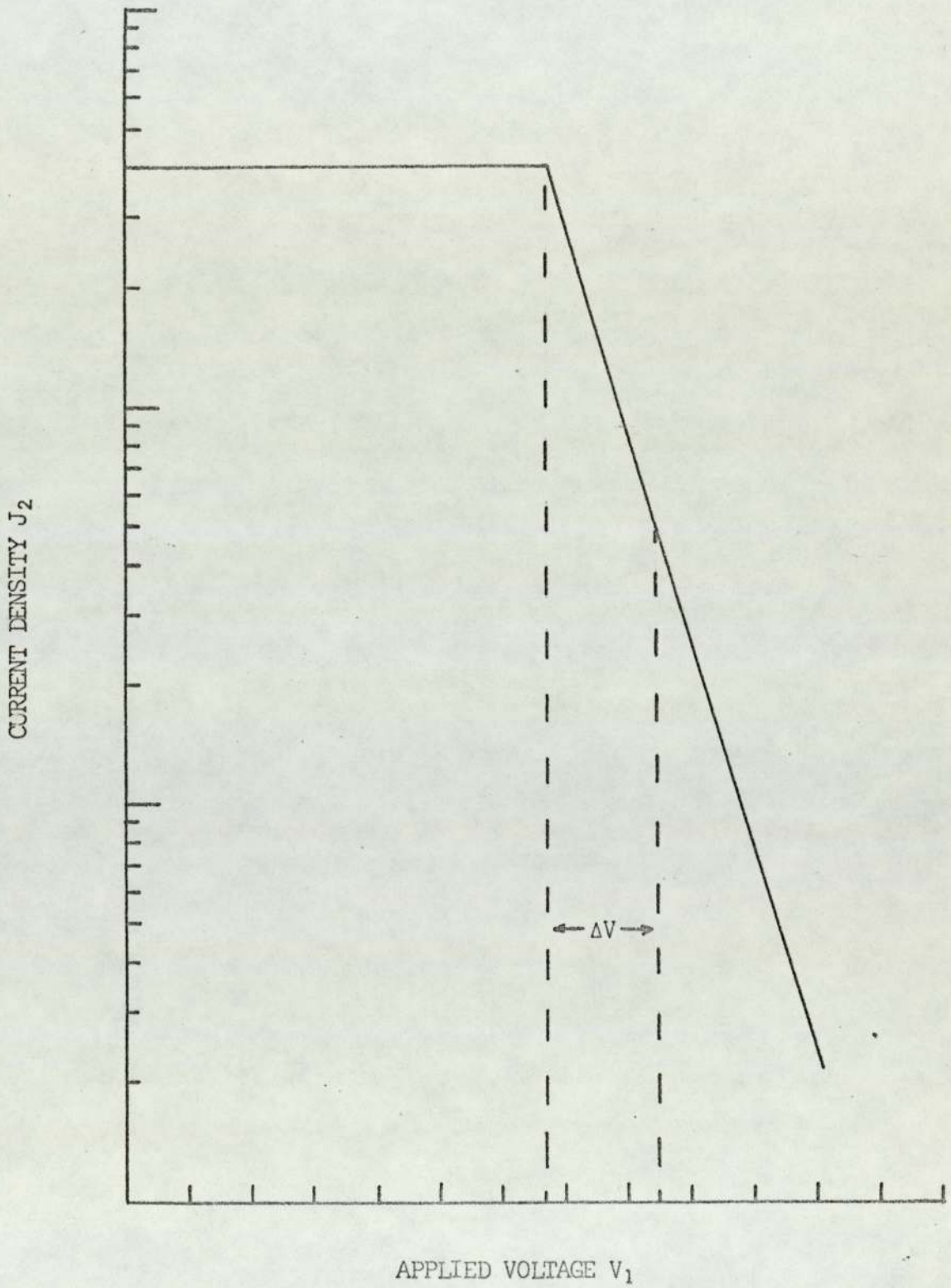

Fig. 6. Current J_2 as a function of applied voltage V_1.

J_2 represents the electron current density impinging the surface of metal (2), while V_1 represents the voltage applied to metal (1) with respect to metal (2).

Examination of Fig. 6 reveals that the current-voltage characteristic is comprised of three distinct regions. Region A is known as the saturated current region. It is apparent from Fig. 6 that the current density J_2 in this region is independent of the applied voltage V_1, but it is found to be dependent on the electron transmission coefficient, the electron work function and the temperature of the surface of metal (1). The current density J_2 can now be expressed by equation 3.7 provided r_e, T, and $e\chi$ are replaced by r_{e_1}, T_1, and $e\chi_1$, respectively.

In order to explain the independence of the current density J_2 on the applied voltage V_1 in the saturated region, consider the electrostatic potential energies of the electrons in the vacuum just outside of the metal surfaces. If the electrochemical potential energies are equal, then the relationship of the electrostatic potential energies of the electrons is given as:

$$e\phi_{a_1} + V_{12} = e\phi_{a_2} \qquad 3.27$$

If a voltage V_1 is applied to metal (1), with respect to metal (2), then the electrochemical potentials of the metals will not be equivalent and equation 3.27 will become

$$e\phi_{a_1} + V_{12} + V_1 > e\phi_{a_2} \qquad 3.28$$

and will be valid for all values of $V_1 > -V_{12}$.

The above electrostatic inequality is illustrated by Fig. 7. From Fig. 7 it is apparent that the electrons emitted from the metal surface (1) do not have to surmount an electrostatic potential barrier in order to approach the surface of metal (2). J_2 will then be dependent only on the emission parameters of the surface of metal (1).

The point B in the characteristic current-voltage plate is generally referred to as the "knee". The "knee" occurs when the electrostatic potentials energies of the electrons in the vacuum just outside the metal surfaces are equal and so the inequality 3.28 becomes

$$e\phi_{a_1} = e\phi_{a_2} \qquad 3.29$$

when

$$V_1 = -V_{12} \qquad 3.30$$

Now equation 3.19 can be rearranged as

$$e\chi_1 = e\chi_2 + V_{12} \qquad 3.31$$

and if $e\chi_1$ is temperature dependent then equation 3.31 becomes

$$e\chi_1(T) = e\chi_2 + V_{12}(T) \qquad 3.32$$

Since the contact potential difference can be determined from equation 3.30, when equation 3.29 is applicable, then the current density J_2 can now be expressed in terms of $e\chi_2$ and $V_{12}(T)$ as

$$J_2 = A(1 - r_{e_1})\, T_1^2 \exp - \left[(e\chi_2 + V_{12}(T))/kT_1 \right] \qquad 3.33$$

If equation 3.33 is rearranged into a logrithmic form, then upon differentiation with respect to (1/T) we obtain

$$e\chi_2 = -k \frac{d\left[\ln(J_2/T_1^2) - V_{12}(T) \right]}{d\,(1/T)} \qquad 3.34$$

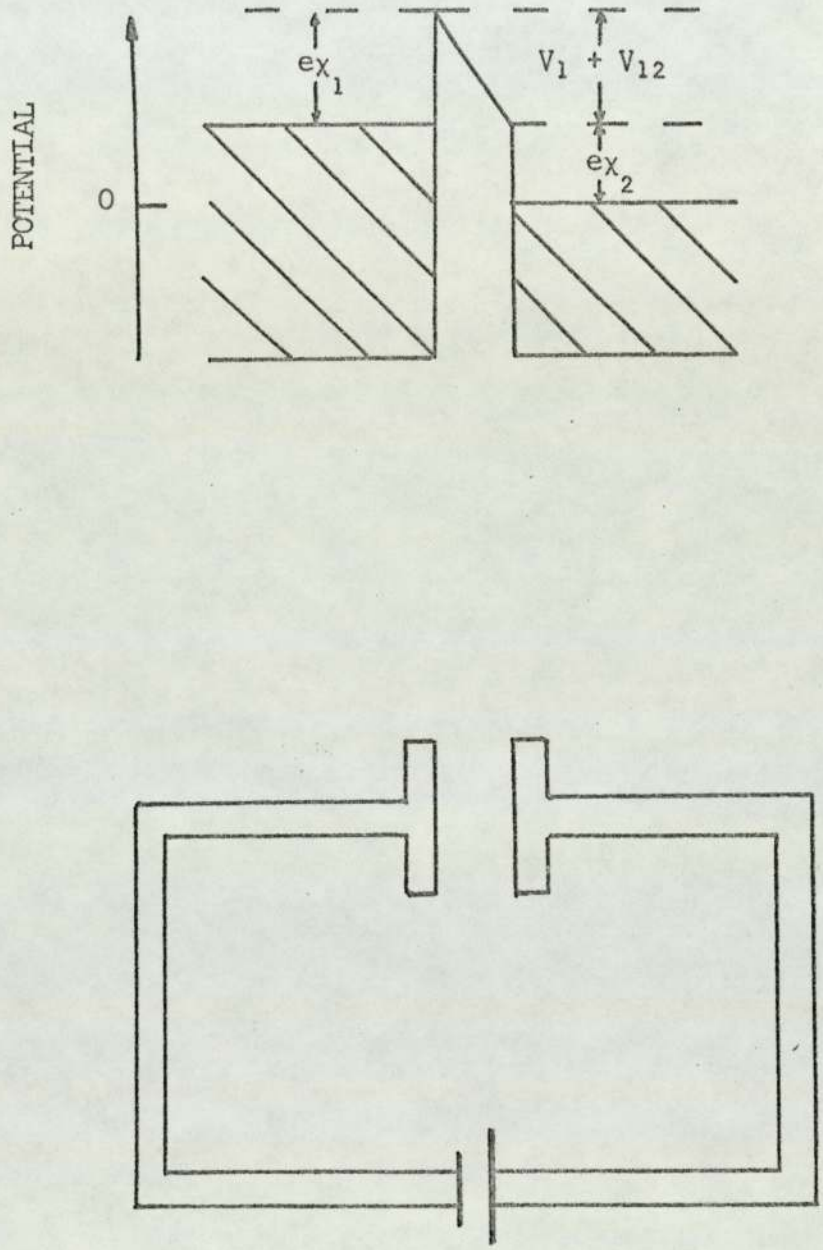

Fig. 7. Potential difference in saturated region of the characteristic plot.

Hence from equation 3.33, the work function of a surface at a constant temperature can be determined from a Richardson type plot of the saturated current densities and contact potential differences obtained from a family of characteristic plots. The family of characteristic plots is obtained by varying the temperature of the surface of metal (1).

Region C is known as the retarding region of the characteristic plot. In this region the electrostatic potential energies of the electrons just outside the surface of metal (2) are greater than those outside metal (1) and this case is illustrated by Fig. 8.

Now the inequality 3.28 will become

$$e\phi_{a_1} + V_{12} + V_1 < e\phi_{a_2} \qquad 3.35$$

when $-V_{12} > V_1$.

V_1 can also be expressed as

$$V_1(T) = -V_{12}(T) - \Delta V \qquad 3.36$$

where ΔV is the displacement voltage in the retarding portion of the characteristic plot as shown in Fig. 6.

Then upon substituting equation 3.36 into equation 3.33, the current density J_2 can now be expressed as

$$J_2 = A(1 - r_{e_1}) \times T_1^2 \times \exp - ((e\chi_2 - V_1(T) - \Delta V)/kT_1) \qquad 3.37$$

where V_1 is the applied voltage of a displacement voltage of ΔV and can have values of $0 \leq V_1 \leq 0$. Now if equation 3.37 is rearranged into a logrithmic form which is then differentiated with respect to

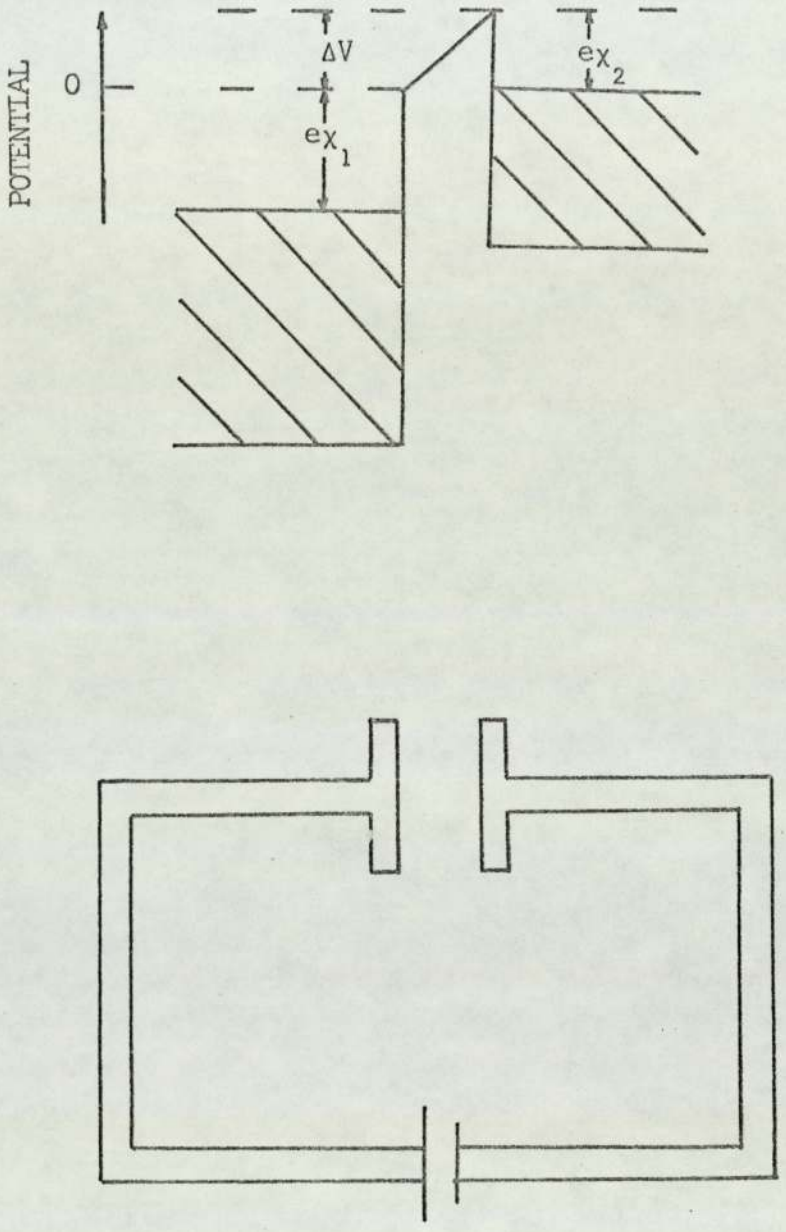

Fig. 8. Potential difference in the retarding region of the characteristic plot.

(1/T), the $e\chi_2$ can be expressed as

$$e\chi_2 = -k \frac{d\left[\ln(J_2/T_1^2) + V_1(T)\right]}{d\,(1/T_1)} + \Delta V \qquad 3.38$$

In order to solve equation 3.38, a Richardson type plot is made from the current densities J_2 and the applied voltages V_1 obtained, at the same displacement voltage, from a family of characteristic plots. Fig. 9 illustrates the manner in which the current densities J_2 and the applied voltage V_1 are obtained from the family of characteristic plots.

The term $A(1 - r_{e_1})$ appears in both equations 3.33 and 3.37 and can be evaluated by determining either $\left[\ln(J_2/T_1^2) + V_1(T)\right]$ or $\left[\ln(J_2(\text{sat.})/T_1^2) + V_{12}(T)\right]$ as $T_1 \to \infty$. When $J_2(\text{sat.})$ refers to the saturated current density.

From the above discussion it appears that the electron beam method for measuring the contact potential difference is quite useful for determining the electron work function of a surface held at a constant temperature. The temperature is, however, limited to about 1000 K because at higher temperatures the thermionic emission current would become significant.

3.3.4.3. Use of the contact potential difference method in the study of gas-metal surface interactions

The capacitor method is quite useful in studying the effects of a gas-metal surface interaction. Its usefulness stems from the fact that the measurement technique does not interfere with the gas-surface reaction, but only measures the results of the interaction in terms of the change in the work function of the surface. The Kelvin method has been quite successful in studying the effects of carbon monoxide[47],

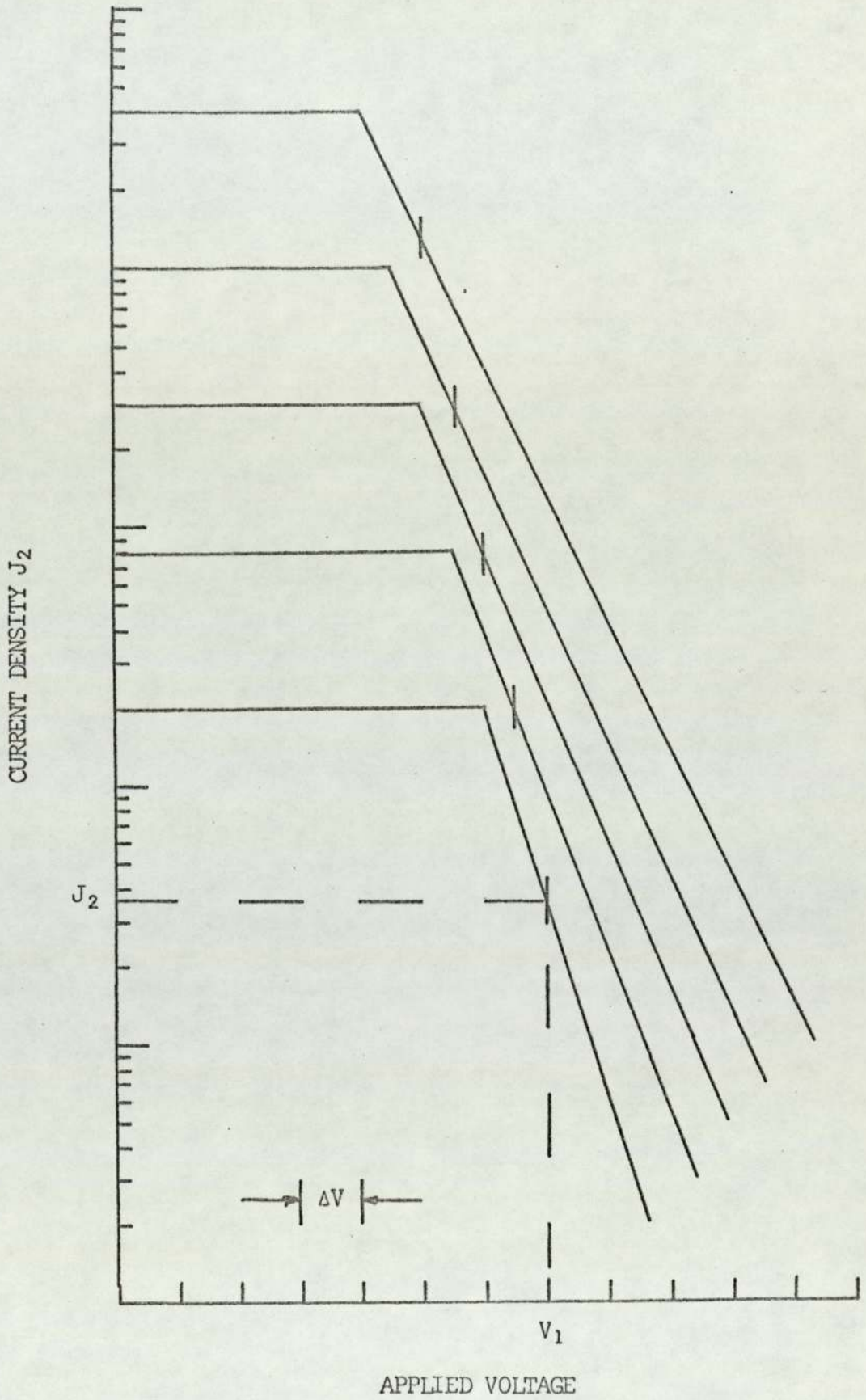

Fig. 9. Family of current-voltage characteristic plots.

halogens[46], nitrogen[47], oxygen[47], and potassium[48] on metal surfaces. Whereas, the electron beam method has been used to study the interactions of oxygen[49-50], hydrogen[49], carbon dioxide[49], nitrogen[49], cesium[51], sodium[26], and potassium[26] on metal surfaces.

3.4. Work Function Measurements on Patchy Surfaces

The discussion thus far has been concentrated on the work function of a homogeneous surface. There are, however, a large number of surfaces that are comprised of areas or patches which have different work function values. These patches arise from differences in the crystalline structure of the metal surface or the formation of islands of adsorbed gases. In the following discussion it will be assumed that the shortest distance across a patch will greatly exceed the distance between the surface and the point defined by the electrostatic energy.

By using equation 3.1, the electrostatic potential energy adjacent to the ith patch is defined as

$$e\phi_{ai} = -e\chi_i - \bar{u} \quad . \tag{3.39}$$

The electrostatic potential for n patches defining a unit area will be given as

$$\sum_{i=1}^{n} f_i \, e\phi_{ai} = -\sum_{i=1}^{n} f_i \, e\chi_i - \bar{u} \tag{3.40}$$

when f_i is that fraction of area covered by the ith patch. If we let

$$\sum_{i=1}^{n} f_i \phi_{ai} = e\bar{\phi}_{ai} \qquad 3.41$$

and

$$\sum_{i=1}^{n} f_i \, e\chi_i = e\bar{\chi} \qquad 3.42$$

the equation 3.40 becomes

$$e\bar{\phi}_a = -e\bar{\chi} - \bar{u} \; . \qquad 3.43$$

From equation 3.43, equation 3.19 can now be rewritten in terms of a patchy surface as

$$e\bar{\chi}_1 - e\bar{\chi}_2 = e\bar{\phi}_{a_2} - e\bar{\phi}_{a_1} = \bar{V}_{12} \qquad 3.44$$

where $\bar{V}_{12}$ represents the average contact potential.

Consider now the effect that a patchy surface will have on the "knee" portion of characteristic plot as described in section 3.3.4.2. Since the electrostatic potential energies of the two surfaces are equal, equation 3.30 will become

$$V_1 = -\bar{V}_{12} \qquad 3.45$$

for patchy surfaces. Equation 3.45 is particularly important because it predicts that for patchy surfaces the contact potential difference will be an averaged value and hence the "knee" will not be as well defined as that illustrated in Fig. 6.

The work function of the surface of metal (2) now is expressed as

$$e\bar{\chi}_2 = k \frac{d\left[\ln(J_2/T_1^2) - \bar{V}_{12}(T) \right]}{d\,(1/T_1)} \qquad 3.46$$

and can be solved from a Richardson plot of the current density (saturated) and average contact potential differences obtained from a family of characteristic plots.

CHAPTER 4

EXPERIMENTAL APPARATUS

4.1. Introduction

The primary objective of this thesis is to elucidate the gas-metal surface interaction by studying the kinetics of the gas desorption reaction and the effect of adsorbed gas species on the work function of a tantalum surface. Such an objective will require an experimental apparatus that must fit the needs of each area of study, and thus the instrument must possess both simplicity in its design and flexibility in its operation.

Fig. 10 is a general description of the experimental equipment. From an examination of Fig. 10, it can be seen that the experimental apparatus is comprised of a vacuum system, a reaction cell, and a gas supply system.

4.2. Vacuum System

4.2.1. General description

The sorption pumps and the gas supply system were constructed from pyrex glass. The ultra-high vacuum portion of the system, except for the pyrex housing used for the experimental cell, was constructed out of stainless steel components supplied by Vacuum Generators Limited. These stainless steel parts, i.e., the all metal values, the symmetrical 6-way adaptors, the reducer coupling, the sublimation pump housing, and the various flanges were all bakable to a temperature of 400^{o}C. Gold metal seals were used throughout this portion of the vacuum system except for the flange supporting the current leads and filaments of the titanium sublimation pump.

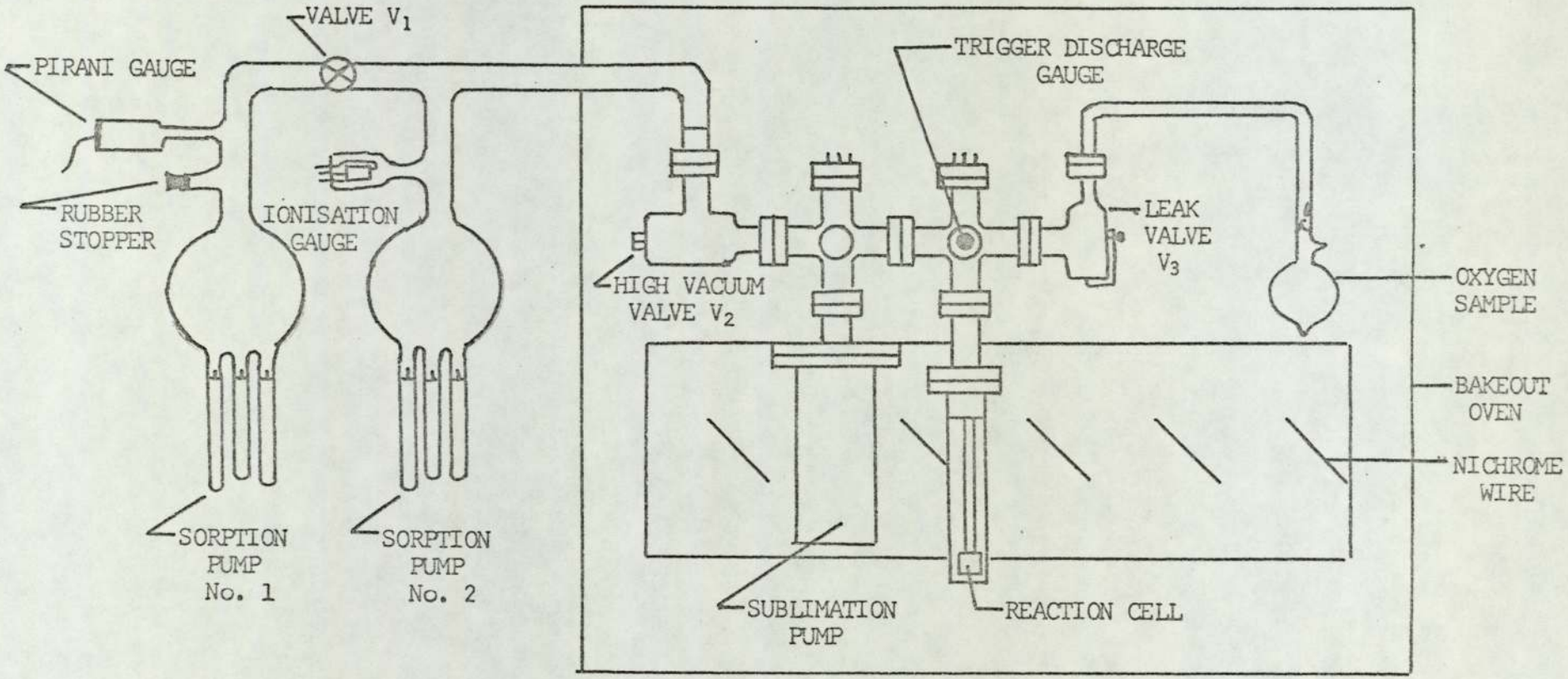

Fig. 10. Experimental equipment.

The ultra-high vacuum gauge was a trigger discharge gauge, model No. V315, supplied by GEC - AEI (Electronics) Ltd. The gauge and its magnet were bakable to 300°C.

The entire ultra-high vacuum portion of the system and the gas supply system, as shown in Fig. 10, were mounted in an asbestos bake-out oven. This bakeout oven was heated by nichrome heating elements and was capable of reaching temperatures of 250°C. The sorption pumps were mounted on the outside of the oven, and thus the entire system was quite mobile.

The next three sections will be concerned with the description of the various pumping modes used in the system. The last section concerning the vacuum system will be devoted to the description of the pump down procedure.

4.2.2. Sorption pumps

In Chapter 2 it was shown that presence of hydrocarbon vapours in a vacuum system could represent a serious source of contamination for gas-metal surface desorption reactions. It was also shown that sorption[52] and sublimation pumps[53] were free of such sources of contamination, and hence these pumps were chosen as roughing and high vacuum pumps respectively.

The two sorption pumps, as illustrated by Fig. 10, were constructed in a manner similar to that reported by J. O. Cope[54]. The pumps were connected in series and were isolated from one another by means of a valve V_1 with an elastomer gasket. Each of the pumps contained five pumping chambers. These pumping chambers were fabricated from pyrex tubing of a medium wall thickness and an outside diameter of 2.5 cm. A tube of stainless steel wire mesh, was held in the centre of each of the chambers by means of stainless steel wires attached to the tube

and pressing against the walls of the chamber. The zeolite pellets (10 X) were placed in the space between the walls of the chamber and the stainless steel tubing. It was found that about 100 grams of the zeolite pellets were sufficient to fill each pumping chamber to a height of about 8½ inches. The main function of the stainless steel tubing was to ensure that the gas could reach all parts of the pumping chamber[55]. The thickness of the zeolite layer in the pump chamber was about three or four times pellet diameter. A thin zeolite layer is desirable because it improves the heat transfer and thus also improves the performance of the pump[55].

The volume of the pump chamber in pump No. 1 was about three litres. The pressure in this pump was measured by a Pirani type vacuum gauge. In order to prevent a dangerous pressure build up during the regeneration cycle[55], this pump was equiped with a B-14 socket and a rubber stopper to act as a safety pressure relief valve.

Pump No. 2 had a pump chamber volume of two litres. The pressure in this pump was measured by a hot filament ionisation gauge supplied by Genevac Ltd.

The vacuum pressure obtainable by a system pumped by a sorption pump will be dependent upon the composition of the gases in the system and the gases adsorbed on the zeolite. Zeolite surfaces at 77 K will adsorbe gases such as oxygen, nitrogen, and water vapour, while gases like neon, helium, argon, and hydrogen are not readily adsorbed. Some gases, such as water vapour, are so strongly adsorbed on the zeolite that they can only be removed by baking the zeolite at a temperature of about 280°C. In order to obtain the lowest possible pressure, the sorption pump must be activated by purging with boiled-off nitrogen while the pump chambers are baked at a temperature of 280°C.

When a pump was not activated before the pump was placed into operation, i.e., the pump chambers were immersed in liquid nitrogen so that the zeolite was below the surface of liquid, the lowest pressure obtainable was about 1×10^{-3} torr. For an activated pump, however, a pressure of 5×10^{-6} torr could be obtained. The pressure as a function of time for the activated sorption pump No. 1 and for an activated sorption pump reported by J. O. Cope[54] are illustrated in Fig. 11.

In order to obtain pressures lower than 5×10^{-6} torr, the sorption pumps No. 1 and No. 2 were operated in series. The following is a typical series of steps taken to activate the sorption pump No. 2 by means of pump No. 1.

1. The isolating valve V_1 was opened.
2. The pump chambers of pump No. 2 were placed in an electric bakeout oven and the temperature increased to about 280°C.
3. The sorption pump No. 1 was put into operation and the pressure of the entire system reduced to its lowest value.
4. Valve V_1 was closed and pump No. 1 was allowed to regenerate, i.e., the pump chambers were permitted to warm to room temperature.
5. The sorption pump No. 1 was then purged with boiled-off nitrogen and towards the end of this purge the nitrogen pressure in pump No. 2 was increased to one atmosphere by momentarily opening valve V_1.
6. With the valve V_1 closed, the sorption pump No. 1 was again put into operation.
7. When the pressure in pump No. 1 was about 1×10^{-3} torr, the pressure in pump No. 2 was slowly reduced to about 1 torr by periodically slightly opening the valve V_1.

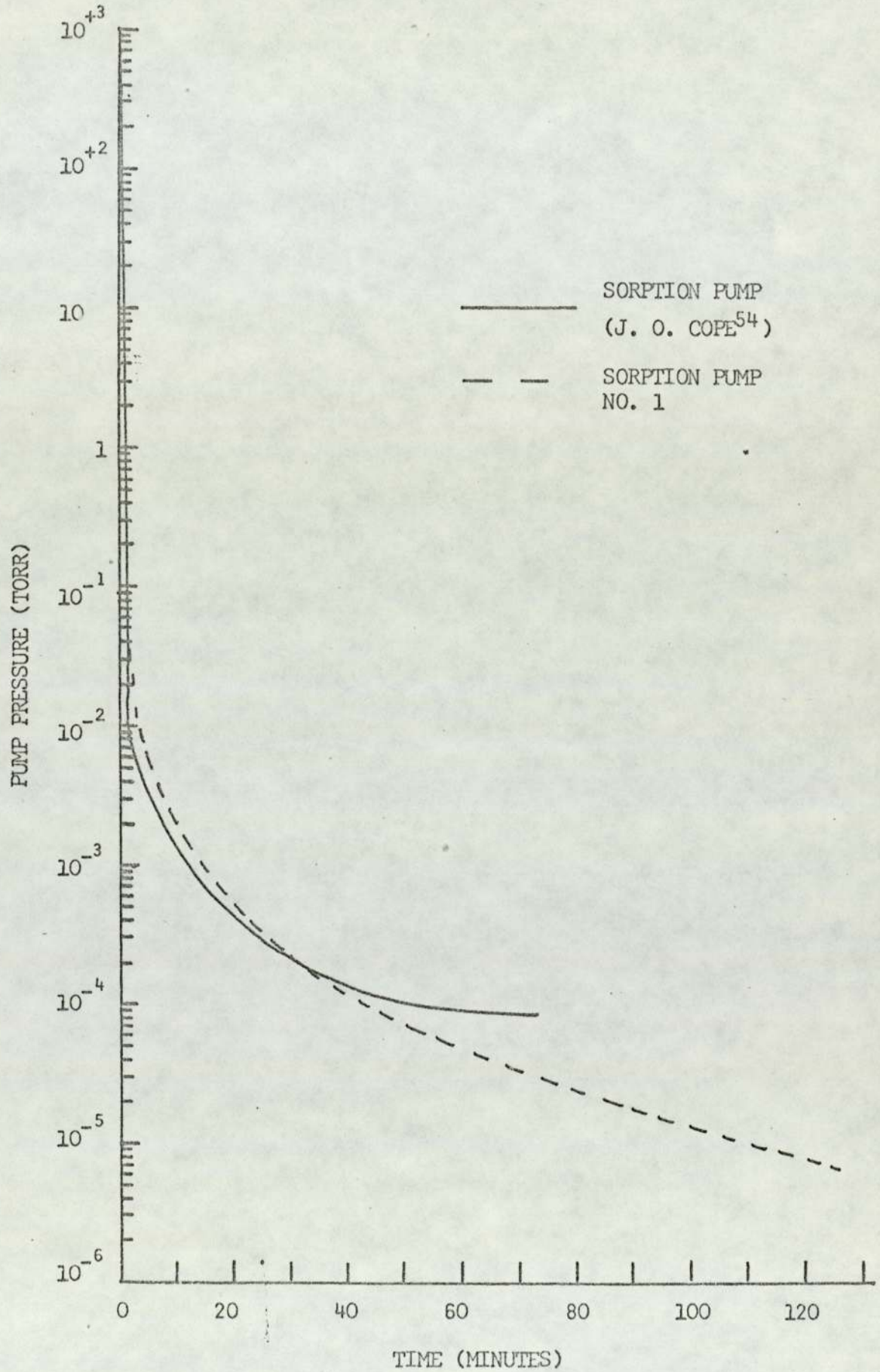

Fig. 11. Sorption pump pressure as a function of time.

8. Steps 5, 6, and 7 were repeated at least four times.
9. With the pressure in pump No. 2 at about 1 torr, the pump chambers of pump No. 2 were now removed from the bakeout oven.
10. The sorption pump No. 2 could be placed into operation as soon as the pump chambers had reached ambient room temperature.

Upon completion of the above procedure, pressures of 5×10^{-7} torr were obtainable in pump No. 2. Care was taken in step 7 that the gas flow from pump No. 2 to pump No. 1 was always in the viscous flow region and this limited the back diffusion of water vapour and the non-adsorbable gases into pump No. 2.

4.2.3. Sublimation pump

The titanium sublimation pump was used to obtain system pressures of less than 1×10^{-7} torr. The stainless steel chamber, the titanium (85%)-molybdenium (15%) filaments and their copper electrical support rods were supplied by Vacuum Generators Limited. A cutaway of this pump is shown in Fig. 12.

The operation of this pump is quite simple. The outer surface of the stainless steel pump chamber was immersed in liquid nitrogen. A clean titanium film was then deposited on the walls of the pump chamber by resistance heating of one of the filaments. The high heating current necessary for a sufficient titanium deposition rate was obtained from two 12 volt heavy duty storage batteries that were connected in parallel. The time of a typical titanium deposition was about $1\frac{1}{2}$ minutes.

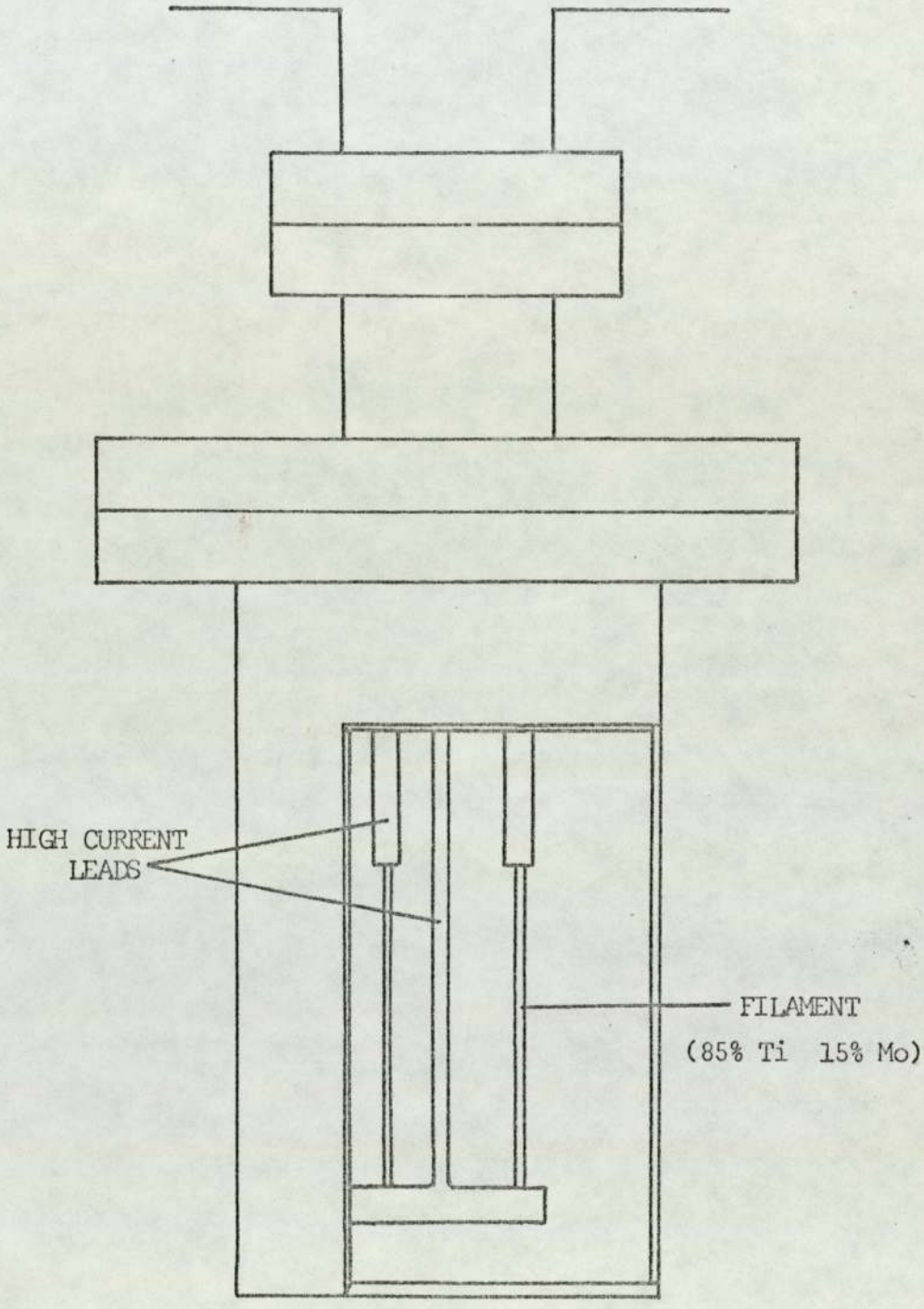

Fig. 12. Cutaway of sublimation pump.

As stated in Chapter 2, the pumping speed for a given partial pressure will be dependent on the rate of adsorption of the gas species on the clean titanium surface. The pumping speed per unit area for gases such as hydrogen, nitrogen, oxygen, and water vapour are quite sufficient. For example, the pumping speed of nitrogen on a clean titanium surface at 77 K will be 2.6 litres/sec/cm^2 when the nitrogen pressure is about 1×10^{-8} torr. The pumping speed of the sublimation pump for gases such as helium, neon, and argon is quite low. Therefore, as in the case of the sorption pumps, steps must be taken to purge these gases from the system prior to the operation of the sublimation pump.

4.2.4. Trigger discharge gauge

As stated previously, a Penning discharge pressure gauge was selected for the ultra-high vacuum portion of the system. This form of gauge can measure pressures in the 10^{-13} torr range and does not suffer from an X-ray or filament vapour pressure limitation. This gauge has the additional advantage that its construction is quite robust and alterations in gauge geometry because of sagging filaments or grids cannot occur.

Since the ion getter pump is based on the principle of a Penning gauge, it is not surprising that the pumping speed of the discharge gauge is significantly greater than that of the Bayard-Alpert type gauge. Discharge gauge pumping speeds of 1 litres/sec are generally reported, but pumping speeds as high as 3 litres/sec for oxygen has been reported for a Redhead type gauge[56]. Hence this form of gauge can, at pressures less than 10^{-8} torr, represent a large portion of the total pumping speed.

4.2.5. Vacuum pump-down procedure

This section will be a general description of the pump-down procedure that was used to evacuate the experimental apparatus to high vacuum pressures.

1. Vacuum valves, V_1, V_2, and V_3 were opened fully.
2. The conditioning steps 2 through 10 inclusive for pump No. 2, as described in section 4.2.2., were repeated.
3. The doors of the oven were placed in position and the heat radiation shields were placed over the entire oven.
4. The temperature, measured by a mercury thermometer, in the oven was slowly increased at a rate that did not exceed 100°C per hour. The oven temperature was limited to 250°C and maintained at this temperature for a period of not less than 4 hours.
5. Each of the titanium filaments were outgassed for 30 minutes by a heating current of 20 amperes.
6. The oven temperature was allowed to cool to ambient room temperature at a rate not faster than 100°C per hour.
7. The high vacuum valve V_2 was closed and the sorption pump No. 2 was allowed to regenerate.
8. The steps to activate pump No. 2, as described in section 4.2.2., were again repeated.
9. The high vacuum valve V_2 was opened and the system pressure was reduced to about 1×10^{-6} torr.
10. The vacuum valves V_2 and V_3 were then closed and the discharge gauge was turned on.

11. When the pressure did not decrease any further, as a result of the pumping by the discharge gauge, the titanium sublimation pump was placed into operation.

As a result of the above procedure, the pressure in the ultra-high vacuum portion of the system could be reduced to pressures well into the 10^{-11} torr range. The reason for the activating pump No. 2, after the bakeout cycle, was that the pressure in the system was of a value of about 1×10^{-4} torr. This pressure increase was not the result of a leak in the system, but was due to the saturation of pump No. 2 with hydrogen. This increase in the partial pressure of hydrogen is believed to be a result of the degassing of the stainless steel during the bakeout cycle[57]. The hydrogen was partially removed by the operation of the activated sorption pump No. 2, and further removed by operating the sublimation pump.

4.3. The Reaction Cell

The reaction cell was designed to study the effects that adsorbed gas species have on the work function of a metal surface and the thermal desorption reaction of gases from a surface. The various experimental techniques required to conduct the latter studies were viewed in some detail in Chapters 2 and 3. Because of the number of various techniques that could be employed, it becomes of the utmost importance that the methods which are used are compatible.

The first experimental technique that was considered was that of the electron work function of a plane metallic surface. From the discussion in Chapter 3, it appears that either the photoelectric or the contact potential method would be suitable. The use of the photo-electric method requires an involved optical system because the light

beam impinging the surface must vary with frequency but no intensity. The contact potential difference method of determining the work function is experimentally less complicated than that of the photoelectric method.

The electron beam method was used to determine the contact potential difference. The experimental apparatus used was similar to that reported by H. Shelton[45]. The planar triode used by H. Shelton is illustrated by Fig. 13. The 3000 gauss magnetic field was placed so that the magnetic and electric fields were normal to the surface of the metal filaments. A positive potential, with respect to the filaments, was applied to the shields and the grid containing the aperture. As a result of electrostatic and magnetic field geometry, the only electrons that were measured by the collector were those formed by a beam whose area was defined by dimensions of the aperture. The characteristic plot was obtained by varying the potential of the collector with respect to the emitter.

The experimental cell used in this study of gas surface interactions is illustrated by Fig. 14. The upper and lower portions of the cell were constructed from a high purity copper sheet supplied by Imperial Metal Industries Ltd. The sides A and B were constructed from stainless steel wire mesh, so that the temperatures of the emitter and the collector could be measured by an optical pyrometer. The grid, emitter, and collector were fabricated from a .005 cm thick metallurgical grade tantalum sheet, which was supplied by the Fansteel Metallurgical Corporation.

Fig. 15 illustrates the electrical circuit that was used for the electron work function determination. The current for the emitter was supplied by two 12 volt heavy duty storage batteries that were connected in parallel. The potential of the emitter was varied by applying a voltage at the junction of the resistors shown in Fig. 15.

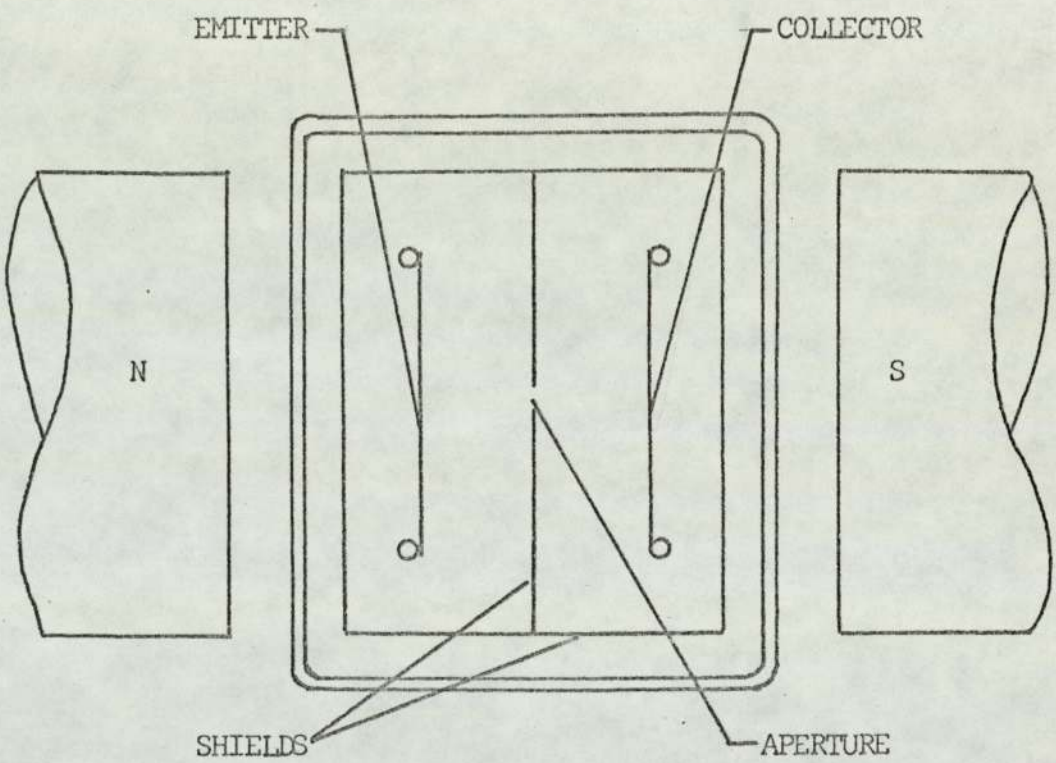

Fig. 13. Planar triode[45].

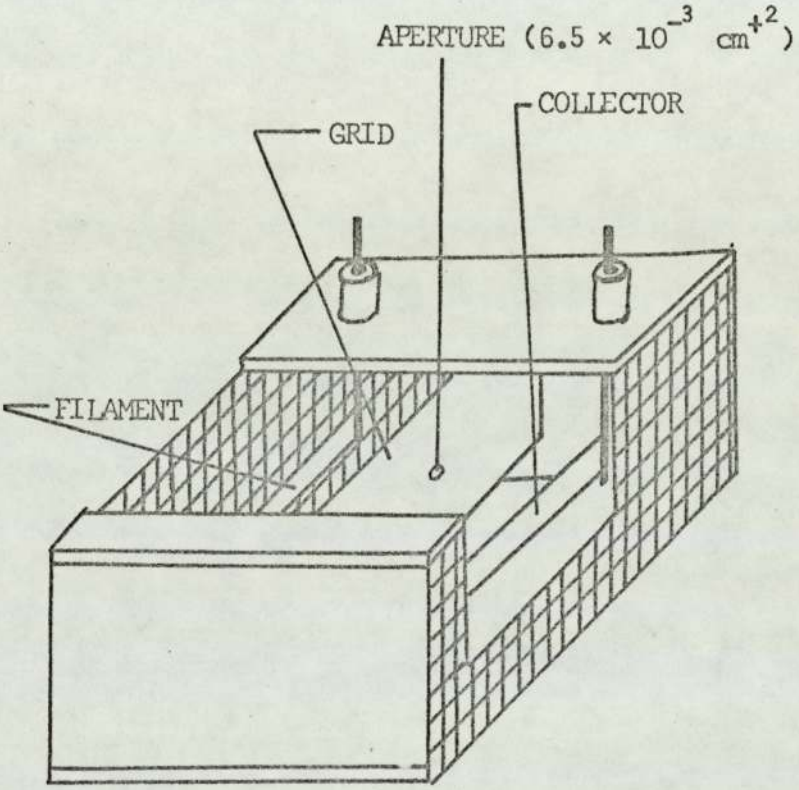

Fig. 14. Cutaway of experimental cell.

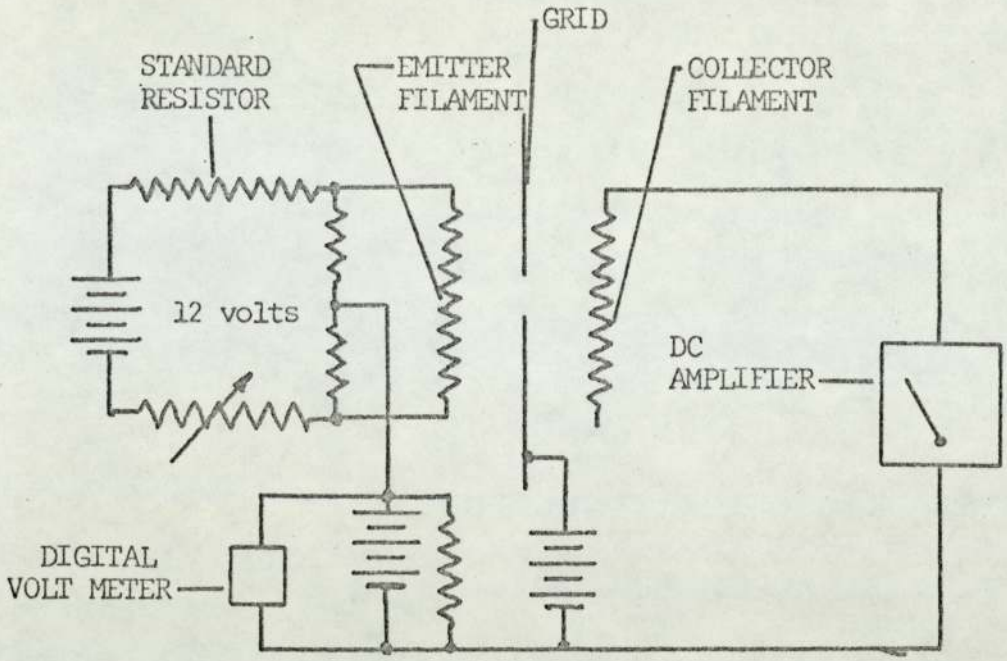

Fig. 15. Electrical circuit for work function determination.

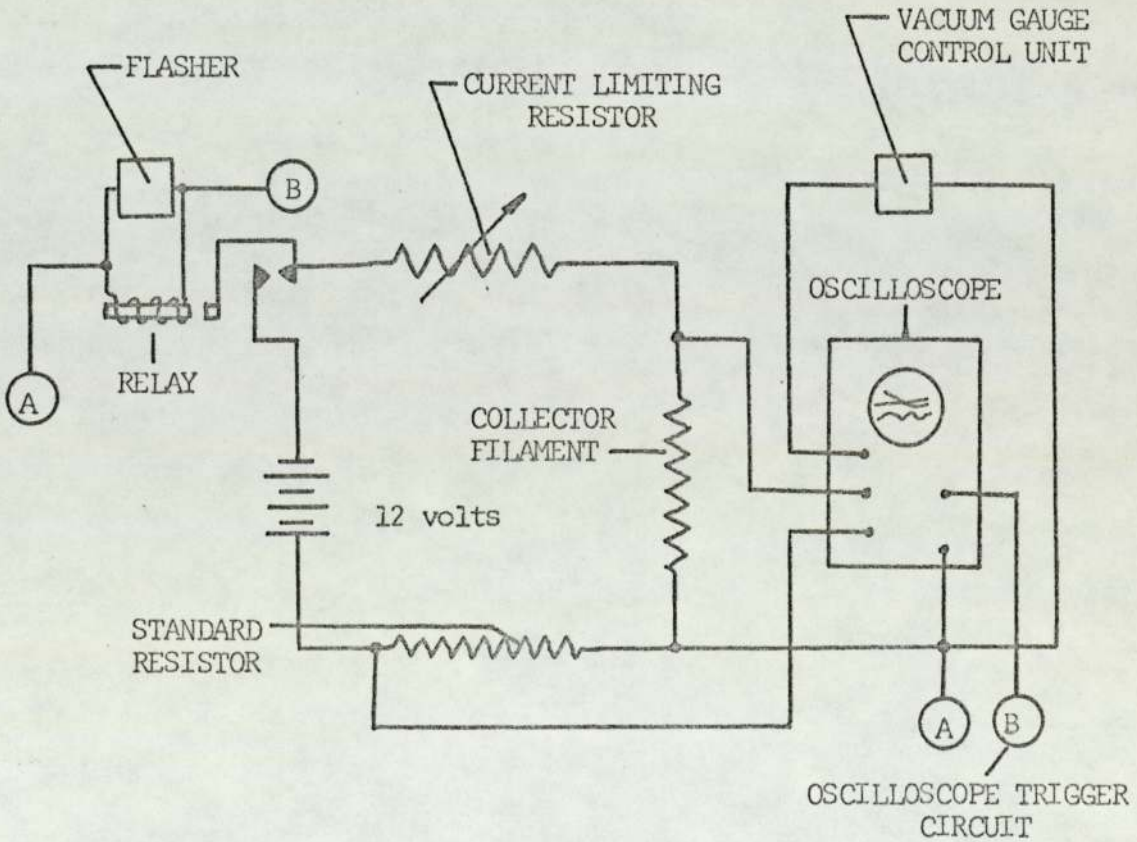

Fig. 16. Electrical circuit for thermal desorption studies.

In this cell, the collector filament will also serve as the "flash" filament for the thermal desorption studies. The length of the collector, which is limited by the dimensions of the cell, is not as long as one would desire for the use in thermal desorption reactions. A longer collector filament, however, could cause, because of sagging effects, serious alignment difficulties in the electron work function determination.

The electrical circuit used in the thermal desorption studies is illustrated by Fig. 16. The current was supplied by two 12 volt heavy duty storage batteries connected in parallel. The circuit current was determined by measuring the voltage occurs the standard resistor. The relay was controlled by a flashing unit supplied by Mr. M. Painter.

A Tektronic Oscilloscope type 545A with a type M_1 four trace pre-amplifier plug-in unit was used to display the following voltages along the same time base.

1. The voltage across the standard resistor.
2. The voltage across the collector filament.
3. The voltage output from the triggered discharge gauge.

The oscilloscope trace was recorded on photographic film.

4.4. Gas Supply System

As illustrated in Fig. 10, the gas sample was stored in a pyrex break-seal vessel. The manifold to the vessel was first evacuated by the pump down procedure outlined in section 4.2.5. When the pressure in the system was less than 1×10^{-6} torr, the leak valve V_3 was closed and the gas could be admitted to the manifold line by the crushing of the break-seal with a metal weight.

The gas used in this study was oxygen. The oxygen was prepared from the thermal decomposition of potassium permanganate. An AEI MS9 mass spectrometric analysis of the oxygen showed traces of both nitrogen and water vapour. Fig. 17 illustrates the experimental apparatus used to prepare the oxygen gas sample and the experimental procedure was as follows:

1. The ground glass valves V_4, V_5, V_6, and V_7 were opened.
2. The activated sorption pump No. 1 was placed into operation and the pressure in the line, measured by a Pirani vacuum type gauge, was reduced to less than 1×10^{-3} torr.
3. Heat was applied to the $KMnO_4$ and the pressure was allowed to increase to greater than 1 torr.
4. The vacuum valve V_7 was opened periodically until the pressure in the line was about .2 torr.
5. Steps 3 and 4 were repeated 18 times.
6. Valves V_4, V_5, V_6, and V_7 were closed and the gas sample flask was sealed at points P_1 and P_2.

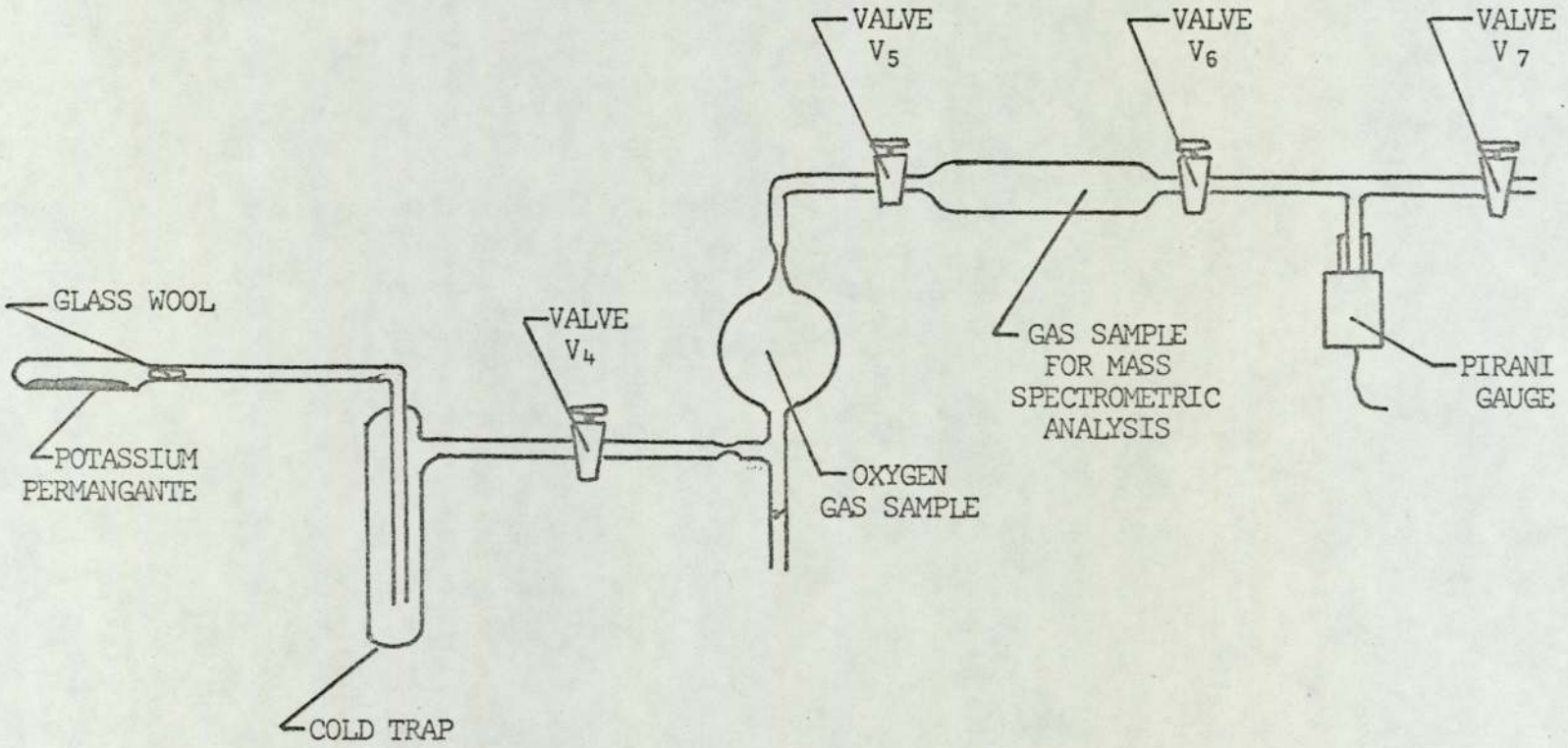

Fig. 17. Apparatus used to prepare oxygen gas sample.

CHAPTER 5

RESULTS AND DISCUSSION OF THE THERMAL DESORPTION REACTIONS

5.1. Introduction

This chapter will be concerned with the studies of thermal desorption from a tantalum surface. Section 5.2. will consider the interpretation of the oscilloscope display traces and the experimental procedure used for a thermal desorption reaction. Particular attention will be given to the determination of the filament temperature as a function of time.

Sections 5.3. and 5.4. will consider the interpretation of the experimental data. In these sections the experimental data obtained from typical β_1 and β_2 peaks will be examined.

Sections 5.5. and 5.6. will examine the effects that the residual gases and oxygen have on the thermal desorption spectrum.

5.2. The Oscilloscope Display of a Thermal Desorption Reaction

Figure 18 illustrates an oscilloscope display of a thermal desorption reaction (experiment No. 236-1) which was recorded on 35 mm Ilford 50-91 recording film. The time base of this display was .2 sec cm^{-1}. The time intervals between .00 and .18 seconds and between 1.82 and 2.00 seconds were not recorded because of a limitation in the field of view of the camera. The above is not a serious limitation and no desorption peaks were observed between .00 and .18 seconds when the zero of the time base on the display was shifted 1 cm to the right.

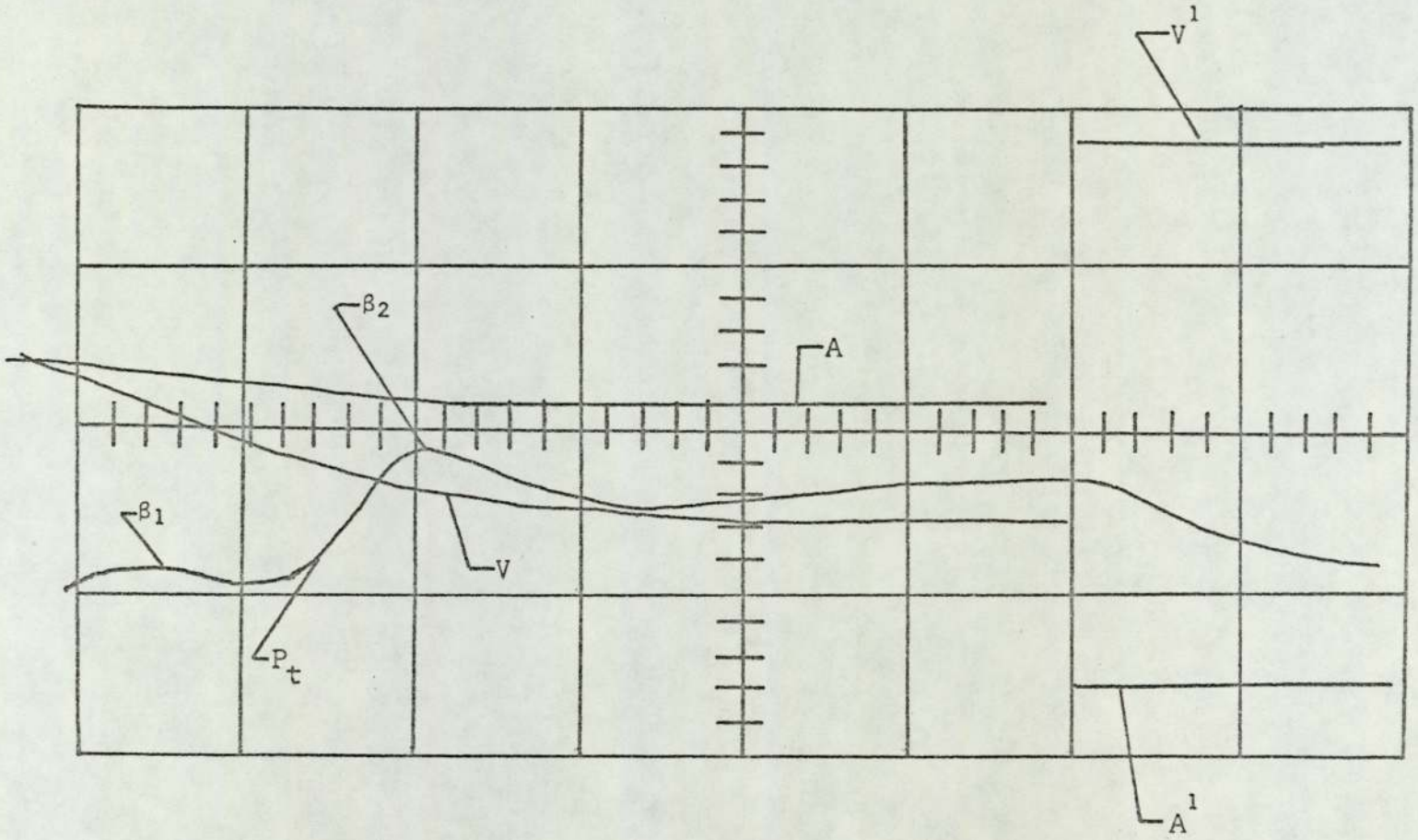

Fig. 18. An oscilloscope display of a thermal desorption reaction.

The voltage across the standard resistor is represented as a function of time by the trace designated as A. The vertical scale of this trace was .05 volts cm^{-1}. This voltage is directly proportional to the collector current and hence trace A also represents the collector current as a function of time. The trace designated by A' indicates the zero voltage base line for the trace A.

The trace V is a display of the collector voltage as a function of time. The vertical scale for this trace and 1 volt cm^{-1}. The trace V' represents the zero base line for the V trace.

The pressure trace is designated by P_t and represents the pressure measured by the discharge gauge as a function of time. The discharge gauge was calibrated for dry air for which the gauge sensitivity is 2.5 amperes $torr^{-1}$. It can be assumed that the pressure increase is due to an increase in the partial pressure of oxygen. If the latter assumption is true, then the gauge reading must be corrected for the gauge sensitivity for oxygen. The value of the gauge sensitivity for oxygen was not supplied by the manufacturer. The manufacturer does state that the gauge sensitivities for nitrogen and dry air are equivalent, and thus one can also assume that the gauge sensitivity for oxygen is approximately that for dry air.

The log scale range of the gauge control unit was selected and the amplification of the plug-in unit to the oscilloscope was adjusted, so that a vertical deflection of 1 cm on the display screen represented a pressure change of an order of magnitude.

The numerical values of the pressure, collector current, and collector voltage were obtained from an enlarged image of the display. The pressure values could be obtained directly from the P_t trace by enlarging the display such that 1 cm of the vertical spacing would just contain a cycle of a similogarithmic graph paper.

The collector current I_c was obtained from

$$I_c(t) = \frac{(Y - Y_o) \times S_F}{X \times R_s} \qquad 5.1$$

where $(Y - Y_o)$ represents the numerical difference between the trace at a time t and zero base line, X is the enlargement factor, R_s is the value of the standard resistor in ohms, and S_F is the vertical scaling factor in volts/cm^{-1}.

A similar expression

$$V_c(t) = \frac{(Y - Y_o) \times S_F}{X} \qquad 5.2$$

was used to determine the value of the collector voltage at a time t. Table I lists the measured values of P_t, I_c and V_c at various times during a thermal desorption reaction.

Examination of the P_t trace in Fig. 18 reveals that there are two distinct pressure peaks and are designated as β_1 and β_2. The pressure in the system should decrease to its initial pressure value after the β_2 peak, but there was only a slight pressure decrease followed by a gradual increase. The reason for this latter effect is believed to be because of the degassing from the walls of the cell.

5.2.1. Determination of the total pumping speed

As described in section 2.3, the pumping speed of the system was determined from the observed change in pressure as a function of time. Examination of Fig. 18 and Table I shows, that after 1.40 seconds or at the termination of the "flash", the pressure decreases with time.

Table I

Observed experimental values of the pressure, collector current, and collector voltage and the calculated values of the total collector resistance and temperature at various times during the thermal desorption reaction

Time (sec.)	Pressure (P_t) × 10^{+8} (torr.)	Collector Current (I_c) (amperes)	Collector voltage (V_c) (volts)	Collector Resistor (R_T) (ohms)	Collector temperature (K)
.20	1.4	13.0	1.54	.118	940
.28	1.6	12.5	1.71	.137	1285
.40	1.4	12.2	1.87	.153	1560
.49	2.0	12.0	2.00	.167	1805
.52	3.0	12.0	2.04	.171	1860
.55	4.0	12.0	2.12	.177	1980
.57	5.0	11.7	2.17	.186	2140
.62	9.0	11.7	2.20	.189	2200
.71	6.0	11.7	2.25	.193	2260

Table I (continued)

Time (sec.)	Pressure (P_t) × 10^{+8} (torr.)	Collector Current (I_c) (amperes)	Collector voltage (V_c) (volts)	Collector Resistor (R_T) (ohms)	Collector temperature (K)
.77	5.0	11.7	2.29	.197	2320
.91	4.0	11.7	2.34	.200	2320
1.00	5.0	11.7	2.34	.200	2320
1.20	6.0	11.7	2.34	.200	2320
1.40	7.0	11.7	2.34	.200	2320
1.46	5.0				
1.50	4.0				
1.57	3.0				
1.76	2.0				

From the observed pressure values at various times, the pumping speed of the system was found to be 15.3 litres sec^{-1}.

5.2.2. Collector temperatures as a function of time

The temperature of the collector as a function of time, as discussed in section 2.5.1., can be determined from the instantaneous filament resistance R_T. This resistance value at a time t is obtained from the ratio of the instantaneous collector filament voltage V_c and the collector current I_c. R_T can be defined as

$$R_T = R_{Ta} + R_{Cu} + R_{ss} + R_x \qquad 5.3$$

where R_{Ta} is the resistance of the tantalum collector filament, R_{Cu} and R_{ss} are the resistances of the copper leads and stainless steel filament supports respectively, and R_x is the sum of all the other resistances. Table I lists calculated values of R_T at various times during the thermal desorption reaction. A plot of R_T as a function of time is shown in Fig. 19. Fig. 19 shows, for portion of the curve between the times .20 and .60 seconds, that R_T appears to be linearly dependent on time. From this linear relationship of R_T with time, the initial resistance R_T^o can be obtained by extrapolating the R_T - time plot to t=0. The value of R_T^o obtained was found to be .080 ohms.

The current carrying leads to the cell were made from copper wire that was about 80 cm long and had a diameter of .158 cm. The resistance of the copper leads can be obtained by solving the general equation for the resistance of a metal conductor[58]

$$R = \frac{\rho l}{A} \qquad 5.4$$

where ρ is the resistivity of the metal, l is the length of the

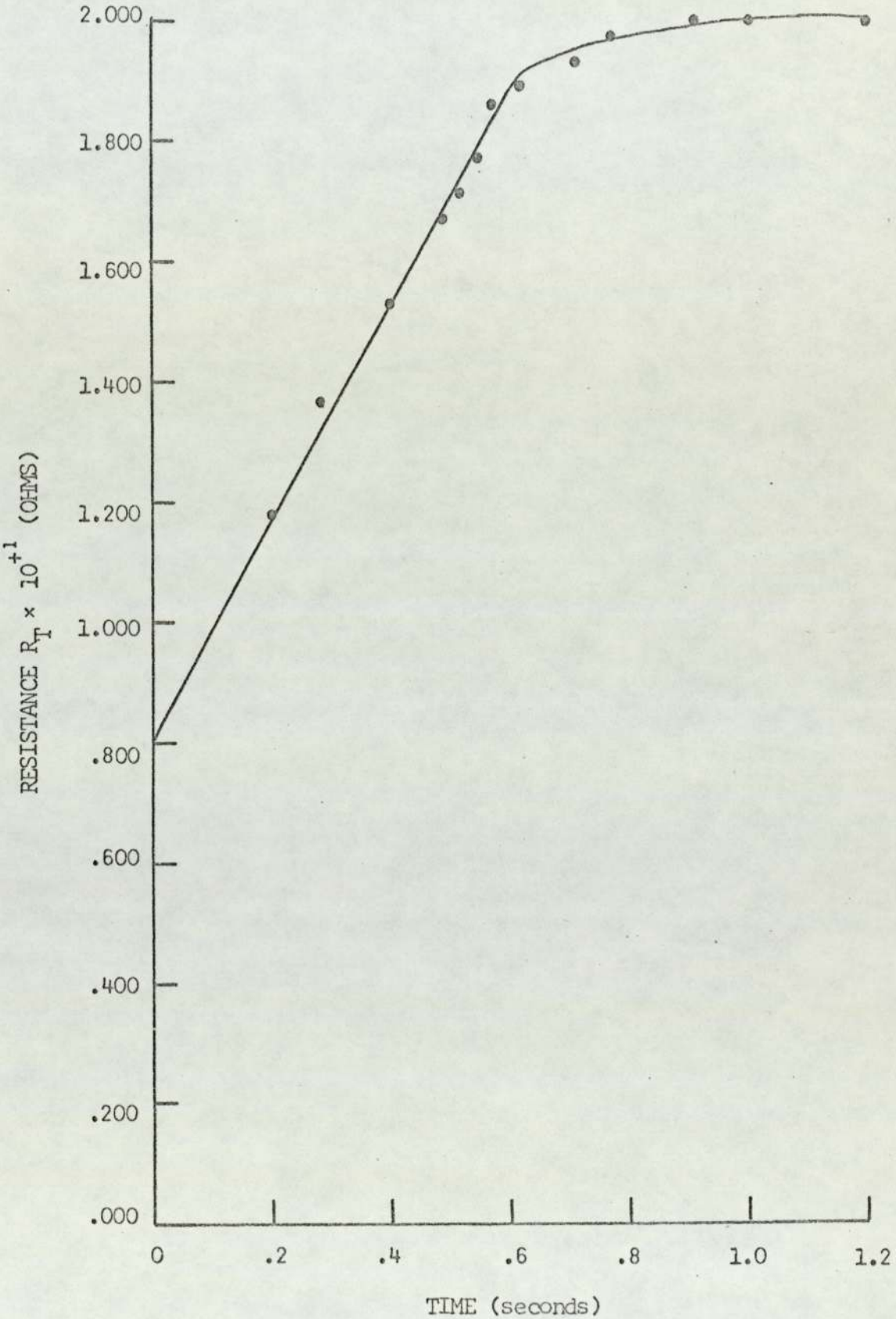

Fig. 19. Resistance R_T as a function of time.

conductor in cm, and A is the cross sectional area in cm^2. The resistivity of copper at 300 K is about 1.5×10^{-6} ohm cm[59]. The initial total resistance of the copper leads R^o_{Cu}, calculated by means of equation 5.4, was found to be .012 ohms.

The stainless steel supports for the tantalum filament were each 2.54 cm long and had an individual cross sectional area of .022 cm^2. If the resistivity of the stainless steel ρ_{ss} was about 30×10^{-6} ohm cm, then from equation 5.4 the initial total resistance R^o_{ss} for the filament supports was calculated to be 0.0069 ohms.

The tantalum filament was 2 cm long and its cross sectional area was 1.25×10^{-3} cm^2. The initial resistance R^o_{Ta} of the tantalum was found to be .0295 ohms.

Equation 5.3. may also be expressed as

$$R^o_T = R^o_{Ta} + R^o_{Cu} + R^o_{ss} + R^o_x \qquad 5.5$$

where R^o_{Ta}, R^o_{Cu}, R^o_{ss} and R^o_x are the initial values of the tantalum filament, copper leads, stainless steel supports, and contact resistances respectively, and R^o_T is the experimentally determined initial total resistance. Upon solving equation 5.5, the initial value of R^o_x was found to be .0316 ohms. The collector circuit contains 12 contacts, and hence the average resistance of each of these contacts would be 0.0025 ohms.

Consider now the temperature rise in the connecting copper leads and the stainless steel filament supports during the thermal desorption reaction. The average collector current in this thermal desorption experiment was about 12 amperes and this would mean that the energy ($I_c^2 R_{Cu}$) dissipated in the copper leads would be about 1.73 watts or .413 calories (gram) sec^{-1}. With the density of the copper and its

specific heat capacity taken as 8.94 grams cm^{-3} [59] and .09 calories $gram^{-1}$ deg^{-1}, the calculated temperature increase in these leads was about 1 K.

The energy ($I_c^2 R_{ss}$) dissipated in the stainless steel supports was calculated to be 1.00 watt or .27 calories (gram) sec^{-1}. If the density of the stainless steel is taken as 7.75 grams cm^{-3} [60] and its heat capacity is estimated from the law of Dulong and Petit, then the temperature increase calculated for the filament supports is about 4 K.

It is well known that the resistivity of a metal, and hence the resistance of a conductor defined by equation 5.4, will be some function of the temperature. The temperature change in the copper leads was calculated to be 1 K. The effect of a temperature change of this magnitude on the resistance of the copper leads will be trivial and thus

$$R_{Cu} = R^{o}_{Cu} \quad . \qquad 5.6$$

The change in resistance of the stainless steel supports, as a result of the 4 K temperature change, can also be ignored and so

$$R_{ss} = R^{o}_{ss} \quad . \qquad 5.7$$

The effect of the collector current on the contact resistance is indeed very hard to estimate. Although the average contact resistance value is quite small, the energy could be dissipated in such a small volume that localized heating could take place. However, the materials involved do have considerable mass, and thus could act as good thermal sinks. It may then be assumed that the contact resistance during the thermal desorption reaction can be expressed as

$$R_x = R^{o}_{x} \quad . \qquad 5.8$$

Now upon rearranging and substituting equations 5.5, 5.6, and 5.7 into equation 5.3, the tantalum filament resistance R_{Ta}, at a given time t, can be expressed as

$$R_{Ta}(t) = R_T(t) - R^o_{Cu} - R^o_{ss} - R^o_x \qquad 5.9$$

or

$$R_{Ta}(t) = (R_T(t) - 0.051) \text{ ohms} . \qquad 5.10$$

The temperature dependence of the resistivity of tantalum has been reported[59]. The resistivity of the collector tantalum filament, for a given time t, can be found by substituting equation 5.10 into 5.4 to obtain

$$\rho_{Ta}(t) = R_{Ta}(t) \frac{A}{l} \qquad 5.11$$

The thermal linear expansion of tantalum between 300 K and 2400 K is reported as 1.7%[59]. This would mean that the resistivity correction due to thermal expansion will be well within the experimental error and thus can be ignored. The temperature of the filament at a time t, is determined by first solving equation 5.11 and reading the temperatures directly from the tantalum resistivity-temperature plot reported in the reference[59].

The collector temperatures, for various times t, are listed in Table I. The collector temperature T as a function of time is illustrated by Fig. 20. The collector temperature appears to be linearly dependent on the time for temperatures up to 2200 K. The temperature obtained at the intercept, when t=0, is approximately that of ambient room temperature and thus does support the use of the above method for the determination of the filament temperature.

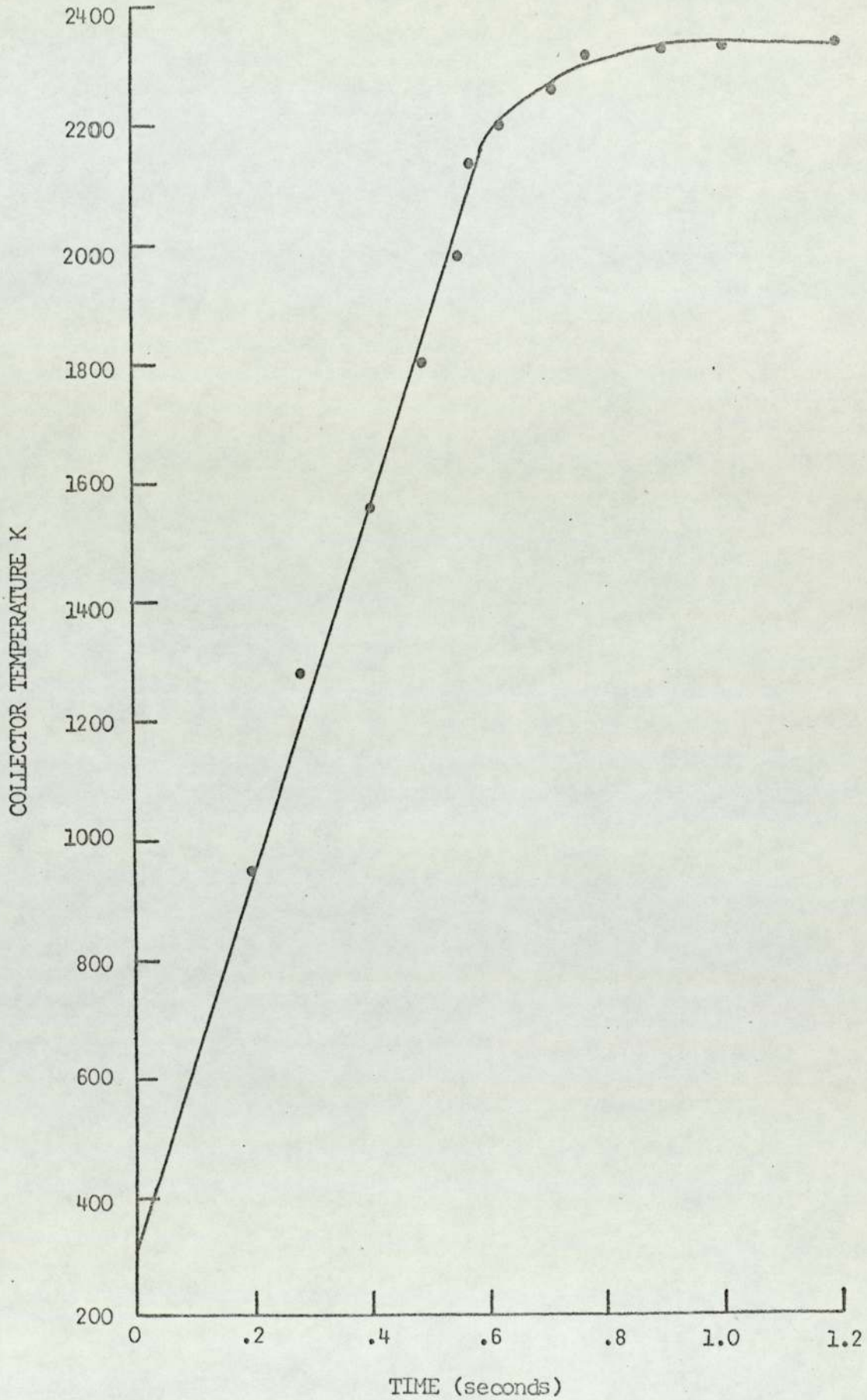

FIG. 20. Collector temperature as a function of time.

5.3. Experimental Procedure

The experimental procedure that was used for the study of the thermal desorption reaction of oxygen from a tantalum surface is as follows:

1. The pressure in the experimental cell was first reduced by the pumpdown procedure that was outlined in section 4.2.5.
2. When the system had reached its ultimate pressure, the tantalum collector filament was then "flashed" to a maximum temperature of about 2200 K. The flashing of the filament was continued until the pressure increase resulting from the flash was consistent.
3. The pressure in the system was then increased by leaking in oxygen from the oxygen supply system. The pressure was controlled by means of the variable leak valve.
4. After a predetermined time, the leak valve was closed and the pressure in the system was allowed to return to the value obtained in step 2.
5. The tantalum filament was then "flashed" and the oscilloscope display was recorded.

5.4. The Analysis of a β_1 Desorption Peak

This section will consider the desorption reaction kinetics of a β_1 peak. The β_1 peak shown in Fig. 18 will not provide enough data points for a complete and accurate analysis, hence the β_1 peak experiment No. 224-3 will be considered and its recorded oscilloscope display is shown in Fig. 21.

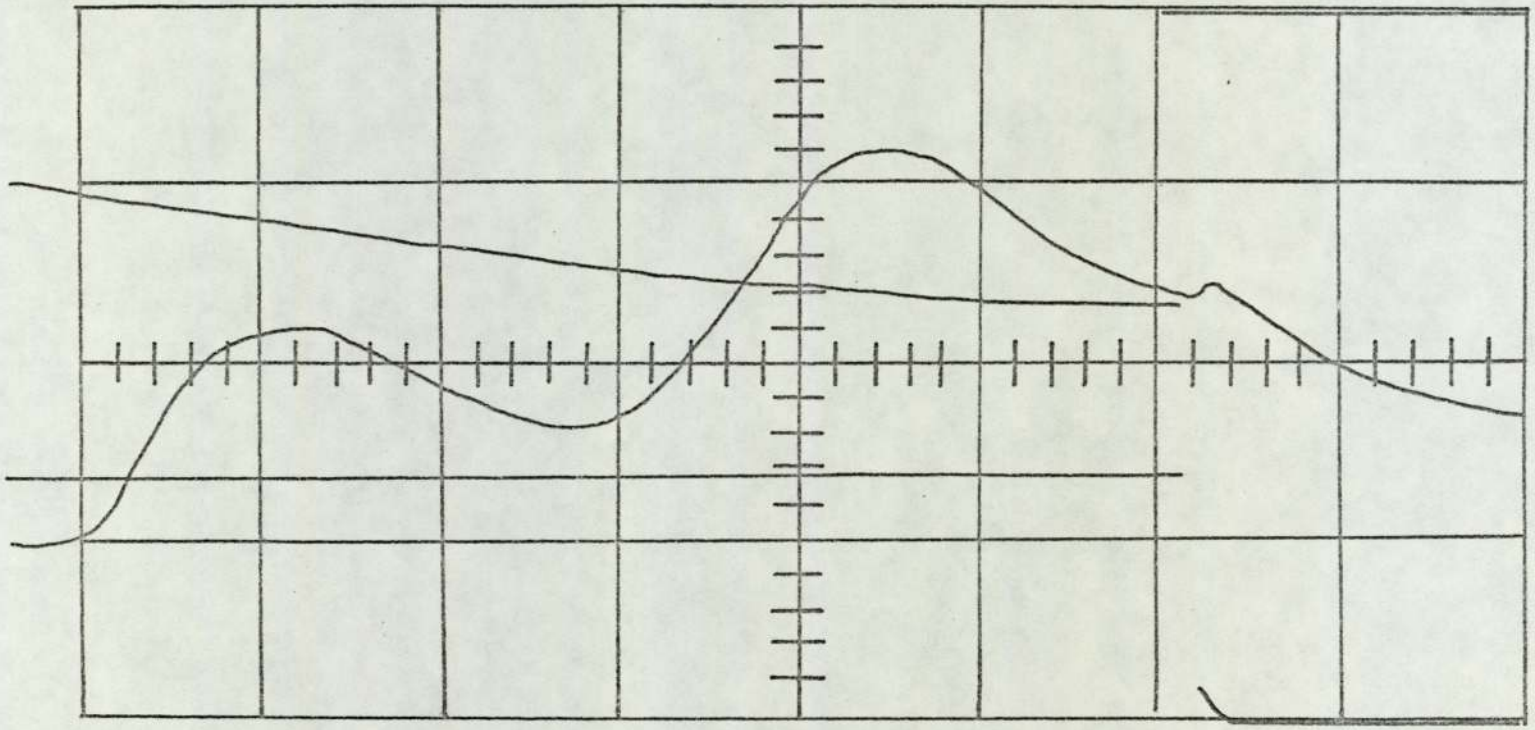

Fig. 21. Thermal desorption spectrum of experiment No. 224-3.

5.4.1. Determination of the rate of desorption as a function of time

The first requirement for the analysis of the data is to obtain the pressure and the filament temperature, at various times t, from the recorded oscilloscope display illustrated by Fig. 21. The method used to obtain this information was described in the previous section and the values that were obtained are listed in Table II.

In section 2.4, the rate of desorption was expressed as

$$\left(\frac{dn}{dt}\right)_t = \left(\frac{dn}{dt}\right)_{t_m} \left[\frac{V}{S_E P_{t_m}} \left(\frac{dP^*}{dt}\right)_t + \frac{P^*_t}{P^*_{t_m}} \right] \quad . \qquad 2.38$$

In order to solve equation 2.38 for $\left(\frac{dn}{dt}\right)_t$, the quantities P^*_t, $P^*_{t_m}$, $\left(\frac{dP^*}{dt}\right)_{t_m}$,, and S_E must be obtained from the experimental data.

The pumping speed S_E was calculated to be 18.5 litres sec^{-1}.

P^* was defined by equation 2.35 and its values at various times during the β_1 thermal desorption reaction are listed in Table III.

A plot of P^*_t as a function of time is shown in Fig. 22. From Fig. 22, the instantaneous slopes $\left(\frac{dP^*}{dt}\right)_t$ can be obtained and values for various times are listed in Table III. The value of $P^*_{t_m}$, obtained directly from Fig. 22, is 17×10^{-8} torr. With the value of $P^*_{t_m}$ known, the values of $\frac{P^*_t}{P^*_{t_m}}$ were determined and are listed in Table III.

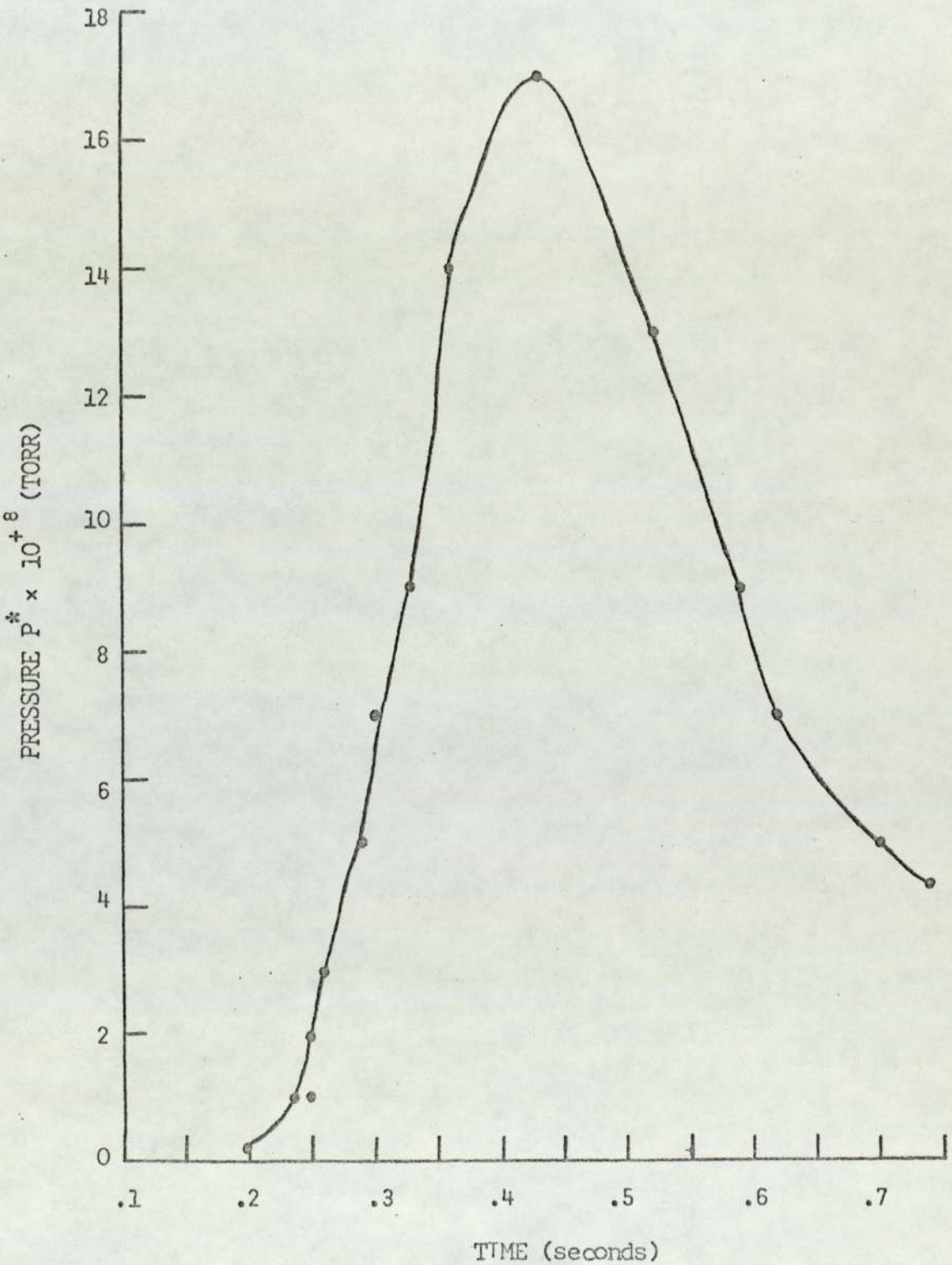

Fig. 22. Pressure P^* as a function of time.

Table II

Observed experimental values of the pressure and calculated values of the collector temperature at various times during the thermal desorption reaction

Time (sec)	Pressure × 10^{+6} (torr.)	Collector temperature (K)
.20	1	905
.24	2	1030
.26	4	1040
.29	6	1065
.30	8	1070
.33	10	1120
.36	15	1160
.43	18	1230
.52	14	1360
.59	10	1400
.62	8	1465
.70	6	1565
.74	5	1610
.80	6	1640
.86	10	1730
.91	20	1810
.94	40	1840
1.00	100	1970
1.20	100	2015
1.30	40	2050
1.40	30	2085
1.44	30	-
1.52	20	-
1.62	10	-
1.70	7	-

Table III

Calculated values of P_t^*, $\left(\frac{dP^*}{dt}\right)_t$, $\frac{P_t^*}{P_{t_m}^*}$, and $\frac{dn}{dt}$ at various times during the β_1 thermal desorption reaction

time (sec)	$P_t^* \times 10^{+8}$ (torr)	$\left(\frac{dP^*}{dt}\right)_t \times 10^{+8}$ (torr sec^{-1})	$\frac{P_t^*}{P_{t_m}^*}$	$\left(\frac{dn}{dt}\right)_t \times 10^{-13}$ (molecules sec^{-1} cm^{-2})
.20	0	12	0	0
.24	1	40	.059	.506
.26	3	86	.176	1.08
.29	5	120	.294	1.14
.30	7	120	.411	1.64
.33	9	120	.530	1.77
.36	14	100	.825	1.90
.43	17	0	1.000	1.96
.52	13	-57	.765	1.06
.59	9	-57	.530	.175
.62	7	-40	.411	.074
.70	5	-17	.294	-
.74	4	-13	.259	-

The last value that is necessary in order to solve for $\left(\frac{dn}{dt}\right)_t$, by means of equation 2.38, is $\left(\frac{dn}{dt}\right)_{t_m}$. This value can be obtained directly by solving equation 2.36. The value of K used in equations 2.36 and 2.38 is given as $3.27 \times 10^{+19}$ molecules litre^{-1} torr^{-1} 15 and hence the value $\left(\frac{dn}{dt}\right)_{t_m}$ for the β_1 desorption reaction is $1.06 \times 10^{+13}$ atoms or molecules^{-1} cm^{-2}. The calculated values of the rate of desorption $\left(\frac{dn}{dt}\right)_t$ are tabulated in Table III.

5.4.2. Calculation of the coverage of the surface

The initial coverage of the surface σ_o can be obtained by solving equation 2.39. The required integration was accomplished by graphical means. From the values given in Table III, a plot of $\left(\frac{dn}{dt}\right)_t$ versus time was made and is illustrated by Fig. 23. The areas under the curve, for a number of time intervals, were determined. The initial surface coverage σ_o was determined from the total area and was found to be $3.7 \times 10^{+12}$ atoms or molecules cm^{-2}. The surface coverage at any time during the desorption reaction $(\sigma_o - \sigma_t)$ can be determined from equation 2.40. The values of $(\sigma_o - \sigma_t)$ are listed in Table IV.

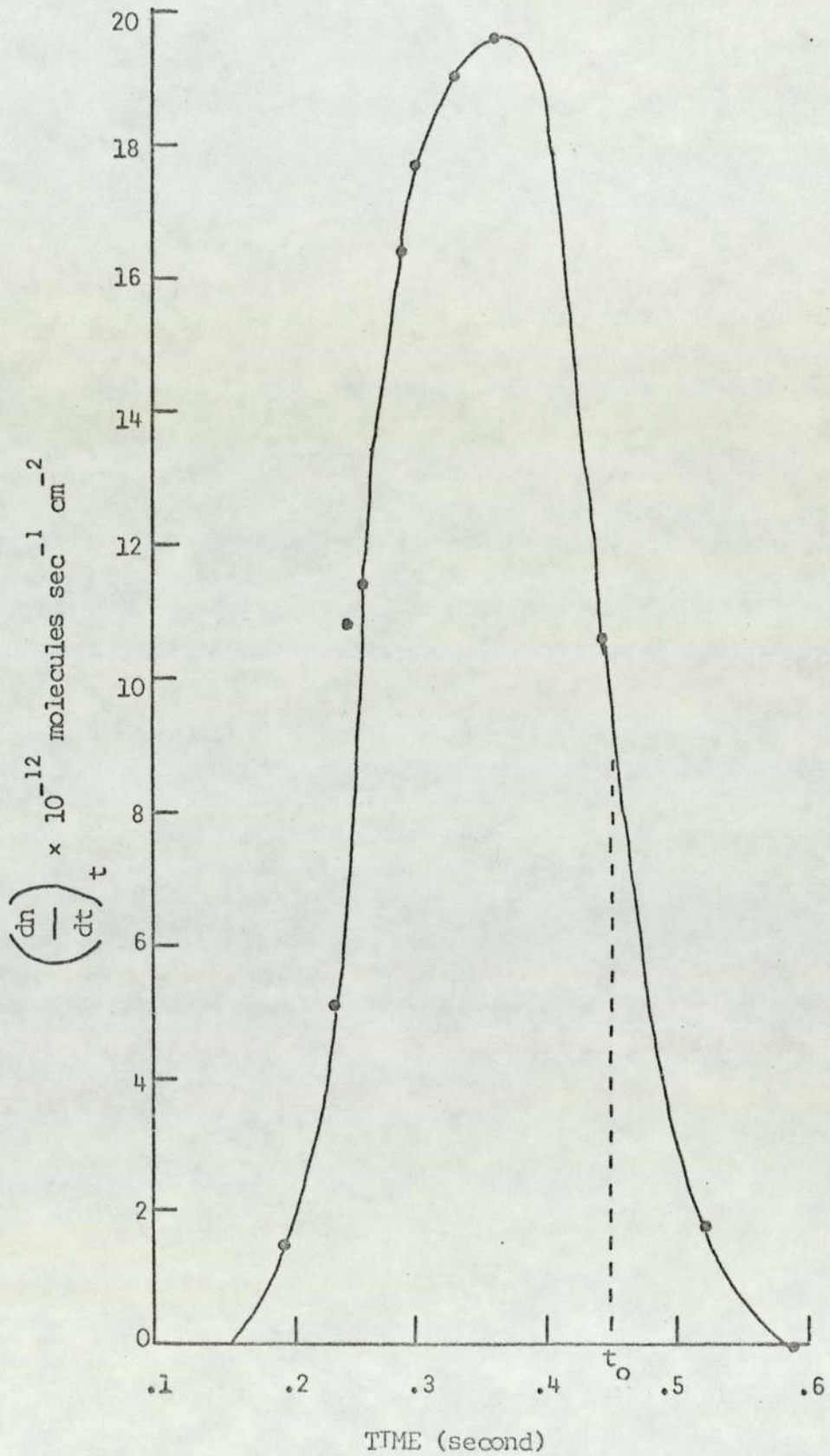

Fig. 23. The rate of desorption as a function of time.

Table IV

A list of experimentally determined values used to examine the kinetics of β_1 reaction

time (sec)	$(\sigma_o - \sigma_t) \times 10^{-12}$ (molecules cm^{-2})	$\left(\frac{dn}{dt}\right)_t \times 10^{-12}$ (molecules sec^{-1} cm^{-2})	$\frac{(dn/dt)_t \times 10^{+4}}{(\sigma_o - \sigma_t)\,T}$ (sec^{-1} deg^{-1})	$\frac{(dn/dt)_t \times 10^{+16}}{(\sigma_o - \sigma_t)^2\,T}$ (cm^2 molecules^{-1} sec^{-1} deg^{-1})	T (K)
.20	3.70	1.53	4.31	.117	960
.23	3.66	4.00	10.9	.298	1000
.25	3.56	8.00	21.9	.617	1020
.27	3.36	13.0	37.1	1.08	1050
.30	2.90	17.4	56.1	1.92	1080
.32	2.54	18.6	66.3	2.62	1105
.35	1.97	19.4	86.4	4.39	1140
.38	1.39	19.4	118.0	8.49	1180

Table IV (continued)

time (sec)	$(\sigma_o - \sigma_t) \times 10^{-12}$ (molecules cm^{-2})	$\left(\frac{dn}{dt}\right)_t \times 10^{-12}$ (molecules sec^{-1} cm^{-2})	$\frac{(dn/dt)_t \times 10^{+4}}{(\sigma_o - \sigma_t)\,T}$ (sec^{-1} deg^{-1})	$\frac{(dn/dt)_t \times 10^{+16}}{(\sigma_o - \sigma_t)^2\,T}$ (cm^2 $molecules^{-1}$ sec^{-1} deg^{-1})	T (K)
.40	1.01	18.8	157.0	15.7	1200
.42	.680	15.0	176.0	25.1	1260
.45	.334	9.20	212.0	64.4	1300
.48	.144	4.60	242.0	129.0	1320
.50	.080	2.80	254.0	316.0	1380
.55	.006	-	-	-	-
.58	-	-	-	-	-

5.4.3. Determination of the order of the reaction

The order of the reaction can be ascertained from a plot of

$$\ln \frac{(dn/dt)_t}{(\sigma_o - \sigma_t)^{n'} T}$$ as a function of (1/T). The values of $(\sigma_o - \sigma_t)$ were obtained from Table IV. The corresponding values of $(dn/dt)_t$ and T were obtained from Fig. 23 and a temperature-time plot similar to that illustrated by Fig. 20. These latter values of $(dn/dt)_t$ and T are listed in Table IV.

The integer n' can be assumed to have a numerical value of either 1 or 2, and thus the order is determined by observing which of the two values of n' will produce the best straight line plot. First and second order plots for the β_1 reaction are illustrated in Fig. 24. It is apparent from inspection of these plots that the β_1 thermal desorption reaction is second order.

5.4.4. Determination of the heat of activation energies, the change in entropy and the standard free energy for the reaction

The experimental activation energy ΔE_p was determined by solving equation 2.41. The value of $d\left[\ln \frac{(dn/dt)_t}{(\sigma_o - \sigma_t)^{n'} T}\right] / d(1/T)$ was obtained from the slope of the second order plot. The calculated value of ΔE_p was 47.8 kcal mol^{-1} or 200 kJ mol^{-1}.

The standard state for the desorption reaction was defined in section 2.3. and a method for its determination was presented in section 2.4. The time t_o was determined from Fig. 23 as .45 seconds and this corresponds to a filament surface temperature T_o of 1300 K.

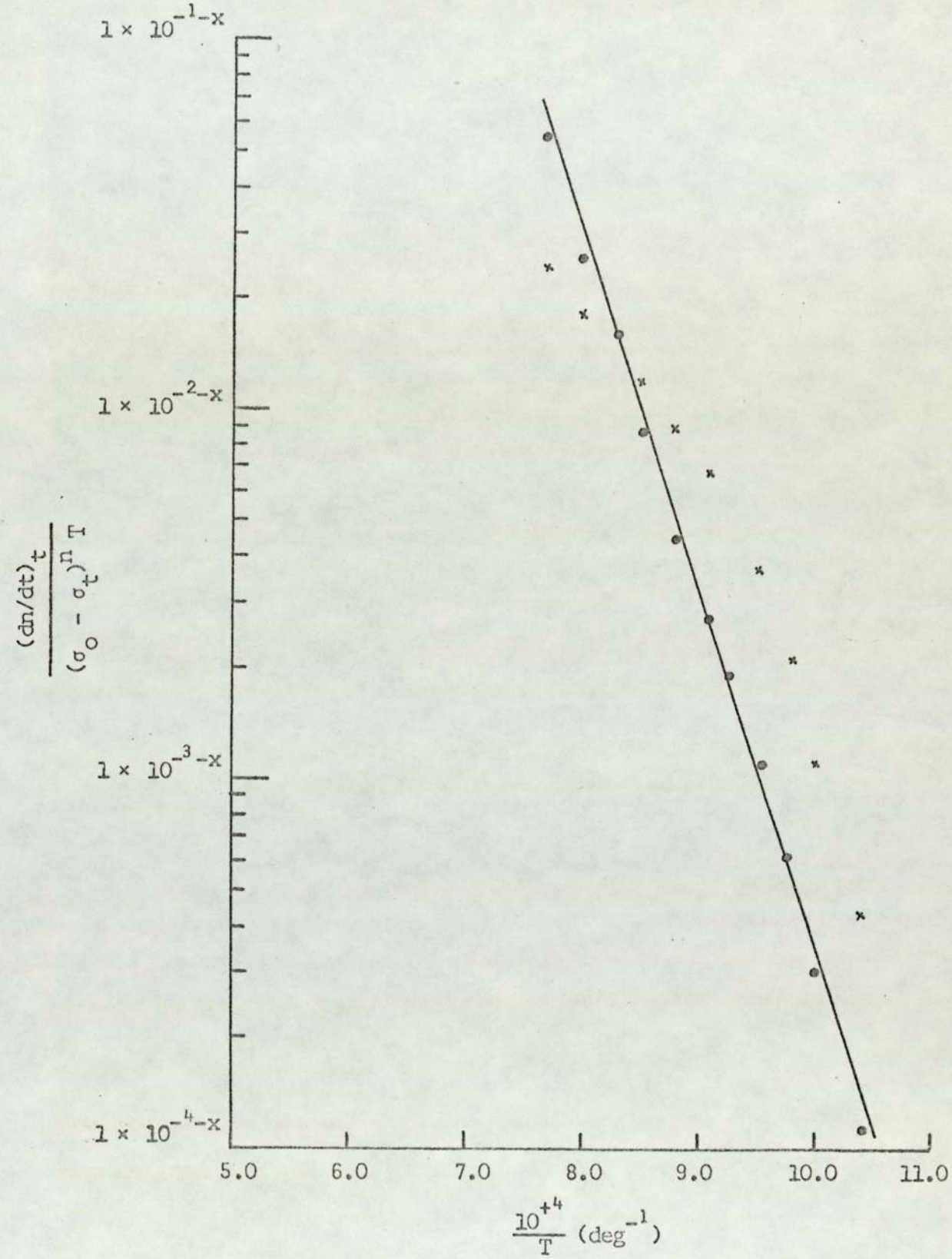

Fig. 24. $\ln \frac{(dn/dt)_t}{(\sigma_o - \sigma_t)^n T}$ as a function of (1/T);
(n=1) × , (n=2) ● .

The standard heat of activation was given as

$$\Delta H^{\ddagger} = \Delta E_p - RT_o \quad . \qquad 2.29$$

Substitution of ΔE_p and T_o into equation 2.29 gave a $\Delta H^{\ddagger}$ value of 45.2 kcal mol^{-1} or 189 kJ mol^{-1}.

In order to determine the change in entropy of the reaction $\Delta S^{\ddagger}$, equation 2.30 is now expressed as

$$\Delta S^{\ddagger} = R \left[\ln \left(\frac{dn}{dt} \right)_{t=.45} - \ln \left[1 \times 10^{-15} (\sigma_o - \sigma_{.45}) \right] - 1 \right]$$

$$+ \frac{47.8}{1300} \text{ kcal mol}^{-1} \text{ deg}^{-1} . \qquad 5.12$$

The values of $(dn/dt)_{.45}$ and $(\sigma_o - \sigma_{.45})$ can be obtained from Table IV. Upon substitution of these latter values into equation 5.12, the change in entropy $\Delta S^{\ddagger}$ was calculated to be 44.2 calorie mol^{-1} deg^{-1} or 185 J mol^{-1}.

The standard free energy of the reaction can be determined from

$$\Delta G^{\ddagger} = \Delta H^{\ddagger} - T_o \Delta S^{\ddagger} \quad . \qquad 2.31$$

The values of $\Delta H^{\ddagger}$, T_o, and $\Delta S^{\ddagger}$ have been determined above, and hence the value of $\Delta G^{\ddagger}$ for this reaction is found to be -12.0 kcal mol^{-1} or -50.1 kJ mol^{-1}.

In this section, the standard heat of activation and the standard free energy change were determined for the β_1 peak of a thermal desorption experiment. The result of this analysis of the β_1 peak is given in Table V.

Table V

The results of the analysis of
a β_1 desorption reaction

Derived Parameter	Calculated value
S_E	18.5 litres sec^{-1} $1.85 \times 10^{+4}$ $meter^3$ sec^{-1}
$(dn/dt)_{t_m}$	$1.06 \times 10^{+13}$ molecules sec^{-1} cm^{-2} $1.06 \times 10^{+17}$ molecules sec^{-1} $meter^{-2}$
σ_o	$3.7 \times 10^{+12}$ molecules cm^{-2} $3.7 \times 10^{+17}$ molecules $meter^{-2}$
Order of the reaction	Second
ΔE_p	47.8 kcal $mole^{-1}$ 200. kJ $mole^{-1}$
T_o	1300 K
$\Delta H^{\ddagger}$	45.2 kcal $mole^{-1}$ 189. kJ $mole^{-1}$
$\Delta S^{\ddagger}$	44.2 cal $mole^{-1}$ deg^{-1} 185. J $mole^{-1}$ deg^{-1}
$\Delta G^{\ddagger}$	-12.0 kcal $mole^{-1}$ -50.1 kJ $mole^{-1}$

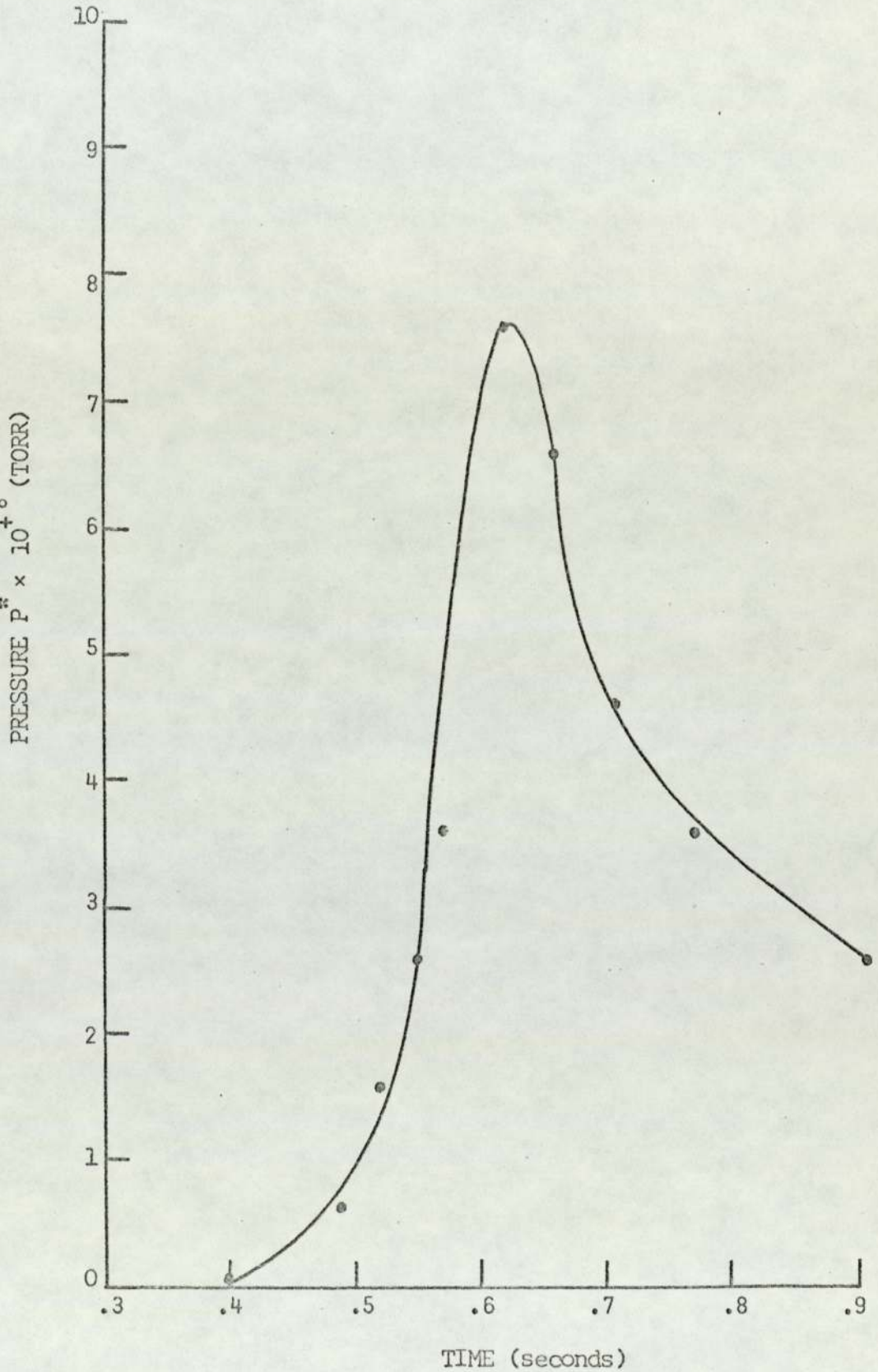

Fig. 25. Pressure P^* as a function of time.

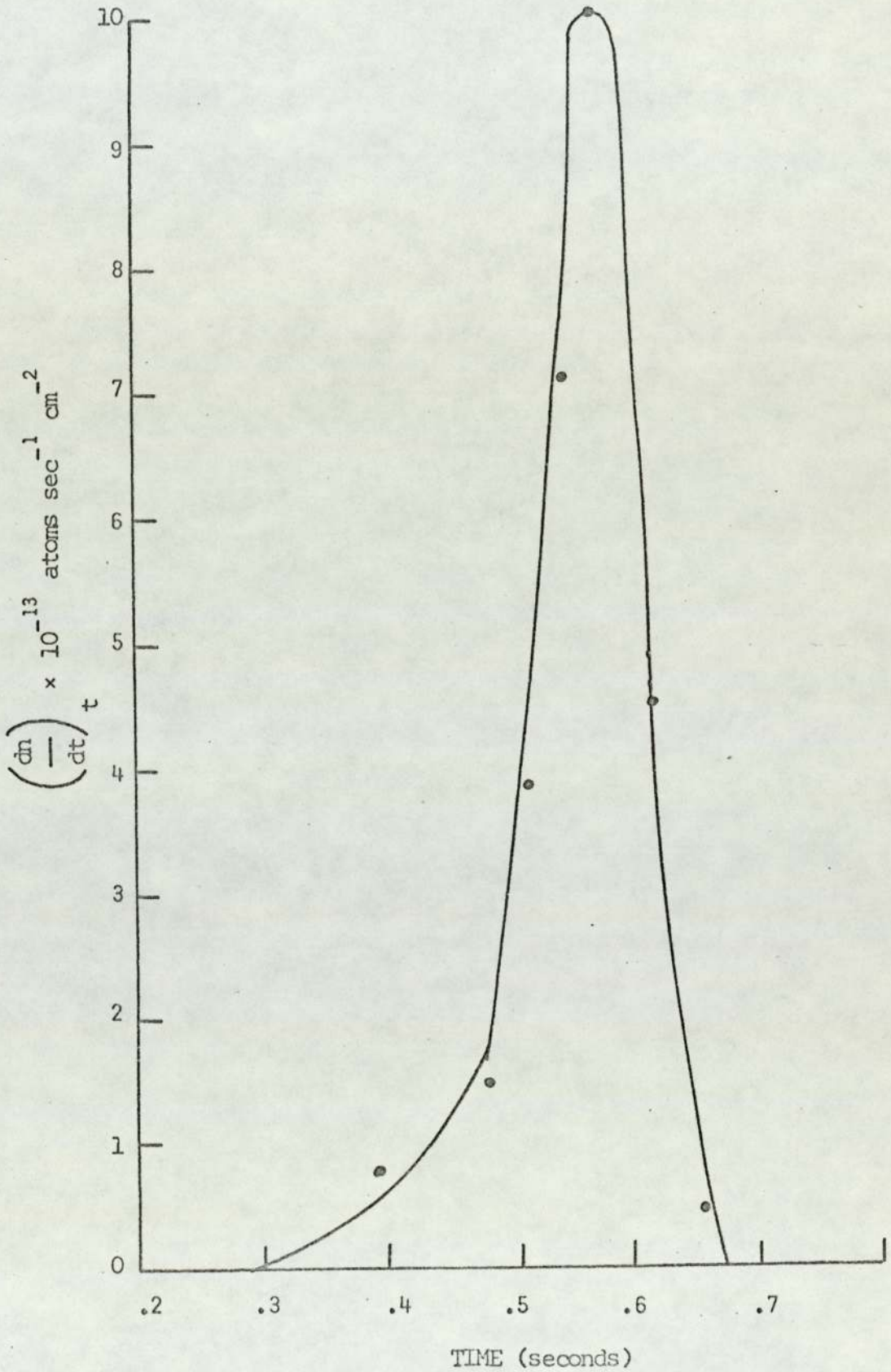

Fig. 26. The rate of desorption as a function of time.

5.5. The Analysis of a β_2 Desorption Peak

The desorption spectrum of experiment illustrated in Fig. 18 was selected to illustrate a typical analysis of a β_2 desorption reaction. The filament temperature as a function of time has already been determined and was shown in Fig. 20. The pressure P_t at various times t has been listed in Table I

5.5.1. Determination of the rate of desorption as a function of time

The values of P^*_t, $P^*_{t_m}$, and $(dP^*/dt)_{t_m}$ were obtained in a manner similar to that used in section 5.4.1. for the analysis of the β_1 peak. The values of P^*_t are tabulated in Table VI.

A plot of P^*_t as a function of time is illustrated by Fig. 25. The instantaneous slopes $(dP^*/dt)_t$ listed in Table VI were obtained in the same manner as those in section 5.4.1. The value of $(dn/dt)_{t_m}$ was calculated to be $4.51 \times 10^{+13}$ atoms or molecules sec^{-1} cm^{-2}. The calculated values of the rate of desorption $(dn/dt)_t$ for this reaction are tabulated in Table VI.

5.5.2. Calculation of the coverage of the surface

The determination of the initial surface coverage σ_o and the coverage $(\sigma_o - \sigma_t)$ at a given time t were determined, as in section 5.4.2., from a plot of $(dn/dt)_t$ as a function of time. The plot of $(dn/dt)_t$ versus time is illustrated by Fig. 26. The initial surface coverage σ_o was found to be about $1 \times 10^{+13}$ atoms or molecules cm^{-2}. The values of $(\sigma_o - \sigma_t)$ for various times during the thermal desorption reaction are tabulated in Table VII.

Table VI

Calculated values of P_t^*, $(dP^*/dt)_t$, (P_t^*/P_{t_m}), and $(dn/dt)_t$ at various times during the thermal desorption

Time (sec)	P_t^* (torr) $\times 10^{+8}$	$(dP^*/dt)_t \times 10^{+8}$ (torr sec^{-1})	$P_t^*/P_{t_m}^*$	$(dn/dt)_t \times 10^{-13}$ (atoms sec^{-1} cm^{-2})
.40	.0	4.29	0	.478
.49	.6	10.1	.079	1.48
.52	1.6	26.6	.210	3.88
.55	2.6	50.0	.342	7.13
.57	3.6	71.5	.474	10.1
.62	7.6	0	1.00	4.51
.66	6.6	-30.8	.869	.469
.71	4.6	24.7	.606	-.031

Table VII

A list of experimentally determined values used to examine the kinetics of the β_2 reaction

time (sec)	$\sigma_t \times 10^{-12}$ (atoms cm^{-2})	$(\sigma_o - \sigma_t) \times 10^{-12}$ (atoms cm^{-2})	$(dn/dt)_t \times 10^{-12}$ (atoms sec^{-1} cm^{-2})	$\frac{(dn/dt)_t \times 10^{+4}}{(\sigma_o - \sigma_t)\,T}$ (sec^{-1} deg^{-1})	$\frac{(dn/dt)_t \times 10^{+16}}{(\sigma_o - \sigma_t)^2\,T}$ (cm^{+2} $atoms^{-1}$ sec^{-1} deg^{-1})	T (K)	$1/T \times 10^{+4}$ (deg^{-1})
.40	.31	9.64	7.80	5.19	.381	1560	6.42
.45	.78	9.17	11.7	7.52	.816	1710	5.88
.50	1.46	8.49	18.0	11.3	1.33	1870	5.35
.53	2.32	7.63	45.0	30.2	3.98	1950	5.13
.55	3.44	6.51	71.3	54.4	9.86	2010	4.98
.57	5.12	4.83	101.0	101.0	20.6	2080	4.80
.60	7.86	2.09	74.0	163.0	37.4	2181	4.60
.62	9.01	.95	45.1	215.0	225	2200	4.54
.65	9.79	.16	13.0	368	367	2210	4.52
.70	9.95	-	-	-	-	-	-

5.5.3. Determination of the order of the reaction

The order of the reaction was determined in the same manner as that for β_1 peak in section 5.4.3., i.e., from a plot of the

$$\ln \frac{(dn/dt)_t}{(\sigma_o - \sigma_t)^{n'} T}$$ as a function of 1/T when n' can assume a value

of either 1 or 2. The values of $(\sigma_o - \sigma_t)$ were obtained from Table VII and the corresponding values of $(dn/dt)_t$ and T were obtained from Fig. 26 and Fig. 20 respectively. An inspection of these first and second order plots that are shown in Fig. 27 indicates that the best straight line fits that of the first order reaction.

5.5.4. Determination of the heat of activation energies, the change in entropy and the standard free energy for the desorption reaction

The experimental activation energy ΔE_p was determined by solving equation 2.40. The value of $d\left[\ln \frac{(dn/dt)_t}{(\sigma_o - \sigma_t) T}\right] / d(1/T)$ was obtained from the first order plot shown in Fig. 27. The calculated value of ΔE_p was 82.2 kcal mol^{-1} or 334 kJ mol^{-1}.

The time t_o, for the standard state, was determined from Fig. 26 and was found to be .62 seconds. This time value corresponds to a standard state filament temperature T_o of 2200 K.

The standard heat of activation $\Delta H^{\ddagger}$ was obtained by solving equation 2.29. The calculated value of $\Delta H^{\ddagger}$ for this reaction was found to be 77.8 kcal mol^{-1} or 326 kJ mol^{-1}.

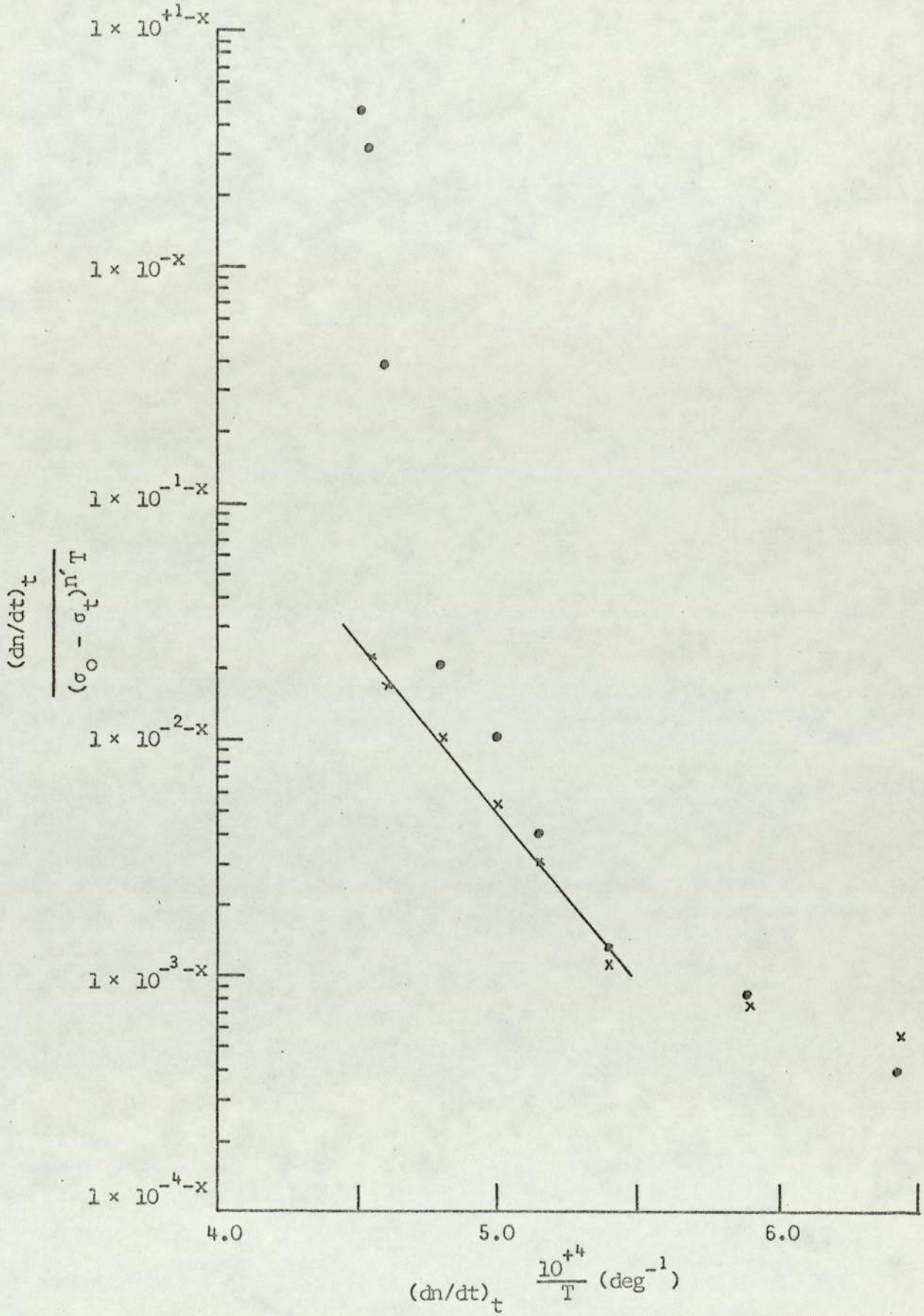

Fig. 27. $\ln \frac{(dn/dt)_t}{(\sigma_o - \sigma_t)^{n'} T}$ as a function of (1/T);

(n′=1) × , (n′=2) • .

In order to determine the change in entropy $\Delta S^{\ddagger}$, equation 2.30 is now expressed as

$$\Delta S^{\ddagger} = R\left[\ln (dn/dt)_{t=.62} - \ln (\sigma_o - \sigma_{.63}) - 1\right] + \frac{82.2}{2200} \text{ kcal mol}^{-1} \text{ deg}^{-1} \quad . \qquad 5.13$$

By solving equation 5.13, the value of $\Delta S^{\ddagger}$ was determined to be 41.9 cal. mol^{-1} deg^{-1} or 175 J mol^{-1} deg^{-1}.

The standard free energy $\Delta G^{\ddagger}$ for the β_2 reaction was obtained by solving equation 2.31. The $\Delta G^{\ddagger}$ for this desorption reaction was calculated to be -26.7 kcal mol^{-1} or -104 kJ mol^{-1}. The results of these experiments are tabulated in Table VIII.

5.6. The Effect of the Residual Gases on the Thermal Desorption Spectrum

One of the main objectives of this thesis was to study the interaction of oxygen on a tantalum surface, but before any signnificance can be assigned to the results it must be clearly established that the observed desorption spectrum can only be attributed to adsorbed oxygen. The following will be a discussion on the various sources of gas contamination and the interpretation of the resulting desorption spectrum.

5.6.1. The effects of the residual gases on the thermal desorption spectrum

The thermal desorption spectrum shown in Fig. 28 was obtained by

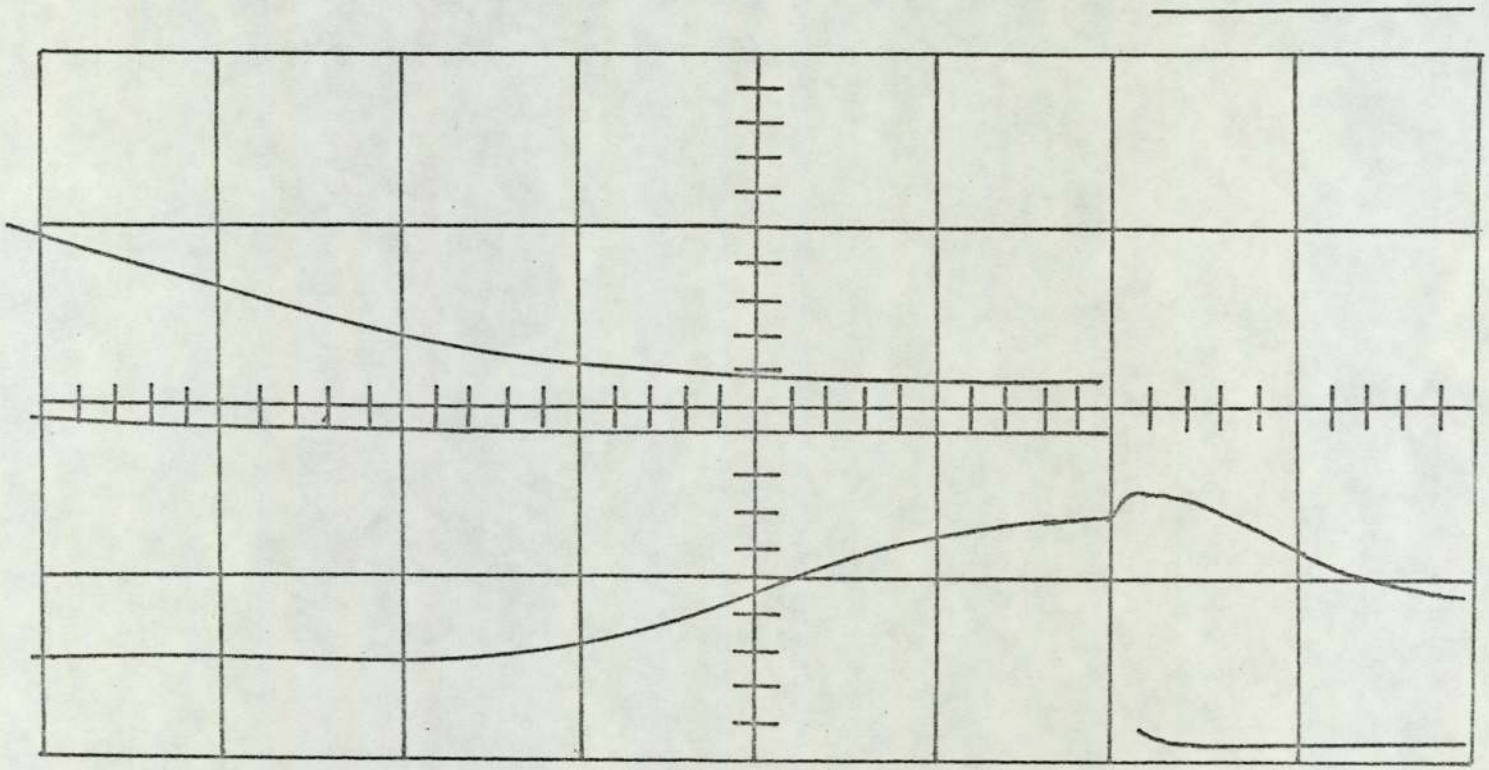

Fig. 28. Thermal desorption spectrum of residual gases after an adsorption time of three minutes.

Table VIII

The results of the analysis of the
β_2 thermal desorption reaction

Derived Parameter	Calculated values
S_E	15.3 litres sec^{-1} $1.54 \times 10^{+4}$ $meter^3$ sec^{-1}
$(dn/dt)_{t_m}$	$4.5 \times 10^{+13}$ atoms sec^{-1} cm^{-2} $4.5 \times 10^{+17}$ atoms sec^{-1} $meter^{-2}$
σ_o	$1 \times 10^{+13}$ atoms cm^2 $1 \times 10^{+17}$ atoms $meter^2$
Order of the reaction	First
ΔE_p	82.2 kcal $mole^{-1}$ 334. kJ $mole^{-1}$
T_o	2200 K
$\Delta H^{\ddagger}$	77.8 kcal $mole^{-1}$ 326. kJ $mole^{-1}$
$\Delta S^{\ddagger}$	41.9 cal $mole^{-1}$ deg^{-1} 175. J $mole^{-1}$ deg^{-1}
$\Delta G^{\ddagger}$	-26.7 kJ $mole^{-1}$ -104 kJ $mole^{-1}$

the following experiment:

1. The first two steps of the experimental procedure, outlined in section 5.3., were completed.
2. With the pressure of the system at about 5×10^{-9} torr, the residual gases of the system were allowed to interact with the tantalum collector for about 3 minutes.
3. The adsorbed gases were then thermally desorbed and the desorption spectrum recorded.

A second experiment was conducted, which was similar to the one described above. The time that the residual gases were exposed to the tantalum surface was about 3 hours. The resulting desorption spectrum is illustrated in Fig. 29.

The effect of the residual gases on the desorption spectrum can be seen by a comparison of Fig. 28 and Fig. 29. In Fig. 29, the effect of the residual gases is to increase the overall pressure level of the desorption spectrum. The β_1 peak is just about detectable, while the β_2 peak is much more pronounced. The complete β_2 peak is obscured by the desorption of gases from the walls of the experimental cell.

5.6.2. The effects of the desorption of gases from the sublimation pump on the thermal desorption spectrum

The only gas that is generally evolved from the titanium filament during its heating cycle is hydrogen. After a time, this gas is removed from the system by adsorption on the cooled titanium film. The sublimation pump does not represent a source of gas contamination, during its off period, provided the liquid nitrogen level is properly maintained. If the level of the liquid nitrogen is allowed to subside

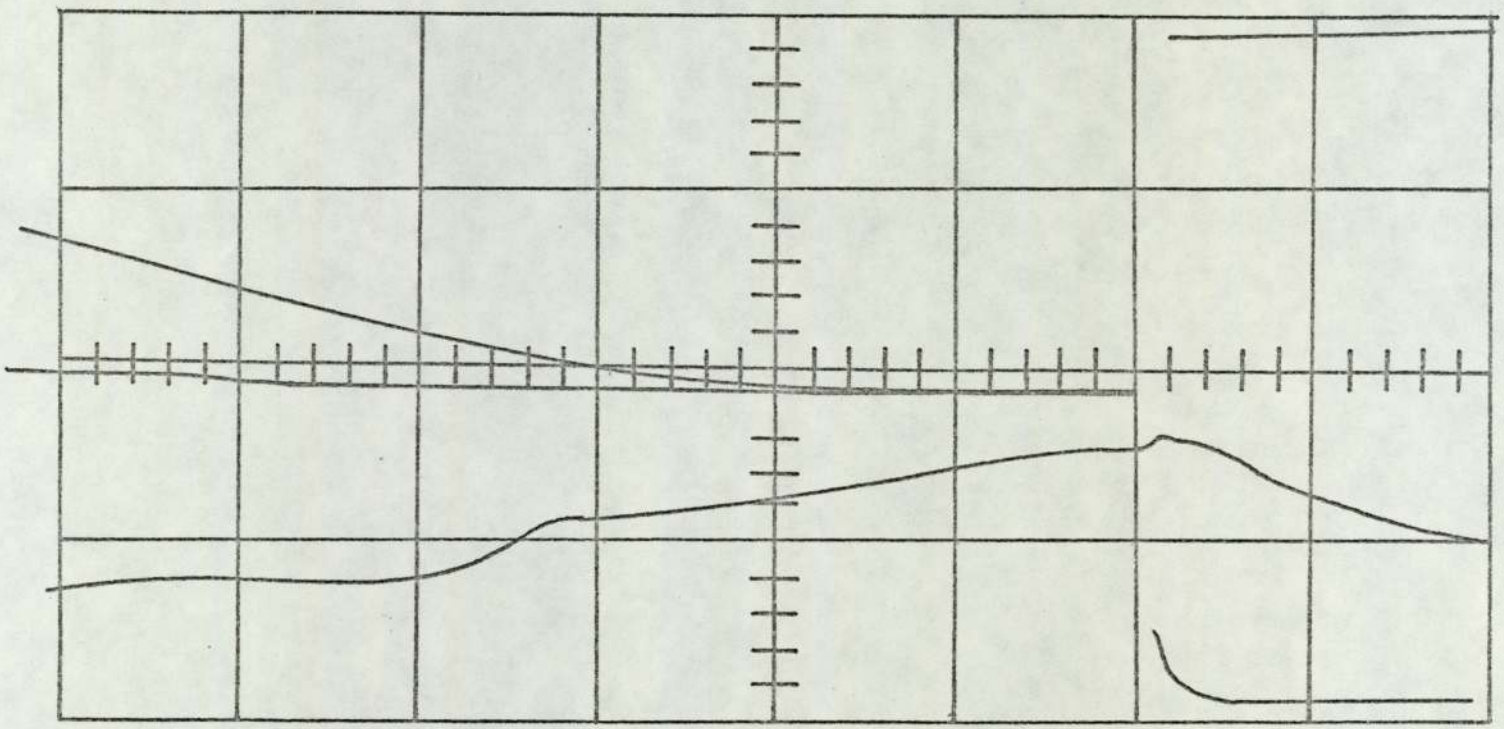

Fig. 29. Thermal desorption spectrum of residual gases after an adsorption time of three hours.

significantly, then gases are desorbed from the walls of the pump chamber. These desorbed gases could then interact with the tantalum surface.

A typical thermal desorption reaction of gases evolved from the titanium sublimation pump is illustrated in Fig. 18. Inspection of all the thermal desorption reactions, involving the desorption of sublimation pump gases, showed that the intensity of the β_1 peak was considerably smaller than that of the β_2 peak. The results of a number of experiments showed that the average maximum pressure P^*_{max} for the β_1 peak occurred at a temperature of about 1260 K, while the average pressure maximum P^*_{max} for the β_2 peak was found to occur at a temperature of 2090 K.

The values of P^* for the β_1 peak were, in general, so small that it was difficult to get a significant number of experimental points for a complete analysis. A significant number of experiment data points were obtained from experiment No. 231-1 and the results of the analysis of the desorption peak are tabulated in Table IX.

5.6.3. The effects of the thermal desorption of gases from the walls of the experimental cell on the thermal desorption spectrum

The desorption spectrum thus far has shown that when the temperature of the collector exceeds about 2000 K, there is gas desorption from the walls of the experimental reaction cell. An experiment was undertaken to examine the effect that these gases will have on the desorption spectrum.

The collector filament was first flashed clean by the procedure outlined in section 5.2. The emitter filament, as shown in Fig. 14, was heated to a temperature of about 1300 K for about 10 minutes.

Table IX

Results of the analysis of the
β_1 peak of experiment No. 231-1

Derived Parameter	Calculated value
S_E	18.0 litres sec^{-1} $1.8 \times 10^{+4}$ $meter^3$ sec^{-1}
$(dn/dt)_{t_m}$	$2.68 \times 10^{+12}$ molecules sec^{-1} cm^{-2} $2.68 \times 10^{+16}$ molecules sec^{-1} $meter^{-2}$
σ_o	$1.9 \times 10^{+12}$ atoms cm^{-2} $1.9 \times 10^{+16}$ atoms $meter^{-2}$
Order of the reaction	Second
ΔE_p	43.5 kcal $mole^{-1}$ 182. kJ $mole^{-1}$
T_o	1080 K
$\Delta H^{\ddagger}$	41.3 kcal $mole^{-1}$ 173. kJ $mole^{-1}$
$\Delta S^{\ddagger}$	56.6 cal $mole^{-1}$ 237. J $mole^{-1}$
$\Delta G^{\ddagger}$	-7.5 kcal $mole^{-1}$ -31.3 kJ $mole^{-1}$

There was no significant increase in pressure during the heating of the emitter. After the emitter filament was turned off, the gases on the collector filament were desorbed and the desorption spectrum recorded. The desorption spectrum obtained is shown in Fig. 21.

5.6.4. Summary

This section of Chapter 5 has been concerned with the effects that various sources of gas contamination can have on the thermal desorption spectrum. It was shown that for adsorption times much less than three hours, the effects of the residual gases on the analysis of the desorption spectrum can be neglected. The desorption spectrum can be serious effected, however, from gases desorbed from the chamber walls of the sublimation pump or from the walls of the reaction cell.

5.7 The Thermal Desorption of Oxygen from a Tantalum Surface

The desorption spectrum of oxygen on tantalum is shown in Fig. 30. This desorption spectrum was obtained by following the experimental procedure outlined in section 5.3. The adsorption time for this reaction was two hours at an oxygen pressure of 5×10^{-8} torr.

Inspection of the desorption spectrum shows that there are two peaks present. A comparison between the oxygen desorption and the residual gas spectrum was accomplished by superimposing Fig. 29 on to Fig. 30. The results of this comparison showed that β_1 peak could only be attributed to the adsorption of oxygen. The results of the β_1 analysis are listed in Table X.

The rate expression of the desorption reaction was defined by equation 2.21. From the results of the analysis of the thermal desorption spectrum of oxygen from the β_1 state, the rate equation for

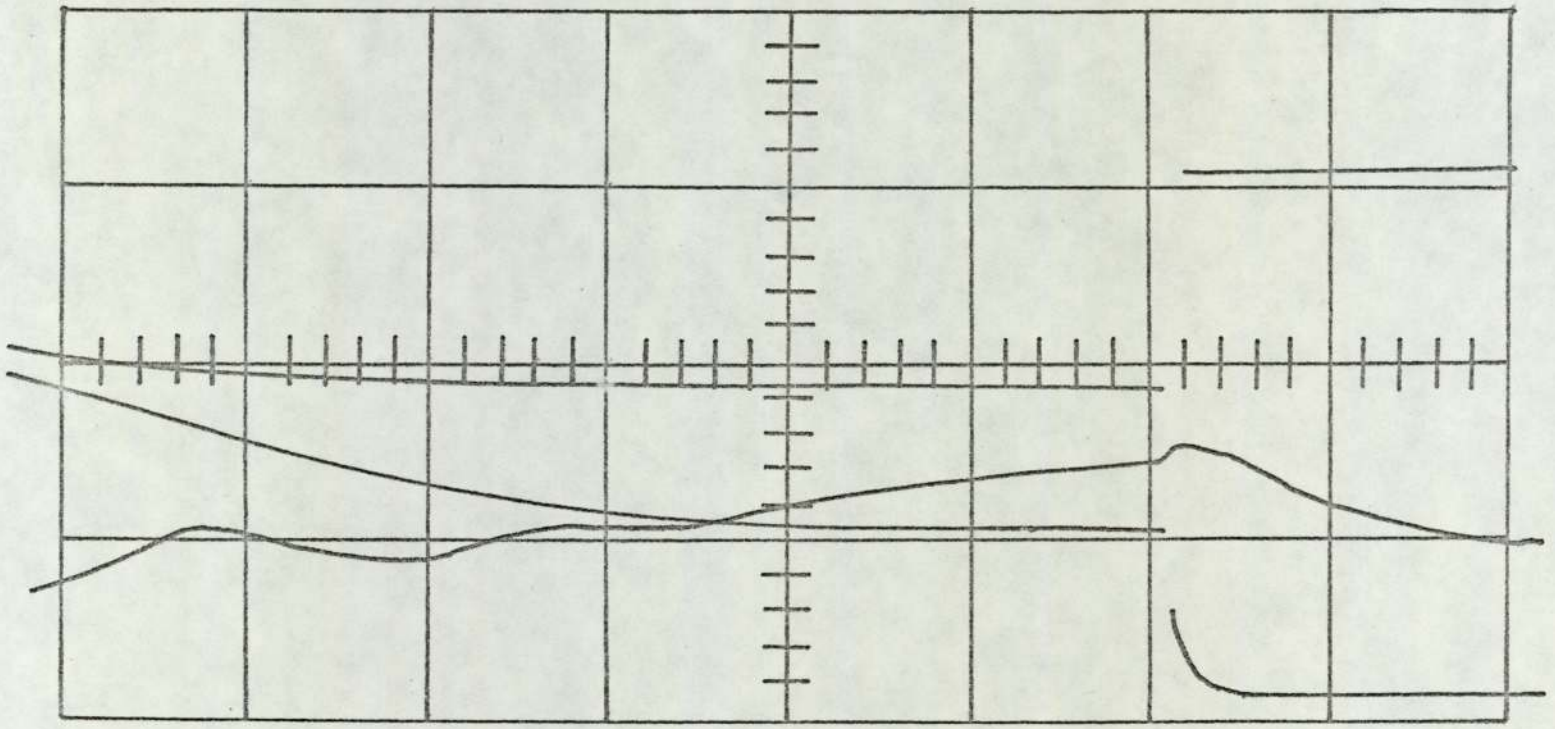

Fig. 30. Thermal desorption spectrum of oxygen after two hours at a pressure of 5×10^{-8} torr.

Table X

Results of the analysis of the thermal desorption spectrum of oxygen from a tantalum surface

Derived Parameter	Calculated value
S_E	13.8 litres sec^{-1} $1.38 \times 10^{+4}$ $meter^{3}$ sec^{-1}
$(dn/dt)_{t_m}$	$2.7 \times 10^{+11}$ molecules sec^{-1} cm^{-2} $2.7 \times 10^{+15}$ molecules sec^{-1} $meter^{-2}$
σ	$7.1 \times 10^{+10}$ atoms cm^{-2} $7.1 \times 10^{+14}$ atoms $meter^{-2}$
Order of the reaction	Second
ΔE_p	48.4 kcal $mole^{-1}$ 202. kJ $mole^{-1}$
T_o	1100 K
$\Delta H^{\ddagger}$	46.6 kcal $mole^{-1}$ 195. kJ $mole^{-1}$
$\Delta S^{\ddagger}$	60.6 cal $mole^{-1}$ 254. J $mole^{-1}$
$\Delta G^{\ddagger}$	-20.0 kcal $mole^{-1}$ -83.6 kJ $mole^{-1}$

low surface coverage becomes

$$\left(\frac{dn}{dt}\right)_t = 1.6\,(\sigma_o - \sigma_t)^2 \exp(-23{,}500/T) \text{ molecules meter}^{-2}. \qquad 5.13$$

By using experimental values of $(\sigma_o - \sigma_t)$ and T obtained from the analysis of experiment No. 224-3, the rate of desorption $(dn/dt)_c$ was calculated for various times during the reaction. The calculated values of $(dn/dt)_c$ and the experimental values of $(dn/dt)_t$ are plotted in Fig. 31 as a function of time. Inspection of these two plots reveals that there is a discrepancy between the experimentally determined and calculated values of the desorption rates. This discrepancy could arise from the estimation of the value of k'_{12} in equation 2.30 or from the experimentally determined values of $\Delta S^{\ddagger}$ or $\Delta H^{\ddagger}$.

The average ratio of $(dn/dt)_t$ to $(dn/dt)_c$ was found to be .36. By using this latter ratio as a correction factor, the rate expression for the β_1 oxygen desorption peak now becomes

$$\left(\frac{dn}{dt}\right)_c = 5.7 \times 10^{-1}\,(\sigma_o - \sigma_t)^2 \exp(-23{,}500/T) \text{ molecules meter}^{-2}. \qquad 5.14$$

The results of the analysis of experiment No. 236-1 can be used to determine the β_2 desorption rate expression. This latter expression is given as

$$\left(\frac{dn}{dt}\right)_c = 1.1 \times 10^{+11}\,(\sigma_o - \sigma_t) \exp(-38{,}900/T) \text{ molecules meter}^{-2}. \qquad 5.15$$

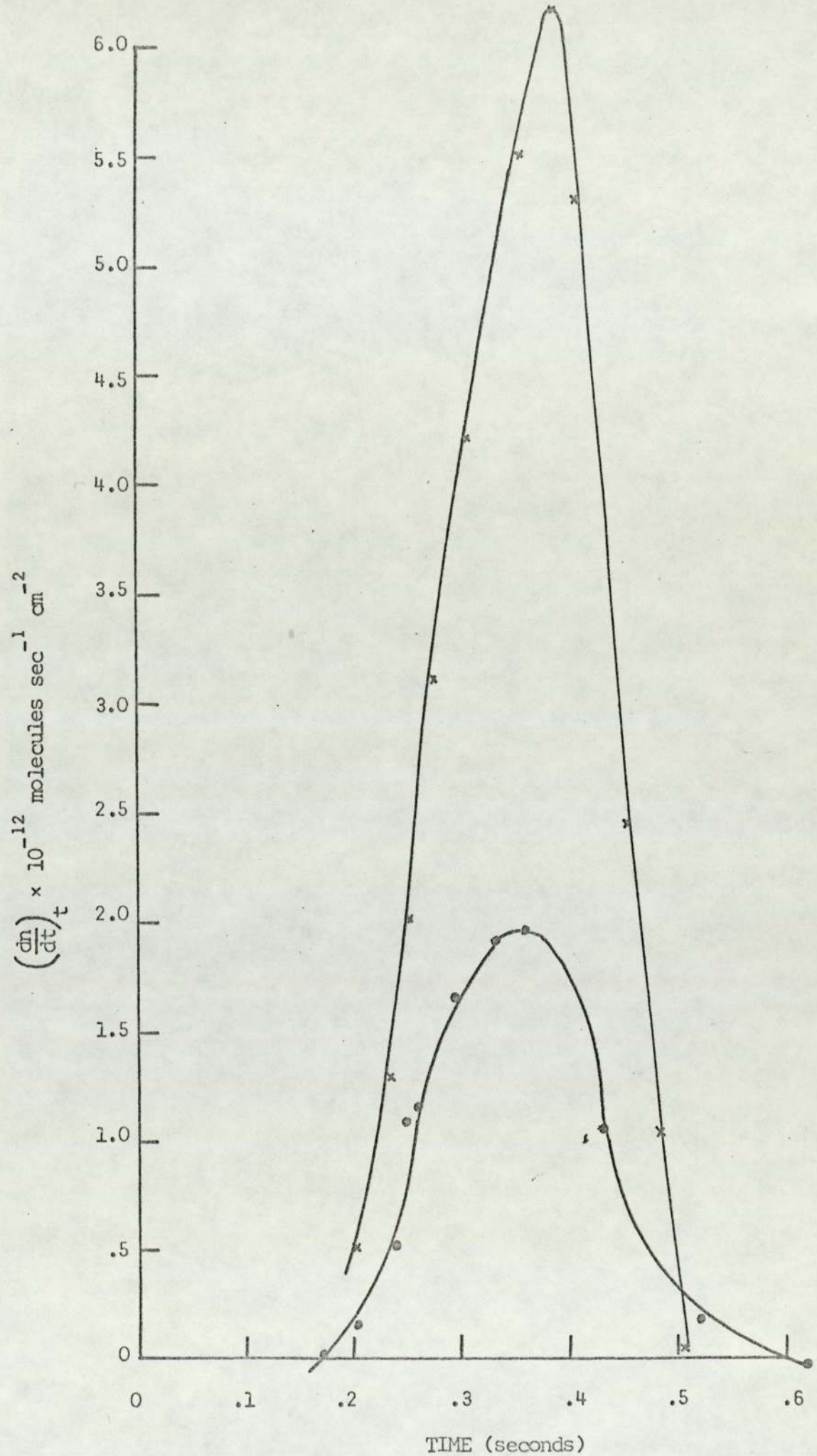

Fig. 31. The rate of desorption as a function of time; calculated × , experimental • .

The calculated and experimental determined desorption ratio are plotted, in Fig. 32, as a function of time. The examination of Fig. 32 shows that the experimental values of the desorption rate exceeds that of the calculated value by a factor of 2. This is not a serious discrepancy when one considers that such an error could arise from a variation of about 3% in the value of $\Delta S^{\ddagger}$.

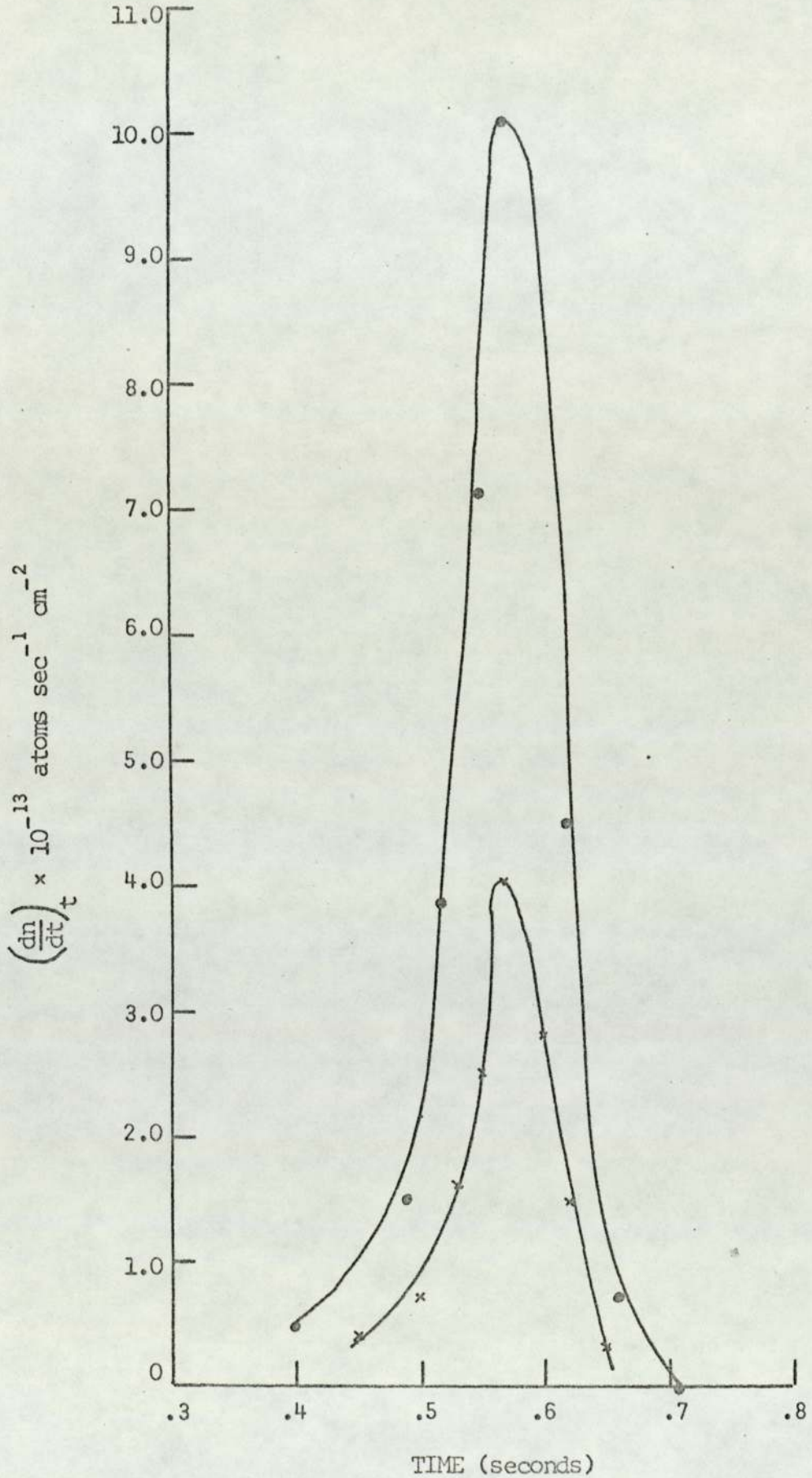

Fig. 32. The rate of desorption as a function of time; calculated × , experimental • .

CHAPTER 6

RESULTS AND DISCUSSION OF THE EFFECTS OF ADSORBED GASES ON THE WORK FUNCTION OF A TANTALUM SURFACE

6.1. Introduction

The electron work function of a polycrystalline surface was determined by the electron beam method described in sections 3.3.4.2. and 5.3. This method determines the work function of a collector surface by the examination of the current-voltage characteristic plot.

The temperature of the emitter surface must be accurately determined in order to determine the work functions of the emitter and the collector filaments. Two methods for the determination of the emitter temperature will be examined and discussed.

The effects of the applied grid voltage on the characteristic plot will be examined. It will be shown that the grid voltage can effect all regions of the characteristic plot.

The electron work function of the polycrystalline tantalum surface will be examined in the presence and absence of adsorbed gases. The interaction of oxygen with the tantalum surface will be considered.

6.2. Collector Current-Voltage Characteristic Plot

A typical collector current-voltage characteristic plot is illustrated in Fig. 33. This characteristic plot was obtained from the experimental cell and its associated electric circuit that are illustrated in Fig. 14 and Fig. 15, respectively. Inspection of Fig. 33 reveals that this characteristic plot has the same three

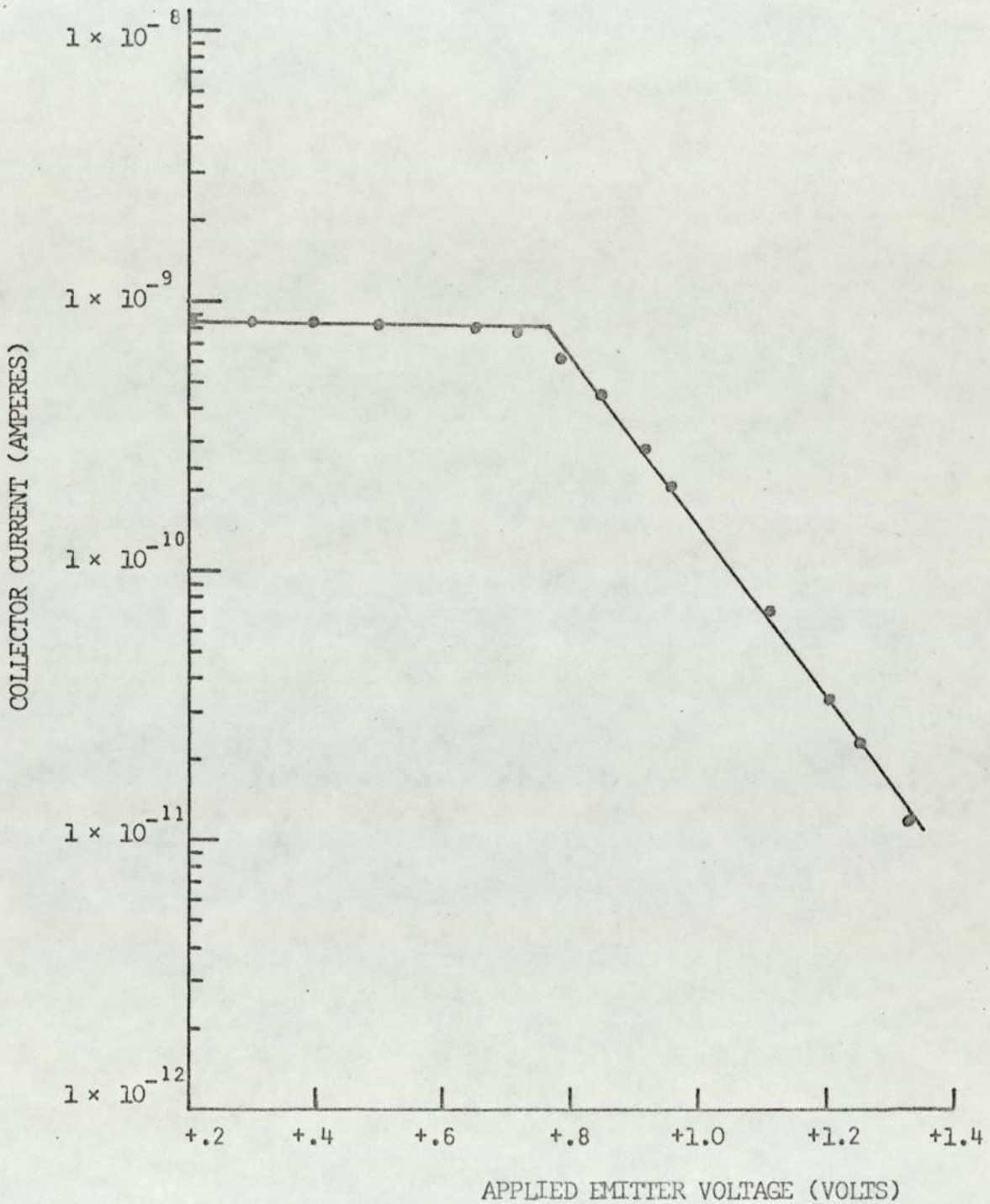

Fig. 33. A typical collector current-voltage characteristic plot.

distinct regions as that of the ideal characteristic plot that was illustrated in Fig. 6. The important features of the experimental plot shown in Fig. 33 are as follows:

1. The saturated region is quite flat.
2. The inflection point or "knee" of the experimental plot is not as sharp as that shown in Fig. 6 or reported by H. Shelton[45]. The tantalum emitter and collector filaments used by H. Shelton[45] were single crystal, while the filaments used in this study were polycrystalline. A polycrystalline surface can be considered as being a patchy surface. Hence, based on the discussion of the effect of patchy surfaces on the work function measurements in section 3.4., the "knee" in Fig. 33 is not expected to be as well defined as that shown in Fig. 6 or reported by H. Shelton[45].
3. From Fig. 33 it can be seen that the collector current density in the retarding portion of the characteristic plot varies exponentially as a function of the applied emitter voltage.

6.3. Emitter Temperature

In using the electron beam method as a means to determine the contact potential difference, the temperature of the electron emitter is an important parameter to consider. The emitter temperature is important because it will effect the collector current-voltage characteristic plot and its numerical values are essential in order to determine the work functions of the emitter and the collector surface.

Consider first of all the saturated current region of the characteristic plot. The magnitude of the collector current density J_2 in this region will be dependent upon the work function and the temperature of the emitter surface. By measuring the saturated current density J_2 and the emitter temperature T_1, the "effective" work function $e\chi_1^{**}$ of the emitter can be determined by solving

$$e\chi_1^{**} = k\,T\ (\ln A - \ln(J_2/T_1^{\,2})) \qquad 6.1$$

where A can be assumed to have a value of 120 amperes cm^{-2} deg^{-2}.

The apparent work function of the emitter can be obtained from

$$e\chi_1^{*} = \frac{-kd\ (\ln(J_2/T_1^{\,2}))}{d(1/T_1)} \qquad 6.2$$

where J_2 is the saturated collector current density for a given value of T_1.

The electron work function of the collector surface can be determined from either equation 3.34 or 3.38. In order to solve either one of these equations, the collector current density must be determined as a function of the emitter temperature.

6.3.1. Energy distribution method

It has been established that electrons emitted from a conductor surface have a Maxwellian energy distribution[30] which is dependent on the surface temperature. Thus, a measurement of the energy distribution of the electrons impinging on the collector surface can be related to the temperature of the emitter surface. This will be true provided the electron energy distribution is representative of that emitted from the emitter filament.

If the above conditions are satisfied, then the emitter temperature can be determined from equation 3.37. Equation 3.37 is rearranged into a logarithmic form and then the $\ln(J_2)$ is differentiated with respect to V_1. The emitter temperature can be determined by solving

$$T_e = \frac{1}{k} \frac{dV_1}{d\ln J_2} \quad . \qquad 6.3$$

6.3.2. Optical method

The temperature of the tantalum emitter was also determined by an optical pyrometer that was supplied by the Leeds and Northrup Company. The optical pyrometer was of the 8630 series and employed the disappearing filament method for measuring the brightness temperature S. The wave length to which this pyrometer responded to was 0.653 microns.

L. Matter and D. B. Langmuir[61] studied the emissivity properties of polycrystalline tantalum supplied by the Fansteel Metallurgical Corporation. These authors used a Leeds and Northrup type K pyrometer that responded to a wave length of 0.652 microns. The relationship between the "true" temperature T_1 and the observed brightness temperature S was found to be

$$T_1 = 0.9915\, S + 37.14 \times 10^{-6}\, S^2 + 5.74 \times 10^{-9}\, S^3 \,. \qquad 6.4$$

The "true" temperature T_1, that are listed in Table XI, were obtained by substituting the observed values for the brightness temperature into equation 6.4.

An inspection of Fig. 14 reveals that during the operation of the planar triode, the position of the magnet prevents optical

Table XI

The observed brightness temperature S and the calculated "true" temperature T_1 for a given filament current I_F

S (K)	T_1 (K)	I_F (amperes)
1073	1115	3.58
1178	1223	4.04
1333	1402	4.85
1370	1443	4.90
1408	1485	5.20
1438	1519	5.55
1548	1650	6.00
1573	1674	6.35
1636	1747	6.95
1703	1826	7.50

temperature measurements of the tantalum emitter filament. G. C. Goode[62] has shown that the filament current is related to the filament temperature. A plot of the "true" temperatures, listed in Table XI, as a function of the square of the filament current I_F is illustrated by Fig. 34. The temperature of the filament T_1 can now be determined from the measured filament current. The filament current was determined by measuring the voltage across a standard resistor.

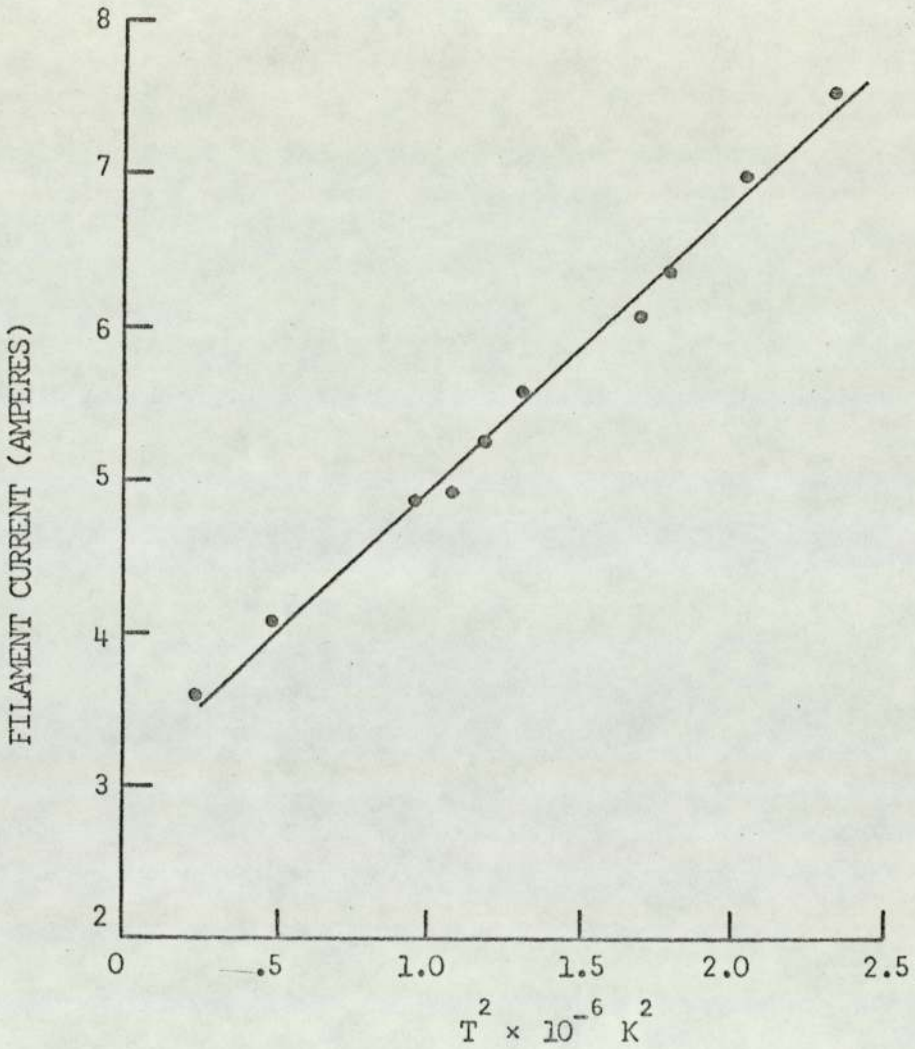

Fig. 34. Filament current as a function of T^2.

6.4. The Effect of the Grid Voltage on the Current-Voltage Characteristic Plot

This section will examine the effect of the grid voltage on the characteristic plot. The applied grid voltage was always positive with respect to the collector filament and the emitter filament. The saturated collector current and the temperature of the emitter, determined by the energy distribution method, will be shown to be dependent on the value of the applied grid voltage.

6.4.1. The effect of the grid voltage on the saturated collector current

The effect of the grid voltage on the current-voltage characteristic plot was determined by measuring the collector current as a function of the applied grid voltage V_g, while maintaining a constant applied emitter voltage V_c and emitter current. The effect of the applied grid voltage V_g on the saturated collector current and on the collector current in the retarding portion of the characteristic plot is illustrated in Fig. 35.

Plot I, in Fig. 35, represents the effect of the applied grid voltage V_g on the saturated current portion of the characteristic plot. This plot was obtained by maintaining the applied emitter voltage at +0.2 volts, with respect to the collector filament and the emitter at an optical temperature of 1635 K. From Fig. 35, it can be seen that at an applied emitter voltage V_c of +0.2 volts, the collector current will be in the saturated current portion of the characteristic plot.

An inspection of plot I, in Fig. 35, reveals that the collector current becomes saturated at an applied grid voltage of 1.0 volt.

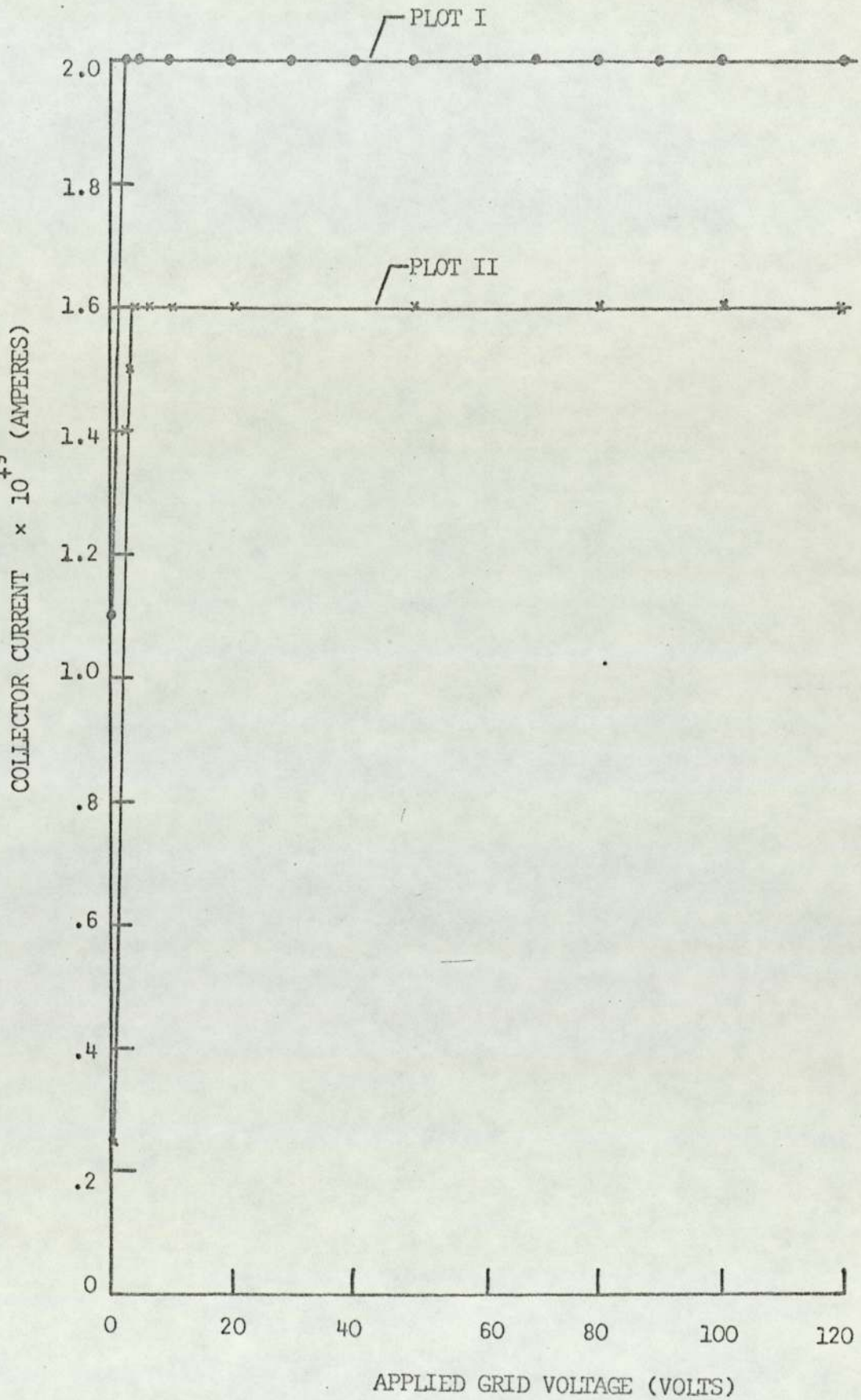

Fig. 35. Collector current as a function of the grid voltage; plot I • ; plot II × .

The collector current remains unaltered for applied grid voltages V_g in the range between +2.0 and +150 volts.

6.4.2. The effect of the grid voltage on the collector current in the retarding portion of the characteristic plot

The collector current as a function of applied voltage in the retarding region of the characteristic plot is illustrated by plot II in Fig. 35. The applied emitter voltage was +0.9 volts, and from an examination of Fig. 35 it can be seen that the collector current will be in the retarding region of the characteristic plot. The emitter temperature, for plot II, was maintained at 1610 K.

An examination of plot II shows that the collector current acquires a maximum value at a grid voltage of +4 volts and remains constant for grid voltages up to +150 volts.

6.4.3. The effect of the grid voltage on the calculated emitter temperature

The effect of the grid voltage on the energy distribution of the electrons was studied by calculating the emitter temperature from a number of current-voltage characteristic plots that were measured at various applied grid voltages. The emitter, during each of the above measurements, was maintained between 1440 K and 1465 K. The calculated values of T_e for various grid voltages are compared with the optically measured emitter temperature T_1 in Table XII.

An inspection of Table XII reveals that the applied grid voltage seriously effects the current-voltage characteristic plot. The effect of the grid voltage on the energy distribution of the electrons can be seen from a comparison of the measured optical temperature T_1 with the calculated emitter temperature T_e. Such a comparison shows that there

Table XII

Calculated emitter temperatures, measured collector current and optically measured emitter temperatures at various applied grid voltages

Saturated collector Current × 10^{+10} (amperes)	Measured optical Temperature T_1 (K)	Calculated emitter Temperature T_e (K)	Grid voltage (volts)
1.6	1440	1540	1.1
1.5	1440	1435	5.0
1.4	1440	1665	10.0
1.5	1465	1570	20.0
1.5	1465	1310	50.0
2.0	1460	-	100.0

is in general poor agreement between the values of T_e and T_1. At grid voltages less than 20 volts, the calculated emitter temperature T_e is generally higher than that of the measured optical temperature T_1. For grid voltages equal or greater than 50 volts, the value of T_e is less than that of T_1.

The changes in the calculated emitter temperature T_e, and hence the energy distribution of the electrons, are a result of changes in the current-voltage characteristic plot due to the variation in the applied grid voltage. For grid voltages up to 20 volts, the characteristic plot is similar to that illustrated in Fig. 33. The effect of the applied grid voltages equal or greater than 50 volts is shown in Fig. 36. In this latter figure, the grid voltage was 100 volts. A comparison of the characteristic plots illustrated in Fig. 33 and Fig. 36 shows that an increase in the grid voltage has a marked influence on the sharpness of the inflection point and the collector current dependency on the applied emitter voltage V_c in the retarding region of the characteristic plot. The inflection point or the "knee" of the characteristic plot in Fig. 36 is so ill-defined that a determination of the contact potential difference is extremely difficult. From an examination of the collector current as a function of applied emitter voltage V_c in Fig. 36, the energy distribution of the electrons does not appear to be Maxwellian.

In view of the results of the effect of the grid voltage on the current-voltage characteristic plot, the grid should not exceed 20 volts, nor can the calculated emitter temperature T_e be taken as representing the actual emitter temperature.

In order to explain the effect of the grid voltage on the current-voltage characteristic, consider the effect that a beam of

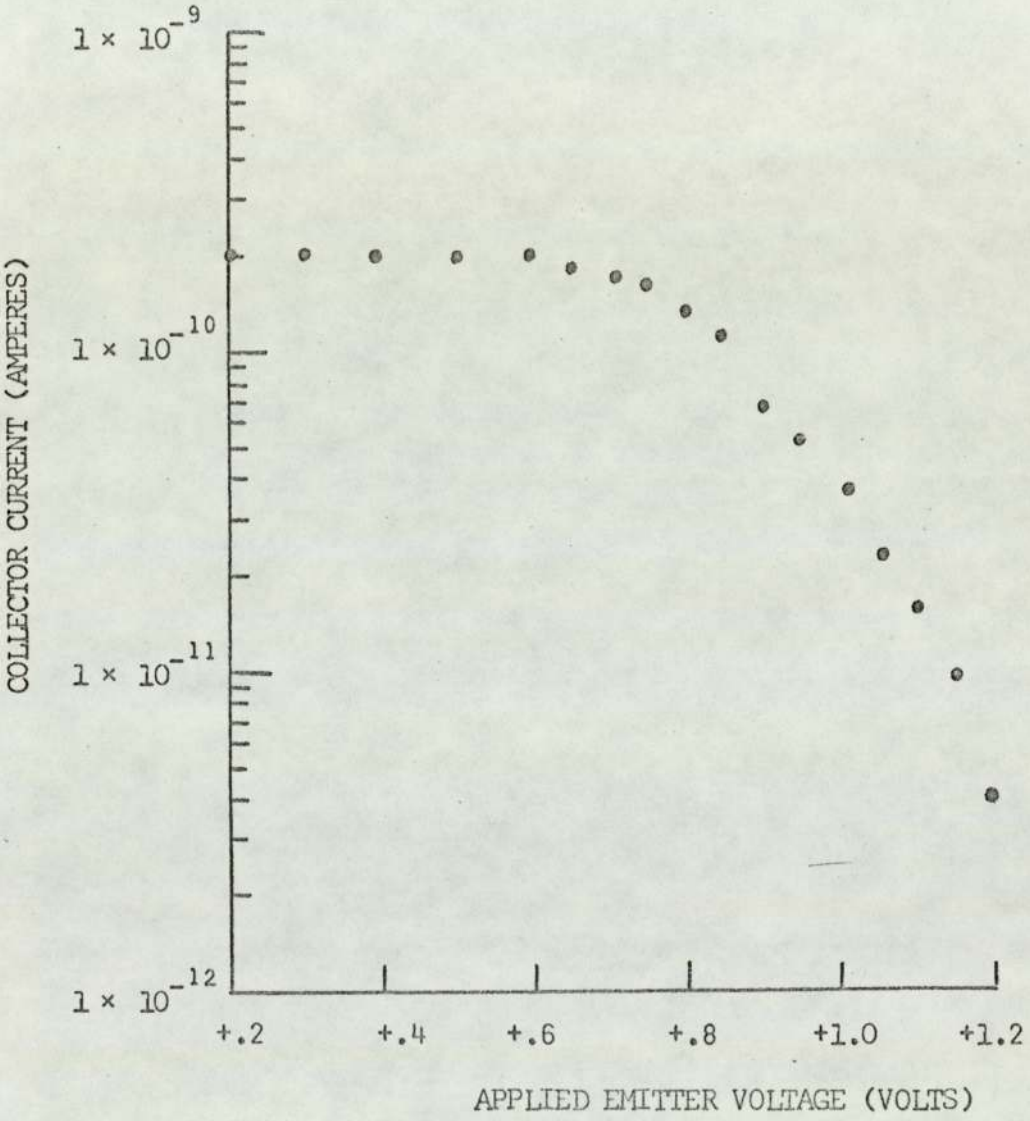

Fig. 36. The effect of an applied grid voltage of 100 volts on the current-voltage characteristic plot.

primary electron will have if they are permitted to strike the walls of the grid aperture. These electrons could either be captured by the grid or suffer elastic or inelastic scattering. For primary electrons that suffer elastic scattering, there will exist a probability that electrons on the metal surface may acquire sufficient energy to be emitted with energies up to 3 eV[63]. These latter electrons are known as secondary electrons and the process by which they are generated is generally referred to as secondary electron emission[63].

The secondary electron emission coefficient δ[63] is defined as the ratio of the number of secondary electrons emitted to the number of primary electrons that incident the metal surface. The value of δ is not particularly affected by temperature, but is dependent on the energy of the primary electrons. The coefficient δ will increase with an increase in the primary electron energy up to a maximum value, whereupon a further increase in the energy of the primary electrons will result in a decrease of δ. The onset of the secondary electron emission can occur at primary electron energies as low as 10 volts.

The secondary emission coefficient δ is also dependent on the angle of incident of the primary electrons. The coefficient δ will increase as the angle of incident decreases.

From the above discussion, it can be seen that the secondary electron emission current could alter the current-voltage characteristic plot in the following manner.

1. The secondary electron current will increase the magnitude of the saturated collector current.
2. The secondary electrons can have energies up to about 3 volts. A secondary emission current would not only alter the magnitude of the total current but also effect the energy distribution of the electrons striking the collector surface.

Based on the above criterion for the effect of a secondary emission current on the characteristic plot, the results of the characteristic plots listed in Table XII and the characteristic plot illustrated in Fig. 36 indicate that the effect of the grid voltage is due to an increase in the secondary emission current. The secondary emission current is quite significant for a grid voltage of 100 volts. The saturated collector current, at the latter voltage, was increased from 1.5×10^{-10} amperes to 2.0×10^{-10} amperes. Even at low grid voltages, it appears that the secondary emission current is significant enough that electrons, because of the restriction in their motion by the presence of the magnetic field, will strike the surface of the grid aperture at a low angle. This low angle of incident for electrons having energies less than 10 eV could result in elastic scattering wihhout electron emission. Such a condition would not alter the total electron current but effect the energy distribution of the electrons.

An important parameter to consider is the fraction of electrons f_c that pass through the aperture that would be involved in collisions with the walls. The fraction of electrons f_c involved in collision with the walls is proportional to the ratio of the surface area and the cross sectional area of the aperture. Thus f_c can be expressed as

$$f_c \propto \frac{2\, t_w}{r} \qquad 6.5$$

where t_w is the thickness of the grid and r is the radius of the grid aperture. From equation 6.5 it becomes apparent that one can expect that fraction of electrons involved in wall collisions will increase as the grid thickness is increased and the radius of the aperture is decreased. The value of $\frac{2\, t_w}{r}$ for the experimental reaction cell illustrated in Fig. 14 was calculated to be .21.

At first glance the results of this section appear to be in conflict with the results plotted in Fig. 35. This is, however, not the case. The collector currents in plot I and II were on order of magnitude greater than those of this section and hence the effect of the secondary emission current on the total collector current was not as apparent.

6.5. Determination of the Electron Work Function of the Emitter and Collector Surfaces from the Current-Voltage Characteristic Plot

In this section the "effective" and the "apparent" work function of the emitter and collector surfaces will be determined from a family of characteristic plots. The measured optical temperature T_1 of the emitter will be used to represent the emitter temperature. The calculated emitter temperature T_e will also be listed in the tables of results so that a comparison of the two methods of temperature measurement can be obtained. The "apparent" work function of the emitter and the "apparent" work function of the collector surface will be obtained by solving equation 6.2 and 3.46, respectively.

6.5.1. Emitter "effective" work function

The "effective" emitter work functions for a number of emitter temperatures were obtained from the family of characteristic plots illustrated in Fig. 37. These characteristic plots were all measured at a grid voltage of 5 volts. The calculated "effective" work functions for various emitter temperatures are listed in Table XIII.

From Table XIII can be seen that once again there is poor agreement between the measured optical temperature T_1 and the calculated emitter temperature T_e.

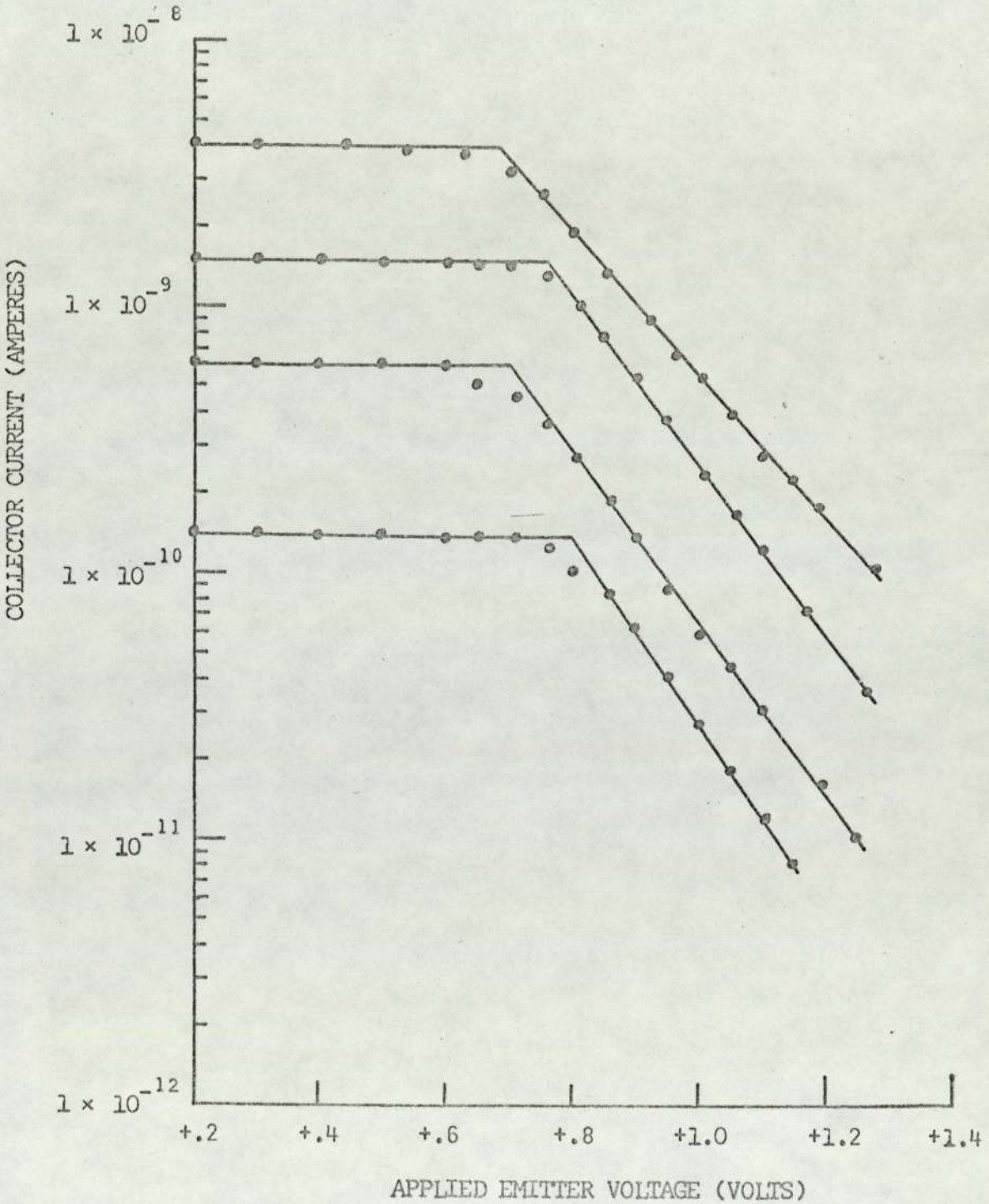

Fig. 37. Family of current-voltage characteristic plots.

Table XIII

The effective emitter work function for various emitter temperatures obtained from the characteristic plots of experiment No. 207

"Effective" emitter work function $e\chi_1^{**}$		Optical emitter temperature T_1	Calculated emitter temperature
(eV)	(kJ mole^{-1})	(K)	(K)
4.96	475.	1545	1434
4.92	471.	1590	1561
4.97	479.	1640	1585
5.06	484.	1715	1862

$$e\chi_1^{**} = 4.98 \pm (\text{P.E.})\ .02 \text{ eV}$$

P.E. = Probable Error

$$e\chi_1^{**} = 477 \pm (\text{P.E.})\ 2 \text{ kJ mole}^{-1}$$

6.5.2. The collector "effective" work function

The collector work function for a patchy surface can be defined from equation 3.44 as

$$e\bar{\chi}_2 = e\bar{\chi}_1 - \bar{V}_{12} \ . \qquad 6.6$$

If $e\chi_1$ is set equal to the "effective" work function of the emitter $e\bar{\chi}_1^{**}$, then the "effective" work function of the collector $e\bar{\chi}_2^{**}$ can be defined as

$$e\bar{\chi}_2^{**} = e\bar{\chi}_1^{**} - \bar{V}_{12} \ . \qquad 6.7$$

The term $-\bar{V}_{12}$ was defined, by equation 3.45, as being equal to V_1.

V_1 represents the voltage at the inflection point in the characteristic plot and is determined, as shown in Fig. 37, as the point of intersection of a pair lines drawn through the saturation current region and the retarding region of the current voltage characteristic plot. The contact potential difference V_{12} and the "effective" emitter work function $e\bar{\chi}_1^{**}$, that were used to determine the "effective" collector work function $e\bar{\chi}_2^{**}$, were obtained from the family of characteristic plots illustrated in Fig. 37 and Table XIII, respectively. The calculated values of $e\bar{\chi}_2^{**}$ are tabulated in Table XIV.

Table XIV

The "effective" collector work function and contact potentials obtained from the characteristic plots of experiment No. 207

Effective collector work function $e\bar{\chi}_2^{**}$		Contact potential $\bar{V}_{12}$	Optical emitter temperature T_1
(eV)	(kJ mole^{-1})	(Volts)	(K)
5.76	551.	-.795	1545
5.62	548.	-.700	1590
5.83	567.	-.865	1640
5.74	550.	-.680	1715

$e\bar{\chi}_2^{**} = 5.74 \pm$ (P.E.) .03 eV

P.E. = Probable Error

$e\bar{\chi}_2^{**} = 550 \pm$ (P.E.) 3 kJ mole^{-1}

A comparison of the collector "effective" work functions of the emitter that are listed in Table XIII indicates that the collector

work function is greater than that of the emitter work function. This effect can be explained by the fact that the gases adsorbed on the collector surface were not thermally desorbed prior to the taking of the characteristic plots. It is then the presence of adsorbed gases species on the surface that are responsible for the high "effective" work functions of the collector.

6.5.3. The "apparent" work function of the emitter

The "apparent" work function of the emitter was determined by solving equation 6.2. The value of J_2 was obtained from the saturation currents of the characteristic plots. The term $d(\ln J_2/(T_1^2))/(1/T_1)$ was obtained from the slope of the plot that is illustrated in Fig. 38. The "apparent" work function was calculated to be 4.85 eV or 465 kJ $mole^{-1}$. The pre-exponential term was determined as 43 amperes cm^{-2} deg^{-2} or $4.3 \times 10^{+7}$ amperes $meter^{-2}$ deg^{-2}. A comparison of the average "effective" work function $e\chi_1^{**}$ with the "apparent" work function $e\chi_1^{*}$ shows that the obtained values are in agreement. The scatter in the experimental data has a greater effect on the calculated value of the "apparent" work function than on the average "effective" work function.

6.5.4. The "apparent" work function of the collector

The "apparent" work function of the collector was determined by solving equation 3.34. This equation was solved by the analytical method that was outlined in section 3.3.4.2. The plot of $\left[\ln(J_2/T_1^2)-\bar{V}_{12}(T)\right]$ as a function of $(1/T_1)$ is shown in Fig. 39. The "apparent" work function of the collector $e\chi_2^{-*}$ was calculated to be 4.96 eV and is not in agreement with the "effective" work function of 5.74 eV.

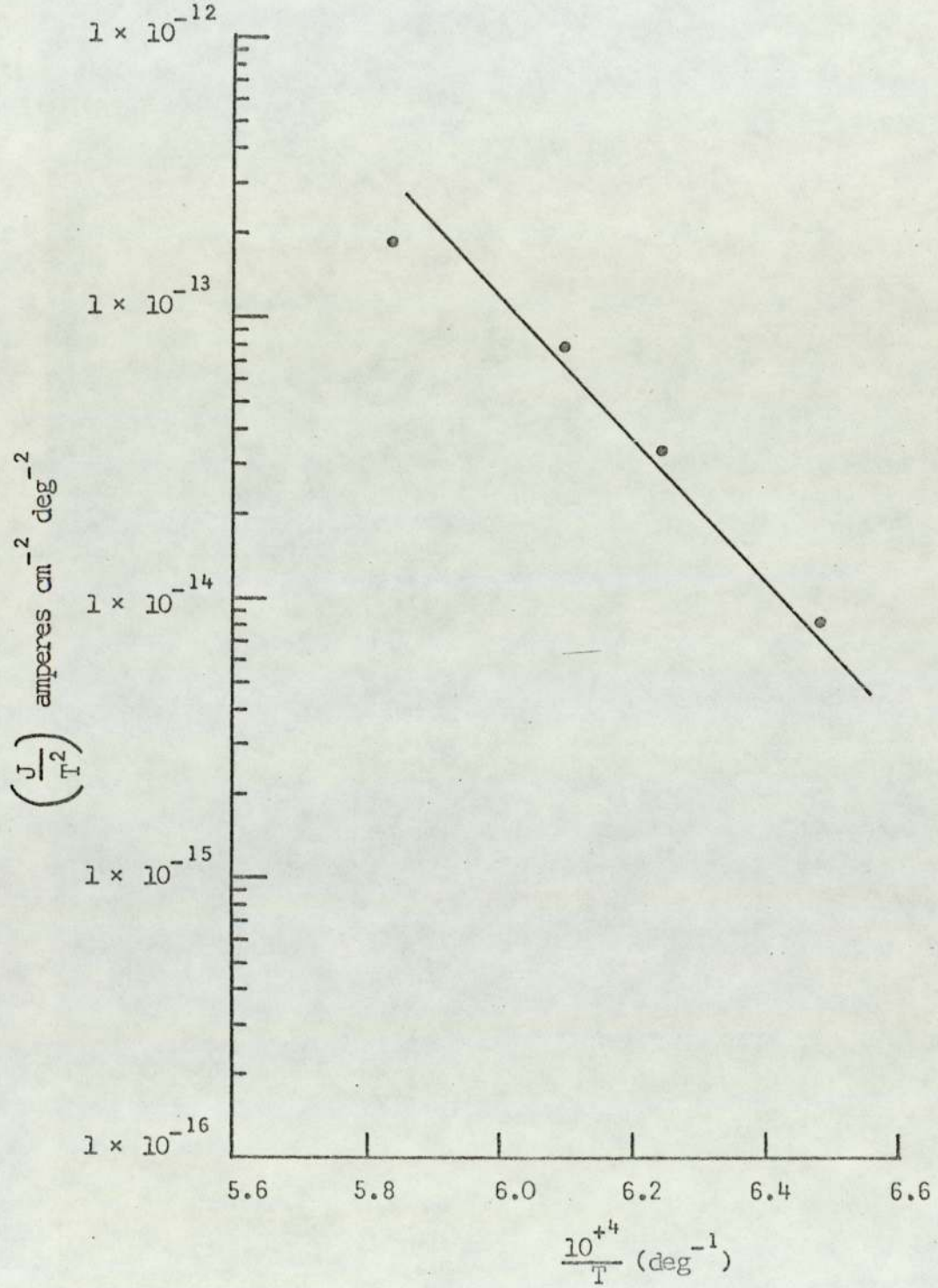

Fig. 38. The $\ln(J_2/T_1^2)$ as a function of (1/T).

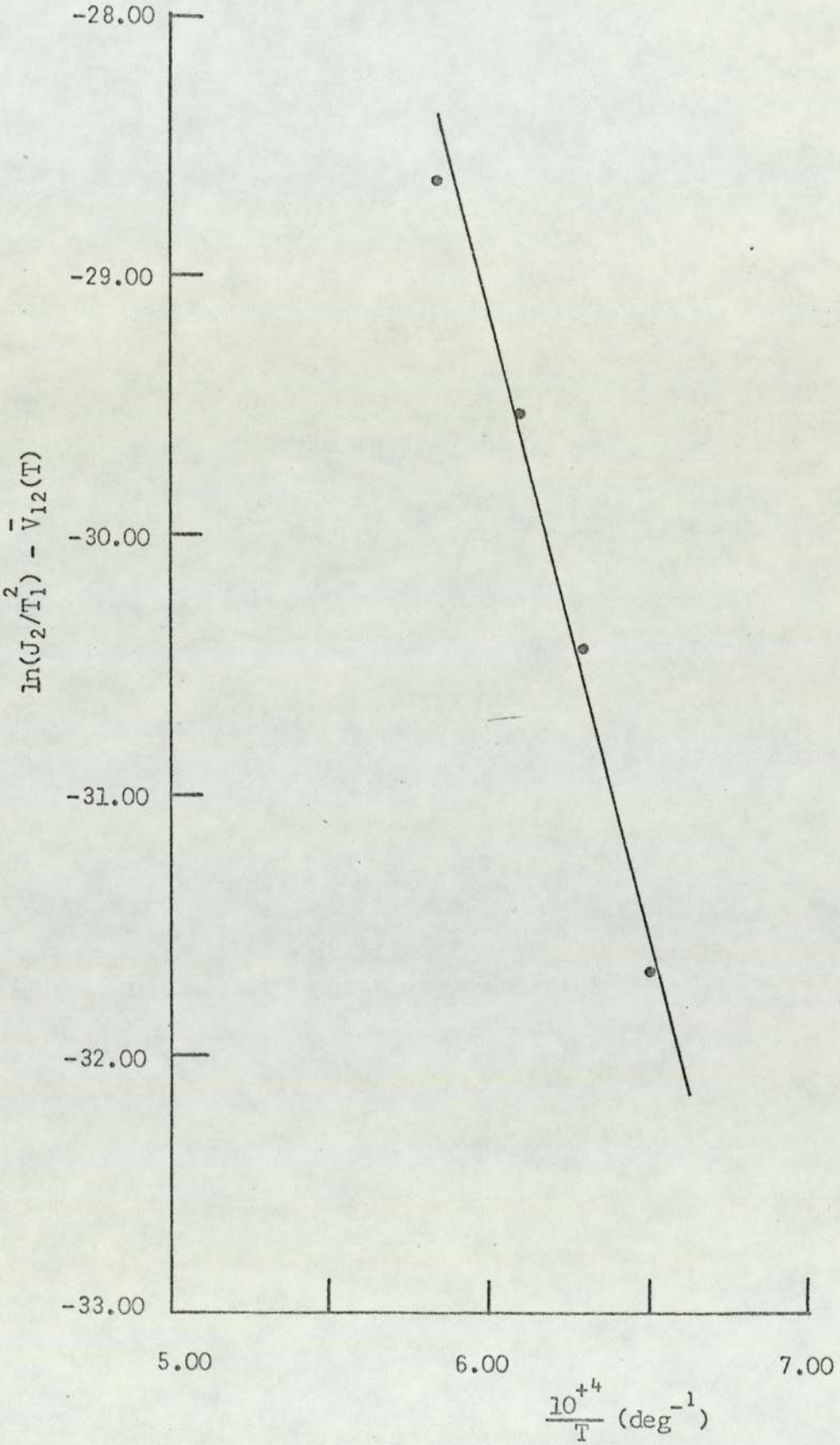

Fig. 39. $(\ln(J_2/T_1^2) - \bar{V}_{12}(T))$ as a function of $(1/T_1)$.

The discrepancy between the values of $e\bar{\chi}_2^{*}$ and $e\bar{\chi}_2^{**}$ stems from the fact that in equation 3.46 the temperature dependence of the contact potential $\bar{V}_{12}$ is negligible when compared to the temperature dependence of the saturated collector current J_2. Hence, by using an average value of the contact potential $\bar{V}_{12}^{a}$, the "apparent" work function of the collector is now expressed as

$$e\bar{\chi}_2^{*} = -k \frac{d(\ln(J_2/T_1^2))}{d(1/T_1)} - \bar{V}_{12}^{a} \qquad 6.8$$

or

$$e\bar{\chi}_2^{*} = e\bar{\chi}_1^{*} - \bar{V}_{12}^{a} \qquad 6.9$$

The average value of the contact potential $\bar{V}_{12}^{a}$ was found to be -.760 volts and from equation 6.9 the "apparent" work function of the collector $e\bar{\chi}_2^{*}$ was calculated to be 5.61 eV or 537 kJ mole^{-1}. The "apparent" work function of the collector $e\bar{\chi}_2^{*}$ determined by solving equation 6.9 is now in agreement with the effective work function $e\bar{\chi}_2^{**}$.

6.5.5. The "effective" and "apparent" work function for a thermally cleaned collector surface

In this experiment the collector surface was first heated to about 2000 K for five seconds. The collector filament was cooled and allowed to remain at the ambient cell temperature for a period of one hour prior to measurement of the characteristic plots.

The values of the "effective" work function for the collector and emitter filaments are tabulated in Table XV.

The "apparent" work function of the emitter was calculated to be 4.91 eV or 470 kJ mole^{-1}. The value of $\bar{V}_{12}^{a}$ was found to be -.475 eV, and by solving equation 6.9, the "effective" work function of the collector was found to be 5.39 eV or 516 kJ mole^{1}.

Table XV

Results of the "effective" work function determined with a thermally cleaned collector surface

Effective emitter work function $e\chi_1^{**}$		Effective collector work function $e\chi_2^{**}$		Contact potential $\bar{V}_{12}$	Optical Temperature	Calculated Temperature
(eV)	(kJ mole^{-1})	(eV)	(kJ mole^{-1})	(Volts)	(K)	(K)
4.91	470	5.37	515	-.462	1520	1426
4.90	469	5.32	509	-.415	1580	1487
4.98	477	5.44	520	-.465	1620	1709
4.93	472	5.49	525	-.560	1685	1956

$\bar{e\chi}_1^{**}$ = 4.93 $\pm$ (P.E.) .01 eV

$\bar{e\chi}_1^{**}$ = 472 $\pm$ (P.E.) 1 kJ mol^{-1}

$\bar{e\chi}_2^{**}$ = 5.40 $\pm$ (P.E.) .03 eV

$\bar{e\chi}_2^{**}$ = 517 $\pm$ (P.E.) 3 kJ mol^{-1}

P.E. = Probable Error

A comparison of the effective work functions listed in Table XV and those in Table XII show that calculated emitter work functions are in excellent agreement. The effect of thermally desorbing gases from the collector surface can be seen by the apparent decrease in the "effective" and the "apparent" work function of the collector.

The fact that the electron work function of the emitter is less than that of the collector indicates that adsorbed gas species were still present on the collector surface.

6.5.6. The interaction of oxygen with a tantalum surface

In this experiment, No. 233, the collector was first cleaned at a pressure of about 6×10^{-9} torr by thermally desorbing the gases from the surface. This was accomplished by flashing the collector a number of times to a temperature greater than 2200 K. The flashing of the collector was continued until the pressure increase in the system during the flash was consistent. The collector was allowed to remain for ten minutes at ambient cell temperature and then the "effective" collector work function was determined.

An analysis of the characteristic plot indicated that the contact potential difference was now +.120 volts. With the effective work function of the emitter at 4.95 eV, the collector work function was determined as 4.83 eV or 464 kJ $mole^{-1}$. This work function value for polycrystalline tantalum is in good agreement with that reported by E. Ya. Zandberg and A. Ya. Tongegode[64]. These latter investigators determine the electron work function by observing the surface ionization of indium and found the work function for polycrystalline tantalum to be 4.88 eV or 467 kJ mol^{-1}. Other investigators[65-66], by employing other experimental techniques, have reported work function values that range from 4.10 eV to 4.33 eV.

The collector was flashed again to a temperature greater than 2200 K and the thermal desorption spectrum is illustrated by Fig. 40. This desorption spectrum shows that there was some contamination of the collector surface from the walls of the reaction cell as a result of making the work function determination. The contamination of the collector surface illustrated in Fig. 40 is not as acute as that shown in Fig. 21.

The pressure of the system was then increased to 6×10^{-8} torr by admitting oxygen into the system by means of the variable leak valve V_3. After one hour, the pressure of the system was reduced to original value by the closing of the valve V_3.

A current-voltage characteristic plot was taken and the contact potential difference was determined to be .295 volts. The electron work function was then calculated to be 4.65 eV or 455 kJ mol^{-1}.

The gases adsorbed on the collector surface were then thermally desorbed and the desorption spectrum is illustrated by Fig. 41. From the thermal desorption spectrum, the surface coverage was determined by the same method as that used in section 5.4.2. The total surface coverage, i.e., the sum of the atoms adsorbed in both the β_1 and β_2 states, was determined as $2.4 \times 10^{+13}$ atoms cm^{-2} or $2.4 \times 10^{+17}$ atoms $meters^{-2}$.

The dipole moment of the adsorbed gas species can be defined as

$$\alpha_d = \frac{\Delta(e\chi_2^{**})}{4\pi\,\sigma_o} \qquad 6.10$$

where $\Delta(e\chi_2^{**})$ is the change in work function as a result of the adsorption of oxygen on the collector surface. The value of $\Delta(e\chi_2^{**})$ was found to be .18 eV or 17 kJ mol^{-1}. The calculated dipole moment per atom was determined as 2.0 Debye. The sign of the dipole moment

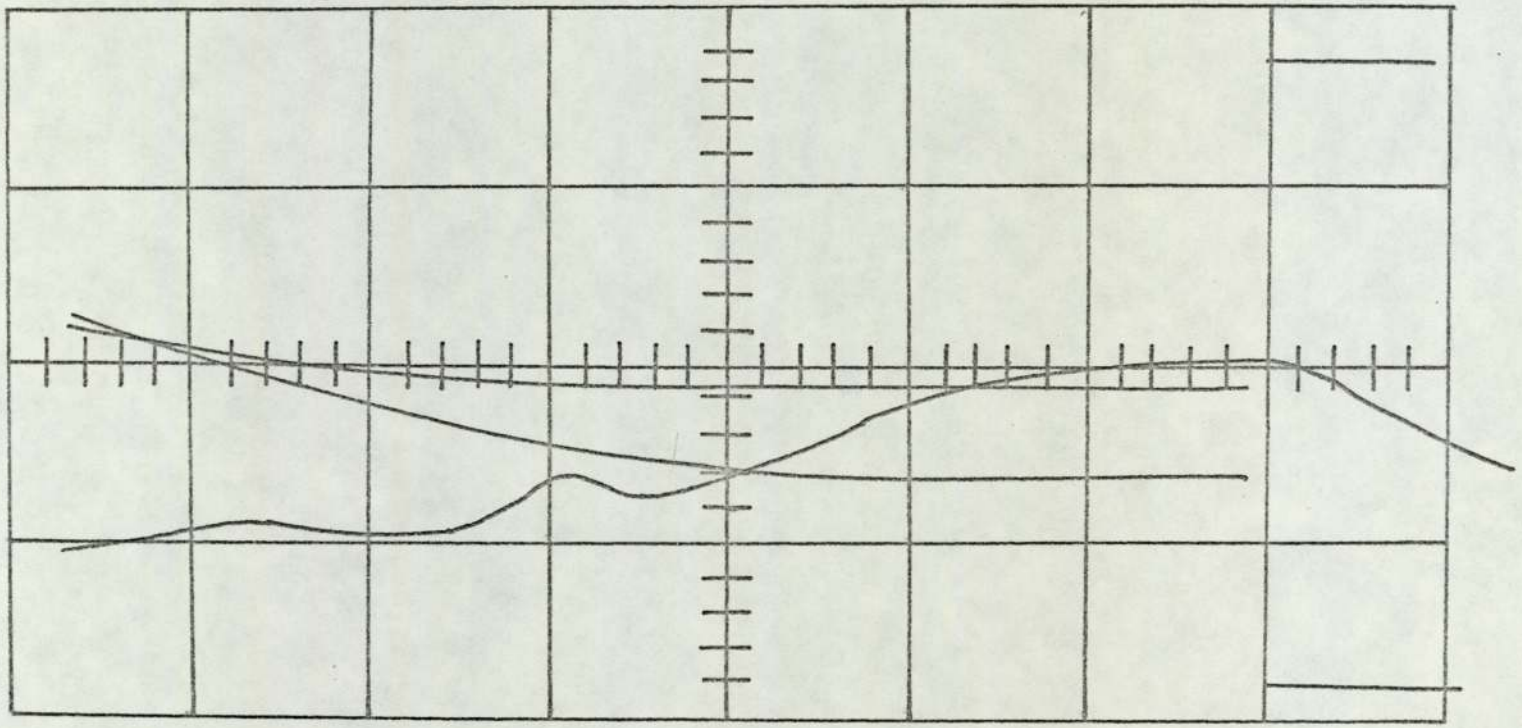

Fig. 40. Thermal desorption spectrum showing the contamination of the collector surface due to desorption from the walls of the experimental cell.

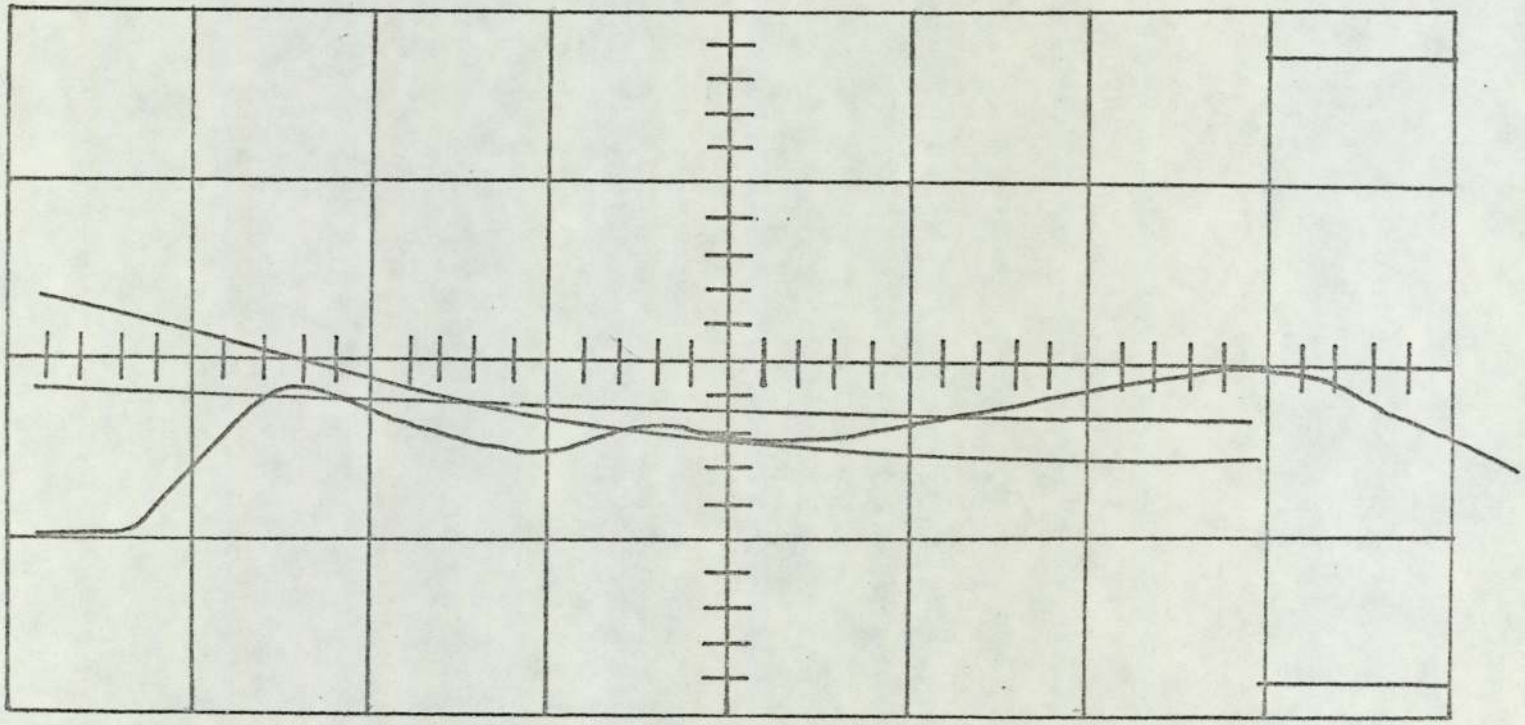

Fig. 41. Thermal desorption of oxygen after one hour at a pressure of 6×10^{-6} torr.

indicates that the charge located on the adsorbed oxygen atom was positive. Other investigators studying the effects of oxygen on the electron work function on tungsten[67] have also reported a decrease in the electron work function at low coverage followed by an increase in the work function.

In section 6.5.2., the effective work function of a tantalum surface in the presence of adsorbed gases was determined as 5.74 eV. If it is assumed that a monolayer of gas is present or $1 \times 10^{+15}$ atoms cm^{-2}, then by solving equation 6.10 the average dipole moment of these adsorbed gases would be -.24 Debye.

In this experiment, the partial pressure of oxygen was increased to 6×10^{-8} torr for one hour. From the kinetic theory of gases, the rate at which gas molecules impinging a surface is given as

$$v = 3.5 \times 10^{+22} \frac{P \text{ (torr)}}{(MT)^{\frac{1}{2}}} \text{ molecules } cm^{-2} \text{ sec}^{-1} \qquad 6.11$$

At a pressure of 6×10^{-8} torr, oxygen molecules will make $8 \times 10^{+11}$ collisions cm^{-2} sec^{-1} or $8 \times 10^{+15}$ collisions $meter^{-2}$ sec^{-1}. The total number of molecules that were desorbed was calculated to be $1.2 \times 10^{+13}$ cm^{-2}. Hence, the sticking coefficient[68] for oxygen on tantalum would be 2×10^{-4}. This value is lower than one would normally expect and would indicate that a proportion of the adsorbed oxygen is desorbed in the form of tantalum oxides $Ta_x O_y$.

CHAPTER 7

SUMMARY AND CONCLUSION

7.1. Experimental Apparatus

A bakable oil free vacuum system was used. This system, after baking at a temperature of 250°C for at least four hours, was shown to be capable of obtaining pressures in the 10^{-11} torr range without the use of an ion pump. The pressure was obtained after careful purging of the entire vacuum system and sorption pumps with boiled-off nitrogen. The purging was needed to remove gases that are not readily adsorbed by either the sorption pumps or the sublimation pump. A single sorption pump was shown to be capable of reducing the pressure of three litre pyrex vessel from one atmosphere to 5×10^{-6} torr and thus represents a significant improvement over the sorption pumps described by J. O. Cope[54].

The reaction cell was a planar triode with a collector filament that could be used in the study of thermal desorption reactions. The planar triode was constructed in a manner similar to that reported by H. Shelton[45]. The collector and emitter filaments were constructed from the same sheet of polycrystalline tantalum.

The thermal desorption spectrum was displayed on a Tektronic Oscilloscope, type 545, with a N_1 four trace pre-amplifier. The oscilloscope traces were recorded on 35 mm Ilford film.

The oxygen sample was prepared in an oil free vacuum system by the thermal decomposition of solid potassium permanganate.

7.2. Thermal Desorption of Oxygen from a Polycrystalline Tantalum Surface

The study of the thermal desorption reaction of oxygen from a tantalum surface has shown that it is possible to make a complete kinetic study of a thermal desorption reaction in a flow system. This was made possible by the determination of the pumping speed from the oscilloscope display.

The temperature of the collector filament at any instant during the desorption reaction was obtained by determining the resistivity of the tantalum collector. The resistances in the filament circuit because of the copper leads and stainless steel supports were shown to be constant during the thermal desorption reaction. The contact resistances were assumed to be constant during the reaction. A change in the resistance of the filament circuit was associated with a change in the resistivity of the tantalum collector. From a knowledge of the temperature dependence of the resistivity of tantalum[59], the temperature of the filament could be determined as a function of time.

The rate of evolution of gas from a surface at a time t was expressed as

$$\left(\frac{dn}{dt}\right)_t = \left(\frac{dn}{dt}\right)_{t_m} \left[\frac{V}{S_E P_{t_m}} \left(\frac{dP^*}{dt}\right)_t + \frac{P^*_t}{P^*_{t_m}} \right] \qquad 2.38$$

where $\left(\frac{dn}{dt}\right)_{t_m}$ was the rate of desorption at the time t_m when P^* approach its maximum value.

The initial surface coverage σ_o was obtained by solving equation 2.39 by graphical means. The surface coverage at a time t was defined by equation 2.40.

The experimental activation energy for a thermal desorption reaction of the nth order was defined as

$$\Delta E_p = R \; d \left[\ln \frac{(dn/dt)_t}{(\sigma_o - \sigma)^{n'} T} \right] \Big/ d(1/T) \qquad 2.41$$

The standard heat of activation $\Delta H^{\ddagger}$ was determined by correcting the experimental activation energy by means of equation 2.33. In order to obtain the standard heat of activation it was necessary to define a standard state for the desorption reaction. Such a state was defined as that surface coverage when the free energy was independent of surface coverage. The standard state was taken at a low surface coverage.

The change in entropy for the activation reaction was determined from the experimental activation energy and the collector filament temperature, the rate of gas evolution, and the temperature of surface at the standard state. The change in entropy was given as

$$\Delta S^{\ddagger} = R \left[\ln \left(\frac{dA}{dt} \right)_{T=T_o} - \ln \left(k'_{n'} (A)^{n'} - 1 \right) \right] + \frac{\Delta E_p}{T_o} \qquad 2.30$$

where n' is the order of the reaction. The constant k^1_{11} had the units of sec^{-1} and an assumed value of 1, whereas, the value of k^1_{12} was given as 1×10^{-15} and had the units of $sec^{-1}\ cm^{-2}\ molecule^{-1}$.

The thermal desorption spectrum showed that gases on the tantalum surface were adsorbed in two states, i.e., β_1 and β_2. Analysis of the β_1 desorption peak indicated that the desorption reaction rate equation could be expressed in terms of the free energy of the reaction as

$$\left(\frac{dn}{dt}\right)_c = 5.7 \times 10^{-1} \quad (\sigma_o - \sigma_t)^2 \exp(-23{,}500/T) \text{ molecules meter}^{-2} \qquad 5.13$$

The analysis of the β_2 desorption peak showed that this was a first order reaction and the reaction rate equation was

$$\left(\frac{dn}{dt}\right)_c = 1.1 \times 10^{+11} \quad (\sigma_o - \sigma_t) \quad \exp(-38{,}900/T) \text{ molecules meter}^{-2} \qquad 5.15$$

The β_1 peak was shown to be the result of the desorption of oxygen. The β_2 was associated with gases desorbed from the walls of the sublimation pump. It was also shown that contamination of the collector surface could result from the desorption of gases from the walls of the reaction cell.

7.3. The Effect of Adsorbed Gases on the Electron Work Function of a Polycrystalline Tantalum Surface

The electron beam method was used for determining the electron work function of a collector surface. This method of determining the electron work function was selected because of its simplicity in design and because it did not require the temperature of the collector surface to be altered. With this method, the work function of the collector and emitter surfaces could be obtained from the measured current-voltage characteristic plot.

The form of the characteristic plot was shown to be dependent on the applied grid voltage. At a grid voltage greater than 10 volts, the magnitude of the saturated current, the definition of the inflection point, and the energy distribution of the electrons were effected. This affect of the grid voltage on the characteristic plot was explained in terms of the secondary electron emission from the grid surface.

The calculated "effective" and "apparent" work functions of the emitter were found to be in agreement. The "effective" work function was determined from the saturated current of the characteristic plots and has a value of 4.93 eV or 472 kJ mol^{-1}. This high value of the work function of the emitter was attributed to the presence of adsorbed gas species.

The "effective" and "apparent" work functions of the collector surface were measured in the presence and absence of adsorbed gases. With adsorbed gases present on the colllector surface, the "effective" work function was determined to be 5.74 eV or 550 kJ mol^{-1}. It was shown that the "apparent" work function could not be determined by solving equation 3.38 because, when compared to the collector current, the temperature dependence of the contact potential difference was insignificant. The "apparent" work function of the collector was determined by solving equation 6.4 and its value was calculated to be 5.61 eV or 537 kJ mol^{-1}.

For a clean surface, the "effective" work function of the collector was calculated to be 4.93 eV or 464 kJ mol^{-1}. When oxygen was adsorbed on the surface, the work function decreased to 4.65 eV or 445 kJ mol^{-1}. The dipole moment of adsorbed gases on the surface at this surface coverage was calculated to be +2.0 Debeys. The dipole moment of gases adsorbed at high coverage was estimated to be -.24 Debeys.

From the low calculated value of the sticking coefficient, some of the oxygen adsorbed on the surface must have been desorbed in the form of tantalum oxides.

7.4. Use of the Planar Triode by Other Investigators

Others investigators[45, 49, 69] have used the planar triode as a means to determine the work function of a collector surface and to study the effects of gas adsorption on the work function of a metal surface. The experimental techniques and the method of analysis of the experimental data used by the latter investigators differs from that which has been presented in this thesis. Because of these differences, it is fitting that a comparison be made between these experimental techniques and methods of analysis.

H. Shelton[45] and A. E. Abey[49] determined the work function of metal surfaces by means of the planar triode. The current-voltage characteristic plots, that were obtained at grid voltages exceeding 100 volts, were nearly ideal. The emitter temperatures were determined by means of equation 6.3. The range of emitter temperatures used by H. Shelton[45] to obtain the family of characteristic plots was 400 K, whereas the emitter temperature range used by A. E. Abey[49] was 200 K. Neither of these investigators showed that there was any correlation between the calculated temperatures and those obtained by other means such as an optical pyrometer. Such a correlation is necessary to justify the reporting the emitter temperature to .1 K[49].

The effect of the grid voltage on the characteristic plot for the planar triode used in these experiments showed that no confidence could be placed in the validity of the calculated emitter filament temperature. At a grid voltage of 100 volts, the effect of a

secondary emission current was pronounced in all regions of the current-voltage characteristic plot. The emitter temperature range used in this work was about 200 K.

The planar triode was used to study the effects of the adsorption of various gases on the work function of a tantalum surface[69]. The change in the work function of the surface was determined from the change in the collector current for a given applied emitter voltage in the retarding region of the characteristic plot. The total change in the work function of the tungsten surface as a result of the adsorption of oxygen was +1.7 eV.

In this study of the effect of adsorbed oxygen on the work function of a tantalum surface, was determined by measuring the change in the "effective" work function of the collector surface. By this technique, any changes in the work function of the emitter would not interfere with the measurement of the change in the work function of the collector. Care was taken to ensure that the change in the work function that was measured was due to the adsorption of oxygen and not as a result of the contamination of the collector surface due to desorbed gases from the walls of the reaction cell.

REFERENCES

1. Moore, W. J., "Physical Chemistry", (Prentice-Hall, Englewood, 1964).

2. Hayward, D. O. and Trapnell, B. M. W., "Chemisorption", (Butterworth, London, 1964).

3. Redhead, P. A., Trans. Faraday Soc., 57, 641 (1961).

4. Ehrlich, G., J. Chem. Phys., 34, 810 (1961).

5. Miles, J. L. and Smith, P. H., J. Electrochem. Soc., 110, 1240 (1963).

6. Jennings, T. A., McNeill, W. and Salomon, R. E., J. Electrochem. Soc., 114, 1134 (1967).

7. Zanberg, É. Ya. and Ionov, N. I., Soviet Phys. - USPEHKI (English Transl.), 67, 225 (1959).

8. Zemel, J., J. Chem. Phys., 28, 410 (1958).

9. Page, F. M., Trans. Faraday Soc., 56, 1742 (1960).

10. Bond, G. C., "Catalysis by Metals", (Academic Press, London, 1962).

11. Dushman, S., "Scientific Foundations of Vacuum Techniques", (John Wiley & Sons, New York, 1962).

12. Eyring, H., J. Chem. Phys. 3, 107 (1935).

13. Glasstone, S., Laidler, K. J. and Eyring, H. "The Theory of Rate Processes", (McGraw-Hill, New York, 1941).

14. Ehrlick, G., J. Appl. Phys., 32, 4 (1961).

15. Redhead, P. A., Vacuum, 12, 203 (1962).

16. Vas'ko, N. P., Ptushinskii, Yu. G. and Churkov, B. A., Surf. Sci. 14, 448 (1969).

17. Ehrlick, G., Advan. Catalysis, 14, 255 (1963).

18. Ehrlick, G., J. Chem. Phys., 34, 29 (1961).

19. Hickmott, T. W., J. Chem. Phys., 32, 810 (1960).

20. Forsythe, O. E. and Watson, E. M., J. Opt. Soc. Am. 24, 114 (1934).

21. Redhead, P. A., Hobson, J. P. and Kornelsen, "The Physical Basis at Ultra High Vacuum" (Chapman & Hall, London, 1968).

22. Power, B. D., "High Vacuum Pumping Equipment", (Chapman & Hall, London, 1966).

23. Herring, C. and Nichols, H., Rev. Mod. Phys., 21, 185 (1949).

24. Anderson, P. A., Phys. Rev., 88, 655 (1952).

25. Langmuir, I. and Kingdon, K. H., Phys. Rev., 34, 129 (1929).

26. Bosworth, R. C. and Rideal, E. K., Proc. Roy. Soc., A162, 1 (1937).

27. Gurney, R. W., Phys. Rev., 47, 479 (1935).

28. Slater, J. C., "Introduction to Chemical Physics", (McGraw-Hill, New York, 1939).

29. Riviere, J. C., "Solid State Surface Science" edited by M. Green, (Marcel Dekker, New York, 1969).

30. Fowler, R. H., "Statistical Mechanics", (Cambridge University Press, 1966).

31. Du Bridge, L. A., Phys. Rev., 39, 108 (1932).

32. Gomer, R. and Hulm, J. K., J. Chem. Phys., 27, 1363 (1957).

33. Eisinger, J., J. Chem. Phys., 28, 165 (1958).

34. Eisinger, J., J. Chem. Phys., 29, 1154 (1958).

35. Jaeckel, R. and Wagner, B., Vacuum, 13, 509 (1963).

36. Swanson, L. W. and Crouser, L. C., Phys. Rev., 163, 622 (1962).

37. Ehrlich, G. and Hudda, F. G., J. Chem. Phys., 35, 1421 (1961).

38. Engel, T. and Gomer, R., J. Chem. Phys. 52, 1832 (1970).

39. Becker, J. A. and Brandes, R. G., J. Chem. Phys., 23, 1323 (1955).

40. Müller, E. W., J. Appl. Phys., 26, 732 (1955).

41. Klein, R., J. Chem. Phys. 21, 1177 (1953).

42. Page, L. and Adams, N. I., "Principles of Electricity", (D. Van Nostrand, New York, 1950).

43. Potter, J. G., Phys. Rev., 58, 623 (1940).

44. Hopkins, B. J. and Smith, B. J., J. Appl. Phys. 39, 213 (1968).

45. Shelton, H., Phys. Rev., 107, 1553 (1957).

46. Jowett, C. W. and Hopkins, B. J., Surf. Sci., 22, 392 (1970).

47. Adams, D. L., Germer, L. H. and May, J. W., Surf. Sci., 22, 45 (1970).

48. Smith, J. N., Wallenwinkel, J. and Los, J., Surf. Sci., 22 411 (1970).

49. Abey, A. E., J. Appl. Phys. 40, 284 (1969).

50. Redhead, P. A., Vacuum, 13, 253 (1963).

51. Norris, W. T., J. Appl. Phys. 35, 467 (1964).

52. Aref'ev, A. V., Lisitsyn, and Maksimov, S. P., Instr. and Exper. Techn. (English Transl.) 3, 660 (1968).

53. Lawson, R. W. and Woodward, J. W., Vacuum, 17, 205 (1967).

54. Cope, J. O., Vacuum, 18, 665 (1968).

55. Bannock, R. R., Vacuum, 12, 101 (1962).

56. Barnes, G., Gaines, J. and Kees, E., Vacuum, 12, 141 (1962).

57. Kelk. J. E. and Mellor, D. J., Vacuum, 19, 451 (1969).

58. "The International Dictionary of Physics and Electronics", Mickels, W. C., Editor-in-Chief, (D. Van Nostrand Company, New York, 1961).

59. Wang, G. C. Y. and Lee, C. Y., "Thermophysical Properties of High Temperature Solid Materials", Toulaukian, Y. S., Editor, (Macmillian, New York, 1967).

60. Lange, N. A., "Lange's Handbook of Chemistry", (McGraw-Hill, New York, 1952).

61. Malter, L. and Langmuir, D. B., Phys. Rev., 55, 743 (1939).

62. Goode, G. C., Ph.D. Thesis, University of Aston in Birmingham, (1969).

63. Massey, H. S. W. and Bushop, E. H. S., "Electronic and Ionic Impact Phenomena", (Oxford at the Clarendon Press, 1952).

64. Zandberg, E. Ya. and Tonlegode, A. Ya., Soviet Phys. Tech. Phys. (English Transl.), 10, 1162 (1966).

65. Zingerman, Ya. P., Ishcuk, V. A. and Morozovskii, V. A., Sov. Phys. - Solid State, (English Transl.), 2, 2030 (1960).

66. Hopkins, B. J. and Riviere, Brit. J. Appl. Phys., 15, 941 (1964).

67. Zingerman, Ya. P. and Ishcuk, V. A., Sov. Phys. - Solid State, (English Transl.), 8, 2394 (1963).

68. McCarroll, B., J. Appl. Phys., 40, 1 (1969).

69. Abey, A. E., J. Appl. Phys., 40, 284 (1969).